2022

Towards the Development of High-Fidelity Models for Large Scale Solar Energy Generating Systems

Samadhi Kaushalya Korale Liyanage

UNIVERSITY
OF WOLLONGONG
AUSTRALIA

Towards the Development of High-Fidelity Models for Large Scale Solar Energy Generating Systems

Samadhi Kaushalya Korale Liyanage

This thesis is presented as required for the conferral of the degree:

Doctor of Philosophy

Supervisors:
Professor Sarath Perera, Associate Professor Duane Robinson, Dr. Dharshana Muthumuni, Dr. Jahan Peiris, Professor Mahinda Vilathgamuwa

The University of Wollongong
School of Electrical, Computer and Telecommunications Engineering

August, 2022

This research has been conducted with the support of an Australian Government Research Training Program Scholarship.

Declaration

I, *Samadhi Kaushalya Korale Liyanage*, declare that this thesis is submitted in fulfilment of the requirements for the conferral of the degree *Doctor of Philosophy*, from the University of Wollongong, is wholly my own work unless otherwise referenced or acknowledged. This document has not been submitted for qualifications at any other academic institution.

Samadhi Kaushalya Korale Liyanage

January 12, 2023

Abstract

Small and large scale solar photovoltaic energy generating systems have been observed to take a leading place in power systems around the world which are aiming to move away from the use of fossil fuels. Technical and other challenges associated with such systems have become the focus areas of discussion and investigation in recent years. Among a range of technical challenges, power quality issues associated with the power electronic converters, especially the harmonics, are an important aspect in order to ensure that their stipulated limits are maintained. While harmonics caused by small-scale inverters, for example, those used in rooftop systems, are managed through their harmonic current emission compliance requirements, the harmonics caused by large scale inverters used in solar farms need to be managed at network levels which is essentially the responsibility of the network owners and operators. To be successful in this management process, the relevant generator connection requirements and system standards, relevant data provided by inverter manufacturers, pre-connection and post-connection studies and procedures require attention. With regard to limits associated with harmonic voltage levels at medium, high and extra high voltage (MV, HV and EHV) levels, well-established international standards exist, whereas the pre-connection study procedures which have existed for many years are now being challenged, noting the increase in the number and capacity of inverter based resources (IBRs).

With regard to pre-connection harmonic compliance studies associated with power electronic based grid integrated resources or devices, the most well-known approach is the use of equivalent frequency domain models of the systems on either side of the point of connection or the grid interface. The grid is often represented by an equivalent harmonic impedance together with a corresponding background harmonic voltage. The power electronic based resources or the devices are represented by Thevenin or Norton models at the harmonic frequencies of interest, which are provided by their vendors where the approaches or the conditions under which these models are determined are not comprehensively known. It is however understood that the parameters of such equivalent circuits are mostly determined based on site tests and represent worst case harmonic performance, which do not necessarily correspond to rated power output. There is also the anecdotal understanding that such models are determined based on mathematical or simulation modelling. The most significant concern associated with such frequency domain models

is their suitability for representation of the actual harmonic behaviour at a given point in time, thus posing the question of their fidelity which forms the backbone of the work presented in this thesis.

It is well known that large scale inverters employ relatively low switching frequencies around 3kHz, yet they lead to dominant low order harmonic currents due to a number of reasons and hence as a precursor to the major work undertaken in the thesis, the mechanisms which govern the generation of such low order harmonics are initially examined so that the concerns associated with frequency domain models can be undertaken in an objective manner. In addressing the concerns associated with frequency domain Thevenin/Norton models, the work presented in this thesis covers the results obtained using a complete electromagnetic transient (EMT) model of a single inverter against the results established using the frequency domain model of the same inverter. The same work is extended to a collection of inverters operating in a solar farm environment as well, considering several scenarios. From these studies undertaken, it is evident that the Norton/Thevenin harmonic models can lead to outcomes that demonstrate an acceptable level of agreement with the results of EMT simulations. The broad observation is that fresh approaches may be required in the modelling of such inverters in grid connected environments to improve the accuracy of pre-connection compliance studies, noting that complete EMT modelling of such systems is seen to be prohibitive.

While noting that inverters manufacturers provide Norton/Thevenin model parameters of large inverters that are mostly based on site testing, it is worthwhile to examine whether these can be theoretically determined, provided all system details, including those of the inverter control systems are known. In this regard, mathematical modelling has been undertaken to determine the inverter output impedance, where the determination of the harmonic source current can be carried out using only a single set of current and voltage measurements at the inverter output. Such mathematical derivation of model parameters helps understand the link between the inverter parameters and the inverter functionality with the corresponding Norton/Thevenin model parameters.

Associated with grid connected inverters, harmonics that are produced by them can be influenced by the harmonics that are present in the grid as background voltages. In this regard, cross harmonic generation is a phenomenon that cannot be ignored where a particular harmonic order that is present in the grid can lead to inverter harmonic currents at different orders in addition to the harmonic order of the voltage to which the inverters are subjected to. The thesis covers the results of a preliminary analysis of the cross harmonics generated by inverters using an individual grid-connected inverter model as well as a grid-connected solar farm model. Based on the work undertaken, a suitable inverter harmonic model that may be considered to study cross harmonic generation is presented.

Acknowledgements

First, I would like to express my sincere gratitude to my principal supervisor Professor Sarath Perera of the University of Wollongong (UOW), for all the support, mentorship, patience, and encouragement provided throughout my candidature. His constructive feedback and guidance led me through challenging times. Beyond research matters, he also provided me with valuable lessons for a successful life. I could not have asked for a better supervisor.

Besides my principal supervisor, I would like to convey my heartfelt thanks to Associate Professor Duane Robinson for his enormous support rendered to me from the very beginning in different ways. I am also grateful to Dr. Dharshana Muthumuni, Dr. Jahan Peiris and Professor Mahinda Vilathgamuwa for their constant support throughout my PhD candidacy.

I wish to thank all my friends in Wollongong for their ideas and support during good times as well as at crucial times during these few years.

I want to acknowledge the facilities and financial support provided by the University of Wollongong, Australia; Manitoba Hydro International, Winnipeg and TransGrid, Australia, throughout my candidature.

Last but not least, I would like to thank my beloved mother and especially my husband, Viraj Senevirathne, for their moral and emotional support and unconditional love.

List of Abbreviations

DPWM	Discontinuous Pulse Width Modulation
EHV	Extra High Voltage
EMT	Electromagnetic Transient
HC	Harmonic Compensation
HV	High Voltage
IBR	Inverter Based Resources
IGBT	Insulated Gate Bipolar Transistor
IEC	International Electro-technical Commission
MPPT	Maximum Power Point Tracking
MRC	Multiple Resonant Controller
MV	Medium Voltage
NER	National Electricity Rules
NSP	Network Service Provider
PV	Photovoltaic
PCC	Point of Common Connection
PI	Proportional Integral
PLL	Phase Locked Loop
PR	Proportional Resonant
PSCAD	Power Systems Computer Aided Design
RC	Repetitive controller
SPWM	Sinusoidal Pulse Width Modulation
SRF	Synchronous Reference Frame
SVPWM	Space Vector Pulse Width Modulation Technique
THD	Total Harmonic Distortion
THIPWM	Third Harmonic Injection Pulse Width Modulation
PWM	Pulse Width Modulation
VSC	Voltage Source Converters

Publications Arising from the Thesis

- S. Liyanage, S. Perera, D. Robinson, D. Muthumuni, J. Peiris and M. Vilathgamuwa, "Towards the Development of High Fidelity Harmonic Models for Solar Farms: Existing Knowledge," 2018 Australasian Universities Power Engineering Conference (AUPEC), 2018, pp. 1-6, doi: 10.1109/AUPEC.2018.8758037.

- S. Liyanage, S. Perera and D. Robinson, "Analytical Derivation of Three Phase Inverter Harmonic Model Parameters," 2021 IEEE PES Innovative Smart Grid Technologies - Asia (ISGT Asia), 2021, pp. 1-5, doi: 10.1109/ISGTAsia49270.2021.9715668.

- S. Liyanage, S. Perera and D. Robinson, "A Study on Cross-Harmonic Generation by Large Three-phase Inverters in Solar Farm Environments," 2022 20th International Conference on Harmonics & Quality of Power (ICHQP), 2022, pp. 1-6, doi: 10.1109/ICHQP53011.2022.9808557.

- S. Liyanage, S. Perera and D. Robinson, "Harmonic Emission Assessment of Solar Farms: a Comparative Study Using EMT and Frequency Domain Models.", CIGRE Science & Engineering (CSE) Journal, June, 2022.

Contents

List of Figures

List of Tables

Chapter 1

Introduction

1.1 Statement of the Problem

The unprecedented growth of small and large scale solar photovoltaic (PV) generating systems around the world is intertwined with a myriad of well-known advantages. However, this growth is bundled together with numerous technical challenges. Among these are power quality problems, and in particular, the harmonic issues which arise as a result of power electronic interfaces (inverters) being used. The impact associated with harmonic currents generated by the solar farms (i.e. multiple inverter systems) becomes problematic as many of the large solar power plants that are considered for connection (or already connected) are located in areas where the grid is relatively weak (low fault levels) or otherwise in locations where the system strength is low.

The harmonic currents injected by inverters to the connected power system can be classified into two main groups: low-order harmonics and higher-order harmonics. Generally, in networks that are managed employing IEC (International Electro-technical Commission) standards and guidelines, low-order harmonics usually refer to the harmonics up to 50^{th} order. The main cause of higher-order harmonics is the high-frequency inverter switching, where such harmonics can be effectively mitigated using a low-pass filter connected to the inverter output terminals. However, in practice, pulse width modulated (PWM) inverters also produce low-order harmonics due to a number of reasons. This is particularly the case with large inverters also, where the switching frequency is not as high as in the case of smaller rooftop inverters.

The main reasons for the generation of low-order harmonics by the inverters are the converter topology, converter control methods and the power electronic components. Apart from these, the background harmonics in the connected grid, semiconductor switch dead-times, magnetizing currents of the inverter transformer and the inverter modulation strategies have been identified as some of the other factors that are linked to the generation of low-order harmonics. The low-order harmonics up to 50^{th} are usually required

to be managed to ensure that the networks meet stipulated planning levels adopted by the network owners and operators.

In the IEC guidelines, installations such as solar farms have to meet the emission allocations provided by the network operators. For the purpose of evaluating the harmonic voltages that arise as a result of such connections, harmonic impedance profiles (loci) are evaluated at the point of common connection (PCC), considering various network scenarios of relevance. In this case, the external network data is provided as a collection of impedance polygons capable of representing the network as a point located on the R/X plane. To choose the impedances, a number of points that lie on polygon edges are chosen to represent frequency-dependent impedance scenarios at the PCC. When determining the harmonic voltages at the PCC, it is usually the practice to have the harmonic currents injected from the inverter or group of inverters collectively into the harmonic impedances established by the worst-case Norton/Thevenin frequency domain models. The main reason for using frequency domain Norton/Thevenin models instead of the inverter electromagnetic transient (EMT) models is the excessive computational burden associated with the latter.

Norton harmonic models of inverters are known to be mostly established through measurements carried out at a selected test site by inverter vendors/manufacturers, which can be totally different from the actual solar farm environment to which the inverter is physically connected. These inverter harmonic models are also known to correspond to the worst case harmonic performance of the inverters operating at the unity power factor. It is also known that the harmonic currents generated by inverters are affected by the inverter external conditions. Therefore, the vendor provided inverter models can only be applied under limited conditions. Furthermore, there can be interactions between the inverters in a solar farm and the rest of the inverters connected network (especially the cable network), which are not represented by the vendor-provided inverter harmonic models. Thus, the accuracy achieved by using vendor-provided fixed Norton/Thevenin harmonic models is questionable with regard to harmonic pre-compliance studies.

Considering the broad problematic areas identified, it is worthy of examining the root causes of the generation of low-order harmonics by the inverters in solar farm environments. Furthermore, it is seen to be worthy to investigate how the Norton/Thevenin models, which are commonly used in pre-compliance studies, perform under different inverter internal and external conditions compared with the performance predicted by detailed EMT models. It is also useful to delve into the development of novel inverter harmonic models that are able to represent the true harmonic behaviour of inverters which take into account the impact of the external harmonics.

1.2 Research Objectives and Methodologies

1.2.1 Research Objectives

The research studies presented in this thesis focus on the low-order harmonics associated with large-scale grid-connected solar farm inverter systems and the examination of associated network behaviour. Broadly, the main objectives of the work presented in this thesis are to investigate the root causes of the generation of low-order harmonics by grid-connected inverters, identify the existing modelling techniques of harmonics generated by the inverters, identify the strengths and drawbacks of using the existing inverter harmonic models in harmonic studies and present new concepts relevant to the modelling of the low-order harmonic emission behaviour of inverters.

The major research activities which have been undertaken are as follows:

- Identification of the root causes of low-order harmonics generated by both single-phase and three-phase inverters, as reported in the literature, and investigation through simulations of how the current harmonics produced by single-phase inverters vary with the current controllers used to regulate the inverter output current, with a view to extend the understandings to three-phase inverters.

- Development of a large-scale three-phase inverter EMT model and a solar farm model to closely resemble a real life grid-connected solar farm, as such models are not readily available for use in research studies. Development of a user-defined component in EMT software to generate the switching pulses of the inverters based on the Space Vector Pulse Width Modulation Technique (SVPWM) as a part of the large-scale three-phase inverter design.

- Development of Norton/Thevenin harmonic models for the designed large-scale three-phase inverter model considering the most significant low-order harmonics and carrying out a sensitivity study to determine to what extent the developed inverter harmonic models can replicate the behaviour predicted by the inverter EMT model under different inverter internal and external conditions.

- Determination of the suitability of the use of general summation and arithmetic summation laws in determining the total harmonic currents injected by a solar farm using the developed farm model.

- Development of mathematical expressions for the Thevenin model parameters of three-phase inverters based on the inverter parameters and control techniques. This facilitates determining inverter harmonic model parameters for a range of harmonic orders with a limited amount of simulation work.

- Investigation of the cross-harmonic generation phenomenon under different grid voltage harmonic levels in a solar farm environment to determine the nature of cross harmonics generation. The main objectives of this investigation are to investigate the significance of cross-harmonics generated by the inverters in terms of the magnitude and to develop inverter harmonic models to represent the cross-harmonic generation of the inverters.

1.2.2 Research Methodology

Although it is well known that inverters produce higher-order harmonics as a result of their high-frequency switching, a thorough investigation needs to be undertaken to establish the root causes of the generation of low-order harmonics. The existing literature presents the most significant causes of low-order harmonic generation by inverters, where voltage ripple in the dc-link has been identified as one of the major causes. To examine this, a simulation model of a single-phase PV inverter system is developed, which is controlled in the d-q reference frame. The developed model is also used to demonstrate how different types of current controllers contribute to regulating the harmonics injected by the inverters.

Considering the main research objective, which is to develop harmonic models of large-scale solar inverters, a detailed simulation model of a large-scale solar PV inverter system is designed as such models are not readily available. Utilising this large scale inverter model, a solar farm model is designed incorporating the cable network of the solar farm. The complete design is modelled in PSCAD^{TM} software as it has been identified as one of the most capable EMT simulation platforms to model and investigate power systems in general. Widely used control systems are used to control the PV inverter system.

In pre-compliance harmonic studies, inverters are usually represented by corresponding Norton/Thevenin models where the model parameters are provided by the inverter manufacturers, which represent the worst-case harmonic performance. The exact methods used to determine the inverter Norton/Thevenin model parameters of practical inverter systems are not described in the literature, and often such work is commercial in confidence. However, it is known that test site data are used to determine the worst-case Norton model parameters. Furthermore, test site characteristics are often completely different from the external network that is actually connected to the inverter in a solar farm environment. Hence, the harmonic currents injected by the Norton models can be different from the harmonic currents injected by the actual inverter system (or the inverter EMT model). To identify the strengths and drawbacks of using Norton/Thevenin models in the place of inverter EMT models in harmonic studies, a sensitivity study is carried out under different inverter internal and external conditions, comparing the results. For that, the Norton model parameters for the designed inverter model are determined purely based

on simulations using the harmonic perturbation injection method since the actual method used in commercial practices is not known.

Based on the inverter parameters and control techniques used in designing the inverter system, mathematical expressions for the inverter output impedance can be derived for both positive and negative sequence harmonic orders. Initially, the expressions are derived for the inverter output impedance considering an inverter model which is connected to a pure dc link voltage, neglecting the dc network dynamics. Following this, the study is extended for the designed complete grid-connected three-phase inverter model. Once the inverter output impedance and the harmonic currents injected by the inverter at the PCC are known, the Norton model source current can be easily determined for each harmonic order.

The cross-harmonic generation is often neglected in most harmonic studies in order to make the study simple. However, the cross-harmonic generation phenomenon is inevitable in practical grid-connected solar PV systems caused by the background harmonics present in the grid. The analysis of the problem becomes complex since the generated voltage/current components at the cross-harmonic frequencies can lead to multiple cross-harmonic generation phenomena. Furthermore, the analysis becomes more intricate when the grid comprises harmonic voltages/currents at multiple frequencies. The scope of the work covered in this regard is limited to a grid comprising a single harmonic only.

1.3 Outline of the Thesis

A brief description of the contents of the remaining chapters is given here.

Chapter 2 is a literature review, and it presents a brief overview of voltage source converters, which are commonly used in solar energy generating systems. The chapter describes the basic terminologies of voltage source converters and moreover, it describes the associated switching mechanisms focusing on a widely used pulse width modulation technique. Furthermore, the existing transmission level harmonic management practices in networks, including emission allocation, limits for individual emissions and compliance assessment, are explained based on relevant IEC principles. The root causes of harmonics generated by both single-phase and three-phase inverters are also described. An overview of the harmonic compliance assessments carried out prior to the grid integration of solar farms and other generating systems, the inverter harmonic models which are widely used for harmonic studies and their drawbacks are also presented in this chapter.

In Chapter 3, generalised models of grid-connected single-phase inverter systems based on three different current control techniques in the d-q reference frame are developed. The selection criteria of the critical components in the developed PV system are described and the design details of the control system are also elaborated. The developed inverter models are used to investigate how the current harmonics generated at the inverter output

vary with the type of current controller used in the inverter model. Furthermore, the contribution of the voltage ripple present at the inverter dc link on generating odd order harmonics at the inverter output is also described.

Chapter 4 presents the design details of a large-scale three-phase grid-connected inverter model based on realistic parameter values as much as possible. The details of the development of a user-defined PSCAD^{TM} component for generating switching pulses for the inverter switches based on the SVPWM technique are also given. The design details of a solar farm model comprising five identical inverters and a cable network are also presented.

Chapter 5 covers the details associated with the determination of the Thevenin model parameters of the three-phase large-scale inverter model developed in Chapter 4. A sensitivity analysis is also presented that compares the harmonics predicted using the Norton/Thevenin models and EMT models under different inverter internal and external conditions for a single grid-connected inverter and multiple inverter solar farm environment. Based on the developed solar farm model, the techniques used to determine the aggregated harmonic current at the PCC are also investigated.

The Thevenin/Norton model parameters are usually determined based on simulations and measurements considering a particular test site. Chapter 6 gives the derivation of mathematical expressions for the Thevenin model parameters for a three-phase inverter with a constant dc link and for a complete grid-connected three-phase inverter.

Chapter 7 presents a detailed analysis of the cross-harmonic generation phenomenon in three-phase grid-connected inverters. A harmonic model, which is capable of representing the cross-harmonics generated by the inverters is also presented.

Chapter 8 gives conclusions derived based on the work presented in the thesis, together with recommendations for future work.

Chapter 2

Literature Review

2.1 Introduction

This chapter presents a brief overview of voltage source converters which are a key component in solar PV generating systems, their switching and mechanisms associated with the emission of unwanted current harmonics. Basic principles which define harmonic distortion in power systems are introduced. Further, the relevant guidelines and standards that limit the harmonic levels in power systems and those standards currently available, which limit the harmonic injection by grid connected inverters are introduced. The harmonic compliance assessment process, which is done prior to the grid-integration of a proposed generation, the type of harmonic models that are presently used for harmonic evaluation of power systems and their drawbacks are also discussed, which is closely connected with the main area of research outcomes presented in the thesis.

2.2 Voltage Source Converters

The well-known voltage source converters (VSC), otherwise known as inverters, are key components in solar PV generating systems. The dc-link of a VSC is connected to the dc output of the series and parallel connected solar panel array together with an energy storing and voltage smoothing capacitor, thus allowing the power flow of VSCs fully controllable [1] and the ac output is produced by employing inverter switching, which is commonly known as Pulse Width Modulation (PWM). There are a number of well-known PWM techniques available and some techniques are preferred in PV inverters as a result of their distinct advantages.

2.2.1 Basics of Sinusoidal Pulse Width Modulation Technique

Sinusoidal Pulse Width Modulation (SPWM) is a switching technique that is used to control the switches of an inverter. In SPWM, a control signal which is known as the

sinusoidal modulating signal is compared with a triangular waveform, which is known as the carrier signal to produce the switching signals of the inverter switches. The control signal is of the same frequency as that of the intended output voltage of the inverter and the carrier signal frequency corresponds to the inverter switching frequency, and it is selected depending mainly on the switching capability of the fully controllable semiconductor switches. The amplitude modulation ratio (m_a) and frequency modulation ratio (m_f) of the signals are defined using equations given in (2.1) and (2.2) respectively [2].

$$m_a = \frac{V_{control}}{V_{tri}} \tag{2.1}$$

$$m_f = \frac{f_s}{f_1} \tag{2.2}$$

where, $V_{control}$ and V_{tri} are the control signal and the triangular signal amplitudes respectively. f_s and f_1 are the switching frequency and the modulating frequency respectively.

SPWM Switching Scheme of Three Phase Inverters

Three phase inverters are commonly used in large-scale systems. In such inverters, to achieve a balanced three-phase output voltage, the carrier waveform is compared with three-sinusoidal control waveforms, which are 120° out of phase from each other. The switching pulse generation mechanism in three-phase inverters is illustrated in Figure 2.1 where A, B and C denote the three phases. V_{AN}, V_{BN} and V_{CN} refer to the corresponding line-to-neutral voltages. The line-to-line RMS voltage (V_{LL}) generated by three-phase inverters at the fundamental frequency as a result of SPWM technique is given in (2.3).

$$V_{LL} = 0.612 m_a V_{dc} \tag{2.3}$$

where, V_{dc} is the inverter dc link voltage.

The SPWM is a commonly used PWM technique in PV inverter applications due to its advantages, such as easy implementation and fewer complexities [3]. Furthermore, the SPWM technique has the advantage of having a constant switching frequency and hence, it is possible to calculate the losses of switching devices, so the thermal design for them becomes easier [4].

It is well known that inverter switching leads to unwanted high-frequency harmonic components (in addition to the required output frequency at voltage $V_{control}$), that are very closely related to the switching frequency [2] which are usually filtered out using low pass filters. However, in addition to these high frequencies, practical inverters also generate low frequency harmonics associated with the various non-idealities and connected equipment, which cannot be avoided. Section 2.3 aims to cover the mechanisms associated with the generation of these unwanted low frequency harmonics considering the inverter as a

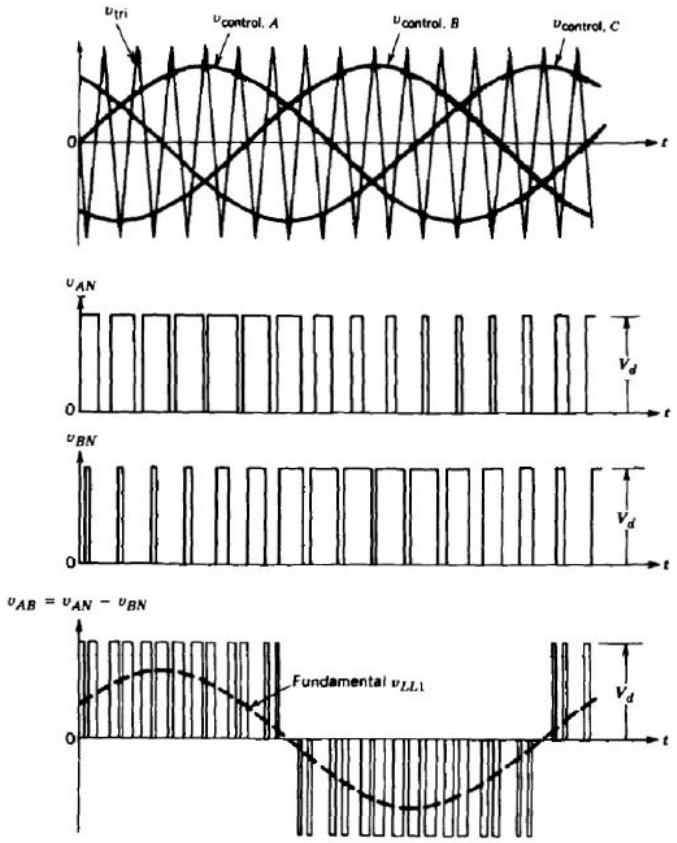

Figure 2.1: Three-phase PWM switching pulses generation [2]

whole, including its non-ideal switches, the dc link, and the transformers that interface the inverters to the ac grid, which itself is not a perfect source.

Other Modulation Techniques Commonly Used in Inverters

Although the SPWM technique is the most well-known method used to generate the switching pulses of the inverters, to achieve better performances of inverters, different modulation techniques have been developed over the years. Among them, Third Harmonic Injection Pulse Width Modulation (THIPWM), Space Vector Pulse Width Modulation (SVPWM) [5], [6] and Discontinuous Pulse Width Modulation (DPWM) [7], [8] techniques are widely used.

The THIPWM method is described in Section 2.3.4, and the SVPWM technique is explicitly described in Chapter 4 and Appendix A. DPWM, the least common of these higher performance methods, is not considered for the remainder of this thesis.

2.3 Mechanisms of Harmonic Generation Associated with Grid Connected Inverters

For the purpose of developing a clear insight into the generation of low frequency harmonics by inverters that are not directly related to the inverter switching frequency, a grid-connected single-phase PWM inverter, which is shown in Figure 2.2 can be considered. Equations can be written for the inverter output ac current and inverter input dc current components [9], [10]. For the ac output current of the inverter,

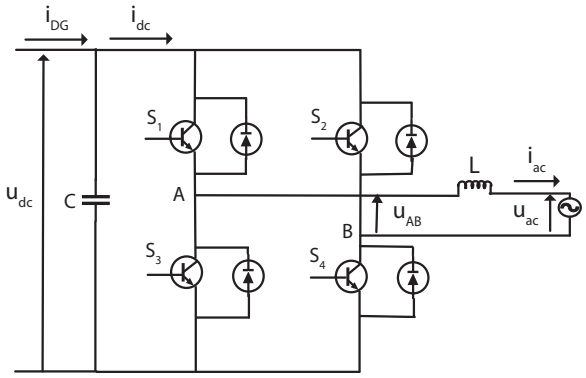

Figure 2.2: Single-phase grid-connected PWM inverter

$$L\frac{di_{\text{ac}}}{dt} = u_{\text{AB}} - u_{\text{ac}} \tag{2.4}$$

where i_{ac} is the inverter injected current to the grid. u_{AB} and u_{ac} are inverter output voltage and grid voltage (assuming it to be a perfect source) respectively. L is the inductance of the low pass filter used. Thus, the equation for the grid injected current can be expressed as,

$$i_{\text{ac}} = \frac{1}{L}\int (u_{\text{AB}} - u_{\text{ac}})dt \tag{2.5}$$

The inverter input dc current can be written as,

$$i_{\text{dc}} = i_{\text{DG}} - C\frac{du_{\text{dc}}}{dt} \tag{2.6}$$

where, i_{dc} and i_{DG} are inverter input current (dc-link current) and the current flow from the dc power generation system respectively. C is the capacitance of the dc-link smoothing capacitor.

From (2.4), it is evident that the inverter output voltage and grid voltage can contribute to the harmonic currents of the inverter output. Hence, the ac output current of the inverter

can be written as,

$$\begin{aligned} i_{\mathrm{ac}} &= i_{\mathrm{ac1}} + i_{\mathrm{g}h} + i_{\mathrm{i}h} \\ &= i_{\mathrm{ac1}} + \sum_{h=2}^{n} i_{\mathrm{g}h} + \sum_{h=2}^{n} i_{\mathrm{i}h} \\ &= i_{\mathrm{ac1}} + \sum_{h=2}^{n} i_{\mathrm{ac}h} \end{aligned} \tag{2.7}$$

where i_{ac1} is the fundamental current component of the inverter output current. $i_{\mathrm{g}h}$ and $i_{\mathrm{i}h}$ are the harmonic current components produced by the grid side voltage harmonics and inverter side voltage harmonic components respectively where the harmonic order is denoted by 'h'. From (2.7) it is evident that the total harmonic current in the ac output current can be eliminated by utilizing an appropriate current controlling technique such that $(\sum_{h=2}^{n} i_{\mathrm{g}h})$ is cancelled by $(\sum_{h=2}^{n} i_{\mathrm{i}h})$.

2.3.1 Current Harmonics ($i_{\mathrm{g}h}$) Generated by Grid Voltage

The current harmonics that arise as a result of the existing grid voltage distortion are unavoidable as practical power systems are inherently polluted, which is caused by other non-linear loads [9], [10].

2.3.2 Current Harmonics ($i_{\mathrm{i}h}$) Generated by Inverter Output Voltage

It is assumed that the single-phase inverter output voltage is generated by a PWM mechanism. However, the high-frequency switching harmonics are ignored and consideration is given only to the low-order harmonics. In general, the PWM modulated output voltage, u_{AB} can be written as,

$$\begin{aligned} u_{\mathrm{AB}} &= d_{\mathrm{pwm}}(t) * u_{\mathrm{dc}} \\ &= (d_{\mathrm{pwm1}}(t) + d_{\mathrm{pwm}h}(t)) * (U_{\mathrm{DC}} + u_{\mathrm{dc}h}) \\ &= u_{\mathrm{AB1}} + \sum_{h=2}^{n} u_{\mathrm{AB}h}, \quad -1 \leq d_{\mathrm{pwm}}(t) \leq 1 \end{aligned} \tag{2.8}$$

where, $d_{\mathrm{pwm}}(t)$ is the PWM signal of which $d_{\mathrm{pwm1}}(t)$ and $d_{\mathrm{pwm}h}(t)$ are the fundamental frequency component and the low-order harmonic components of $d_{\mathrm{pwm}}(t)$ signal respectively. u_{dc} is the dc bus voltage of which U_{DC} and $u_{\mathrm{dc}h}$ denote its fundamental component and the low-order harmonic components respectively. u_{AB1} and $u_{\mathrm{AB}h}$ represent the fundamental component and h^{th} low-order harmonic components of u_{AB} respectively.

In (2.8), if $d_{\mathrm{pwm}}(t)$ and u_{dc} do not contain any harmonic components, u_{AB} will be equal to u_{AB1} and naturally if any low order harmonics are arise in the inverter output voltage, they are caused by the low order harmonics present in either $d_{\mathrm{pwm}h}(t)$ or $u_{\mathrm{dc}h}$ or both.

The Origin of $u_{\mathbf{dc}h}$

The instantaneous power on the dc side of the inverter is given by,

$$\begin{aligned} p_{\mathrm{dc}} &= u_{\mathrm{dc}} i_{\mathrm{dc}} = u_{\mathrm{dc}}(i_{\mathrm{DG}} - C\frac{du_{\mathrm{dc}}}{dt}) \\ &= u_{\mathrm{dc}} i_{\mathrm{DG}} - C(U_{\mathrm{DC}} + u_{\mathrm{dc}h})\frac{d(U_{\mathrm{DC}} + u_{\mathrm{dc}h})}{dt} \\ &= u_{\mathrm{dc}} i_{\mathrm{DG}} - CU_{\mathrm{DC}}\frac{du_{\mathrm{dc}h}}{dt} - Cu_{\mathrm{dc}h}\frac{du_{\mathrm{dc}h}}{dt} \\ &= u_{\mathrm{dc}} i_{\mathrm{DG}} - CU_{\mathrm{DC}}\frac{du_{\mathrm{dc}h}}{dt} - \frac{C}{2}\frac{du_{\mathrm{dc}h}^2}{dt} \end{aligned} \tag{2.9}$$

The instantaneous ac power output of the inverter can be expressed as in (2.10) by substituting for u_{AB} from (2.4).

$$\begin{aligned} p_{\mathrm{ac}} &= i_{\mathrm{ac}} u_{\mathrm{AB}} = i_{\mathrm{ac}} u_{\mathrm{ac}} + Li_{\mathrm{ac}}\frac{di_{\mathrm{ac}}}{dt} = i_{\mathrm{ac}} u_{\mathrm{ac}} + \frac{L}{2}\frac{di_{\mathrm{ac}}^2}{dt} \\ &= (u_{\mathrm{ac1}} + \textstyle\sum_{h=2}^{n} u_{\mathrm{ac}h})(i_{\mathrm{ac1}} + \sum_{h=2}^{n} i_{\mathrm{ac}h}) + \frac{L}{2}\frac{d(i_{\mathrm{ac1}} + \sum_{h=2}^{n} i_{\mathrm{ac}h})^2}{dt} \end{aligned} \tag{2.10}$$

where, u_{ac1} and $u_{\mathrm{ac}h}$ are the fundamental component and the harmonic components of u_{ac}, respectively.

Expressing fundamental components of the grid voltage and inverter output current as, $u_{\mathrm{ac1}} = \sqrt{2}U_{\mathrm{ac1}}\cos(w_0 t + \theta)$ and $i_{\mathrm{ac1}} = \sqrt{2}I_{\mathrm{ac1}}\cos(w_0 t)$, where w_0 is the fundamental angular frequency of the grid voltage, θ is the phase angle of the current i_{ac1} with respect to that of u_{ac1}, and U_{ac1} and I_{ac1} are the corresponding Root Mean Square(RMS) values, (2.10) can be simplified as,

$$\begin{aligned} p_{\mathrm{ac}} &= U_{\mathrm{ac1}} I_{\mathrm{ac1}}\cos\theta + U_{\mathrm{ac1}} I_{\mathrm{ac1}}\cos(2w_0 t + \theta) - w_0 LI_{\mathrm{ac1}}^2\sin(2w_0 t) + i_{\mathrm{ac1}}\textstyle\sum_{h=2}^{n} u_{\mathrm{ac}h} \\ &\quad + u_{\mathrm{ac1}}\textstyle\sum_{h=2}^{n} i_{\mathrm{ac}h} + \frac{L}{2}\frac{d(2i_{\mathrm{ac1}}\sum_{h=2}^{n} i_{\mathrm{ac}h} + (\sum_{h=2}^{n} i_{\mathrm{ac}h})^2)}{dt} \end{aligned} \tag{2.11}$$

If $u_{\mathrm{AB1}} = \sqrt{2}U_{\mathrm{AB1}}\cos(w_0 t + \theta - \theta_1)$, where θ_1 is the phase angle between u_{AB1} and u_{ac1}, p_{ac} can be rewritten as,

$$\begin{aligned} p_{\mathrm{ac}} &= u_{\mathrm{AB}} i_{\mathrm{ac}} \\ &= U_{\mathrm{AB1}} I_{\mathrm{ac1}}\cos(\theta - \theta_1) + U_{\mathrm{AB1}} I_{\mathrm{ac1}}\cos(2w_0 t + \theta - \theta_1) + i_{\mathrm{ac1}}\textstyle\sum_{h=2}^{n} u_{\mathrm{AB}h} \\ &\quad + u_{\mathrm{AB1}}\textstyle\sum_{h=2}^{n} i_{\mathrm{ac}h} \end{aligned} \tag{2.12}$$

Neglecting the losses in the inverter and the dc link capacitor, $p_{\mathrm{dc}} = p_{\mathrm{ac}}$ and hence noting that the power injected by the dc generating system (i.e PV array) is $p_{\mathrm{PV}} = u_{\mathrm{dc}} i_{\mathrm{DG}}$, a power balance equation can be written as, $u_{\mathrm{dc}} i_{\mathrm{DG}} \approx U_{\mathrm{AB1}} I_{\mathrm{ac1}}\cos(\theta - \theta_1)$ (considering

(2.10) and (2.12)). Hence, considering (2.9) and (2.12) it shows that the dc-link capacitor is used for power decoupling, and thus, it may lead to the voltage variations. Similarly, considering (2.9) and (2.11),

$$\begin{aligned} p_{\mathrm{dc}} &= p_{\mathrm{ac}} \\ &= u_{\mathrm{dc}} i_{\mathrm{DG}} - CU_{\mathrm{DC}} \frac{du_{\mathrm{dc}h}}{dt} - \frac{C}{2}\frac{du_{\mathrm{dc}h}^2}{dt} \\ &= U_{\mathrm{ac1}} I_{\mathrm{ac1}} \cos\theta + U_{\mathrm{ac1}} I_{\mathrm{ac1}} \cos(2w_0 t + \theta) - w_0 L I_{\mathrm{ac1}}^2 \sin(2w_0 t) + i_{\mathrm{ac1}} \sum_{h=2}^{n} u_{\mathrm{ac}h} \\ &+ u_{\mathrm{ac1}} \sum_{h=2}^{n} i_{\mathrm{ac}h} + \frac{L}{2} \frac{d(2i_{\mathrm{ac1}} \sum_{h=2}^{n} i_{\mathrm{ac}h} + (\sum_{h=2}^{n} i_{\mathrm{ac}h})^2)}{dt} \end{aligned} \tag{2.13}$$

Assuming i_{DG} to be constant, $u_{\mathrm{dc}} i_{\mathrm{DG}} \approx U_{\mathrm{ac1}} I_{\mathrm{ac1}} \cos\theta$. Therefore, from (2.13), (2.14) can be derived.

$$\begin{aligned} p_{\mathrm{dc}} &= p_{\mathrm{ac}} \\ &= -CU_{\mathrm{DC}} \frac{du_{\mathrm{dc}h}}{dt} - \frac{C}{2}\frac{du_{\mathrm{dc}h}^2}{dt} \\ &= U_{\mathrm{ac1}} I_{\mathrm{ac1}} \cos(2w_0 t + \theta) - w_0 L I_{\mathrm{ac1}}^2 \sin(2w_0 t) + i_{\mathrm{ac1}} \sum_{h=2}^{n} u_{\mathrm{ac}h} + u_{\mathrm{ac1}} \sum_{h=2}^{n} i_{\mathrm{ac}h} \\ &+ \frac{L}{2} \frac{d(2i_{\mathrm{ac1}} \sum_{h=2}^{n} i_{\mathrm{ac}h} + (\sum_{h=2}^{n} i_{\mathrm{ac}h})^2)}{dt} \end{aligned} \tag{2.14}$$

Generally, $|U_{\mathrm{DC}}| \gg |u_{\mathrm{dc}h}|$, $|i_{\mathrm{ac1}}| \gg |i_{\mathrm{ac}h}|$ and $|u_{\mathrm{ac1}}| \gg |u_{\mathrm{ac}h}|$. Therefore,

$$CU_{\mathrm{DC}} \frac{du_{\mathrm{dc}h}}{dt} \gg \frac{C}{2}\frac{du_{\mathrm{dc}h}^2}{dt} \tag{2.15}$$

$$\begin{aligned} U_{\mathrm{ac1}} I_{\mathrm{ac1}} \cos(2w_0 t + \theta) - w_0 L I_{\mathrm{ac1}}^2 \sin(2w_0 t) \gg i_{\mathrm{ac1}} \sum_{h=2}^{n} u_{\mathrm{ac}h} + u_{\mathrm{ac1}} \sum_{h=2}^{n} i_{\mathrm{ac}h} \\ + \frac{L}{2} \frac{d(2i_{\mathrm{ac1}} \sum_{h=2}^{n} i_{\mathrm{ac}h} + (\sum_{h=2}^{n} i_{\mathrm{ac}h})^2)}{dt} \end{aligned} \tag{2.16}$$

Thus, from (2.14), by ignoring the terms that are relatively small in magnitude, an approximate equation for $u_{\mathrm{dc}h}$ can be derived as,

$$\begin{aligned} -CU_{\mathrm{DC}} \frac{du_{\mathrm{dc}h}}{dt} &\approx U_{\mathrm{ac1}} I_{\mathrm{ac1}} \cos(2w_0 t + \theta) - w_0 L I_{\mathrm{ac1}}^2 \sin(2w_0 t) \\ u_{\mathrm{dc}h} &\approx \int \frac{-1}{CU_{\mathrm{DC}}} \left((U_{\mathrm{ac1}} I_{\mathrm{ac1}} \cos(2w_0 t + \theta)) - w_0 L I_{\mathrm{ac1}}^2 \sin(2w_0 t) \right) dt \end{aligned} \tag{2.17}$$

An alternative equation for $u_{\mathrm{dc}h}$ can be derived by equating (2.9) and (2.12),

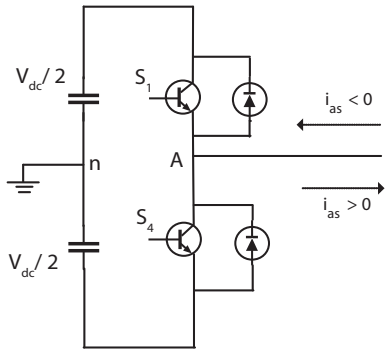

Figure 2.3: Inverter leg [15]

$$
\begin{aligned}
-CU_{\mathrm{DC}}\frac{du_{\mathrm{dc}h}}{dt} &\approx U_{\mathrm{AB1}}I_{\mathrm{ac1}}\cos(2w_0t+\theta-\theta_1)\\
u_{\mathrm{dc}h} &\approx \int \frac{-U_{\mathrm{AB1}}I_{\mathrm{ac1}}\cos(2w_0t+\theta-\theta_1)}{CU_{\mathrm{DC}}}dt
\end{aligned}
\tag{2.18}
$$

Therefore, from (2.17) and (2.18), it is apparent that even order harmonic components are dominant in the dc link voltage and the amplitude of $u_{\mathrm{dc}h}$ is proportional to U_{AB1}. Thus, it can be concluded that the harmonics on the dc bus is generated by the commutation process of the inverter. As the u_{dc} mainly comprises even order harmonics, the $d_{\mathrm{pwm}}u_{\mathrm{dc}}$ will lead to odd order harmonics. The low-order harmonics represented by both $d_{\mathrm{pwm}h}$ and $u_{\mathrm{dc}h}$ are unavoidable in the case of a grid-connected inverter.

A similar procedure to the above can be followed for three-phase grid-connected inverters as well to demonstrate the generation of harmonics in the ac output voltage of order $6n\pm1$ where n is an integer [9].

2.3.3 Inverter Dead-time

The well-known inverter dead-time (also known as blanking time) and non-linear turn on and turn off delays degrade the inverter output current quality leading to the generation of low-order harmonics while causing a reduction in the fundamental output current [11]–[15].

The ideal situation and the dead-time effect can be explained using one leg of an inverter as shown in Figure 2.3. Figure 2.4(a) shows the ideal PWM control pulses supplied to the two switches in the inverter leg of Figure 2.3 and Figure 2.4(c) shows the corresponding output voltage. The PWM control pulses with the dead-time of T_d added to the rising edge are shown in Figure 2.4(b) [15]. During dead-time both switches in the inverter leg cease to conduct. Thus, the output voltage will depend on the inverter output current direction (whether $i_{\mathrm{as}}>0$ or $i_{\mathrm{as}}<0$). Considering the dead-time, and the turn on and off times of the switches, the output voltage obtained for the inverter leg is as shown in Figures 2.4(d) and (e) for the two plausible output current directions demonstrating the gain/loss to the

voltage-time area.

Depending on the current direction, the average voltage gain/loss caused by the dead time and turn on/off times of the switches can be expressed as,

$$\Delta V = \frac{-T_d - t_{\text{on}} + t_{\text{off}}}{2T_s} V_{\text{dc}}, \qquad i_{\text{as}} > 0 \tag{2.19}$$

$$\Delta V = \frac{T_d + t_{\text{on}} - t_{\text{off}}}{2T_s} V_{\text{dc}}, \qquad i_{\text{as}} < 0 \tag{2.20}$$

where, T_s is the sampling period, t_{on}, t_{off} and T_d are turn-on time delay, turn off time delay and the dead-time respectively. V_{dc} is the inverter dc link voltage.

Due to the dead-time effect, the instantaneous average output voltage (V(t)) of a single-phase full-bridge inverter is distorted depending on the inverter current (i_{as}) direction by an amount of ΔV as expressed in (2.19) and (2.20). This is graphically shown in Figure 2.5 [14]. This distortion in V(t) at current zero crossings leads to low-order harmonics (such as the third and fifth of the fundamental frequency) at the inverter output voltage.

For a three-phase inverter, the average distorted output voltages can be expressed based on the current directions of the phases (a,b and c) as,

$$\begin{aligned} V'_a &= \Delta V * V_{\text{dc}} \left\{ \frac{2\text{sign}(i_{\text{as}}) - \text{sign}(i_{\text{bs}}) - \text{sign}(i_{\text{cs}})}{3} \right\} \\ V'_b &= \Delta V * V_{\text{dc}} \left\{ \frac{2\text{sign}(i_{\text{bs}}) - \text{sign}(i_{\text{cs}}) - \text{sign}(i_{\text{as}})}{3} \right\} \\ V'_c &= \Delta V * V_{\text{dc}} \left\{ \frac{2\text{sign}(i_{\text{cs}}) - \text{sign}(i_{\text{as}}) - \text{sign}(i_{\text{bs}})}{3} \right\} \end{aligned} \tag{2.21}$$

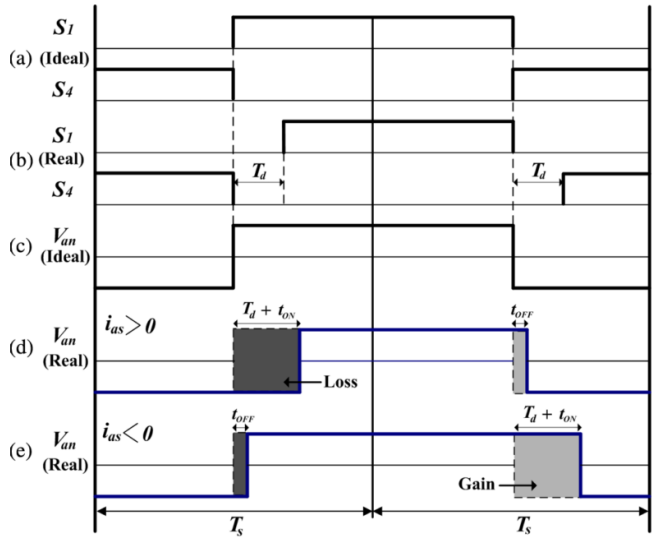

Figure 2.4: PWM signals output voltage patterns [15]

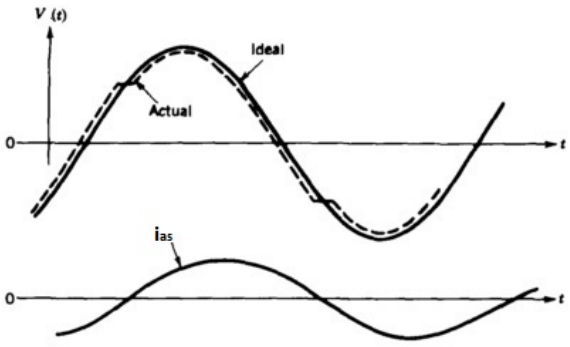

Figure 2.5: Effect of dead-time on the sinusoidal output ([14])

where, sign(i_{as}) = 1 for $i_{as} > 0$ and sign(i_{as}) = 0 for $i_{as} < 0$. V'_a, V'_b and V'_c denote the average three-phase distorted voltage outputs of the inverter respectively.

For three-phase inverters, the harmonic analysis shows the generation of low-order harmonic distortion due to the addition of the dead-time, which occurs at harmonic orders $6m \pm 1$ $(m = 1, 2, 3, ...)$ [12].

2.3.4 Third-order Harmonic Injection

The well-known third harmonic injected PWM is basically a modification over the SPWM [16]. This is done to maximise the utilisation of the dc bus voltage. This method leads to the addition of a third harmonic to the phase voltage waveform. Although this method does not alter the line-to-line voltage magnitude in three-phase inverter outputs, it leads to a reduction in the peak voltage of the phase voltage [16]–[18].

Assume the instantaneous inverter output voltage to be given by y, where y consists of the required fundamental component and the injected third order harmonic component.

$$y = sin\theta + a\ sin3\theta \tag{2.22}$$

where $\theta = wt$ and $'a'$ is the weighting factor of the injected third order harmonic, which is required to be determined.

The maximum and minimum of y can be solved by differentiating (2.22) with respect to θ.

$$\frac{dy}{d\theta} = cos\theta + 3a\ cos3\theta \tag{2.23}$$

By equating (2.23) to zero, values of θ corresponding to the turning points of y can be determined as,

$$\begin{aligned} cos\theta &= 0 \\ cos\theta &= \left(\frac{9a-1}{12a}\right)^{1/2} \end{aligned} \tag{2.24}$$

The corresponding sine values can be found by substituting the $cos\theta$ values in $sin^2\theta = 1 - cos^2\theta$ equation. Thus, the values of y, at the turning points can be derived by substituting the resultant $sin\theta$ values to (2.23).

$$\begin{aligned} \hat{y} &= 1-a \\ \hat{y} &= 8a\left(\frac{1+3a}{12a}\right)^{3/2} \end{aligned} \tag{2.25}$$

The optimum value for a can be determined by differentiating (2.25) and equating the resultant to zero, which gives 1/6 as the result. Therefore, the required waveform is,

$$y = sin\theta + \frac{1}{6}\,sin3\theta \tag{2.26}$$

By substituting for a (which is 1/6) in (2.23), the maximum value of y and the corresponding θ values can be calculated as 0.866 and $\pi/3$, $2\pi/3$, etc. respectively.

It is clear that the addition of the third harmonic component to the modulating waveform causes a reduction in the peak output voltage. Therefore, it is possible to increase the inverter output voltage so that the inverter fully utilizes the dc link voltage magnitude. If the increasing factor is K, (2.26) can be modified as,

$$y = K(sin\theta + \frac{1}{6}\,sin3\theta) \tag{2.27}$$

The peak value of the modulating waveform can be increased up to unity. Since the previous peak value (before adding the K factor) of the modulating signal is known, the value of the K factor can be calculated by,

$$\begin{aligned} 1 &= K * 0.866 \\ K &= 1.155 \end{aligned} \tag{2.28}$$

The addition of the third harmonic voltage results in an increase in the fundamental component of the inverter output voltage by 15.5%. Due to this third harmonic addition, the phase voltage and hence the current will distort with third order harmonic.

The phase voltage of a simple two-level three-phase inverter model can be defined as the voltage at the inverter output (in one phase) with respect to the inverter neutral point. It is important to note that, even though there is the presence of third harmonics in phase-to-neutral voltage, the line-to-line voltage does not contain the third harmonics. The third harmonic current flowing from a three-phase inverter depends on the configuration of the transformer connected to the inverter as well.

2.3.5 Magnetizing Current Drawn by Transformers

While the majority of the rooftop solar PV inverters connected to public low voltage networks are transformer-less, large scale inverters connected to high voltage grids always are interfaced through step up transformers of which their magnetizing currents have been identified as one of the key reasons for low-order harmonic generation [19], [20] where the third order harmonic is the principle harmonic component of which the magnitude is usually about 40% of the excitation current for a typical power transformer [20], [21]. Depending on the transformer connections and the grounding of star points, the third order harmonic current may or may not flow.

2.3.6 DC and Even Order Harmonic Current Generation

Even though not very significant, inverter switching imperfections can lead to half-wave asymmetry in the output voltage, thus leading to a dc component and even order harmonic currents at the output of inverters.

The dc voltage component in the asymmetrical output voltage can lead to asymmetrical biasing of the inverter connected transformers leading to a flow of even harmonics in addition to odd harmonics [22]. The magnitudes of even order harmonics increase with the dc bias in the magnetic core in the transformer, where the phase of even order harmonics indicates the sign of the bias. Techniques exist for compensation of these dc currents by sensing the low-order even harmonics present in the magnetizing current [23].

2.4 Harmonics in Power Systems and Their Management

It is well known that harmonics can adversely affect power systems by degrading the quality of supply. Harmonics can lead to excess heating and losses and interfere with the operation of electrical equipment. Hence, necessary measures have to be enforced to limit the harmonic injected by installations into power systems. For instance, standards such as IEEE 1547-2018 [24] and IEC 61727:2004 [25] applicable for small scale inverters limit the current harmonics injected to low voltage public distribution systems, whereas the injection of harmonic currents at MV, HV and EHV connection points are limited through limits associated with harmonic voltages as covered in guidelines such as the IEC technical report IEC/TR 61000-3-6:2008 [26].

2.4.1 Brief Introduction to IEC/TR 61000.3.6:2008 Technical Report

The main objective of this technical report is to limit the harmonic voltages in MV, HV and EHV power systems to specific levels so that they will not result in any adverse effects on the operation of equipment connected to the network. Customers are responsible

for maintaining the harmonic voltage emission levels at the connection points (point of common connection - PCC) such that the resulting harmonic voltage levels do not exceed the planning levels (refer Table 2.1) adopted by the network utility once all customers are connected. The harmonic voltage limit allocation process methodology prescribed in [26] follows a three stage process.

To ensure electromagnetic compatibility as per the general IEC philosophy following levels need to be paid due attention:

Disturbance Level

The equipment connected to the electricity grid cause disturbances on the network and hence, they may affect the operation of the other equipment connected to the network as expected. The disturbance level generated by a particular piece of equipment connected to a specific location of the network not only depends on the characteristics of the equipment, but also the nature of the point of connection. In general, the network-wide disturbance levels will demonstrate a probabilistic distribution.

Immunity Level

Equipment connected to the electricity network needs to be designed to withstand a certain level of disturbance and the maximum level of disturbance a particular equipment can withstand without affecting its performance is known as the immunity level of that equipment. This mainly depends on the design and component tolerances of the equipment. Considering all equipment in a network-wide sense, these levels also will show a probabilistic distribution.

Compatibility Level

The ideal outcome should be to ensure that the highest disturbance level in a network does not interfere with the operation of the least sensitive equipment. However, from a technical and economic point of view, this is not feasible and hence a compatibility level is chosen equal to a disturbance level which does not exceed, for example, 95% of the disturbance levels in the entire network. This implies that there is a 5% probability of the immunity levels of the connected equipment being affected by the network-wide disturbances.

Planning Level

Noting the description of the compatibility levels, utilities will have to set planning levels (which are internal quality objectives or reference values) for the various voltage levels

Table 2.1: Indicative planning levels for harmonic voltages (in percent of the fundamental voltage)

Odd harmonics non-multiple of 3			Odd harmonics multiple of 3			Even harmonics		
Harm. Order	Harmonic voltage %		Harm. Order	Harmonic voltage %		Harm. Order	Harmonic voltage %	
	MV	HV-EHV		MV	HV-EHV		MV	HV-EHV
5	5	2	3	4	2	2	1.8	1.4
7	4	2	9	1.2	1	4	1	0.8
11	3	1.5	15	0.3	0.3	6	0.5	0.4
13	2.5	1.5	21	0.2	0.2	8	0.5	0.4
$17 \leq h \leq 49$	$1.9\frac{17}{h}$ -0.2	$1.2\frac{17}{h}$	$21 \leq h \leq 45$	0.2	0.2	$10 \geq h \geq 50$	$0.25\frac{10}{h}$ +0.22	$0.19\frac{10}{h}$ +0.16

of the network. These levels are set below the compatibility levels so that electromagnetic compatibility can be achieved where planning levels will allow the establishment of emission limits for the various installations. IEC/TR 61000.3.6:2008 only gives indicative values for the planning levels for the various harmonics, which are summarised in Table 2.1.

The relationship between the compatibility level, disturbance levels, planning levels and immunity levels is illustrated in Figure 2.6.

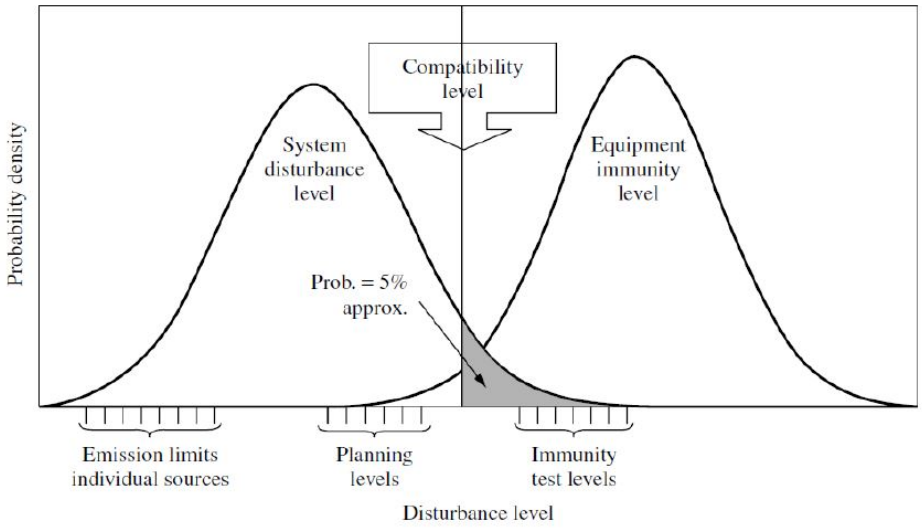

Figure 2.6: Relationship between compatibility, immunity, planning and emission levels [25]

General Summation Law

The IEC/TR 61000.3.6:2008 uses a general summation law which is used to determine the net harmonic voltage (or current) at a particular location due to a number of harmonic producing installations connected to that location. This can be described using (2.29).

$$U_h = \sqrt[\alpha]{\sum_i U_{hi}^{\alpha}} \tag{2.29}$$

where, U_{hi} is the individual harmonic voltage and U_h is the net harmonic voltage. The summation exponent α is selected according to Table 2.2.

Table 2.2: α exponents for different harmonic orders [25]

Harmonic order	α
h < 5	1
$5 \leq \alpha \leq 10$	1.4
$10 < \alpha$	2

2.5 Harmonic Compliance Assessment

In harmonic compliance assessment associated with solar generation farms, harmonic emission levels are to be determined at the PCC. The solar farm developer/operator has to demonstrate through harmonic compliance assessment studies [27] that the harmonics emitted do not exceed the acceptable conditions established by the Network Service Provider (NSPs). Based on the results, harmonic mitigation techniques can be suggested to regulate the harmonics at the PCC if required.

Both time-domain EMT models and frequency-domain models can be considered to investigate the harmonic behaviour of grid-connected solar farms. EMT models are known to provide more accurate results in harmonic studies, provided suitable models are available. Such studies are conducted prior to the connection of a proposed solar plant to investigate whether the harmonic emission levels are compliant as per the emission levels allocated by the Network Service Provider (NSPs), who tend to follow the stipulated guidelines [28]. However, since large-scale solar farms have a large number of inverters, EMT model based method in determining the harmonic emission levels is seen to be prohibitive considering the excessive simulation time. Instead, frequency-domain models are commonly used in harmonic studies in practice.

In harmonic studies, the emission levels are determined for a range of operating scenarios of both the external network and the proposed generator for each harmonic order. Since electricity networks are not static, the external network data is provided as a collection of impedance polygons by the NSPs for each harmonic order. These impedance

polygons represent different network scenarios on the R/X plane. Hence, the external network can be represented by Thevenin equivalent models, which are derived from the data associated with harmonic impedance polygons where the polygon edges are usually considered. As per [27], there are some drawbacks of using this approach. Once a harmonic polygon is traversed, it is not easy that any specific result can be traced back to a specific network configuration.

2.6 Representation of Inverter Harmonic Behaviour Using Norton/Thevenin Model

Historically, harmonics injected by some equipment have been represented by ideal current sources under specified operating conditions. This is still the practice with relatively small equipment such as those connected to public low voltage networks as covered by IEEE 1547-2018 [24] and IEC 61727:2004 [25]. Harmonic behaviour of relatively large power system equipment has been traditionally represented using Norton/Thevenin models [29], [30], where the model parameters determined under specified operating conditions are usually provided by the equipment manufacturers, such as those of grid connected large scale inverters. The grid to which the equipment is connected also has been traditionally represented by Norton/Thevenin model. This harmonic behaviour of the combined system takes the form of the circuit as shown in Figure 2.7 where the superposition theorem is used to determine the net harmonic voltage at the point of common coupling.

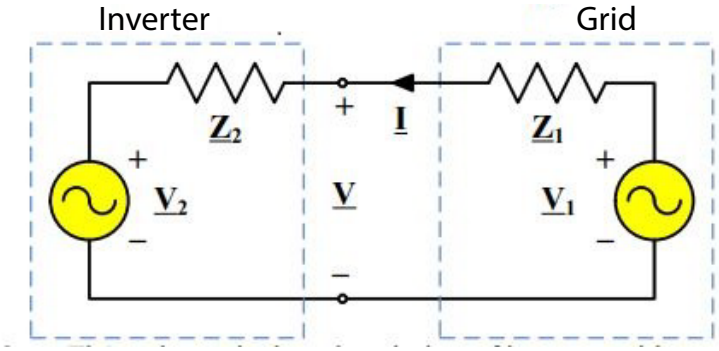

Figure 2.7: Thevenin equivalent of inverter-grid system [31]

The control of the grid-connected voltage source inverters is based on an inner current control loop, which controls the grid current and an outer control loop which controls the dc link voltage. Hence, it is more convenient to present PV inverters as current sources, assuming the voltage at the point of connection is regulated by the distribution transformer [32]. However, the Norton model and the Thevenin model are easily interchangeable as they are equivalent in analytical work.

The inverter manufacturers provide the Norton/Thevenin model parameters alongside the inverters in the frequency domain. These parameters are said to be the worst-case harmonic model parameters for the corresponding frequency. The exact method used by the inverter manufacturers to determine these harmonic model parameters is not known precisely, as the method used is an intellectual property of the manufacturer. However, in the literature, different approaches can be identified which have been used to determine the Norton/Thevenin model parameters of the inverters [31], [32].

2.6.1 Drawbacks of Using Norton/Thevenin Models for Harmonic Studies

It is evident that the inverter manufacturers use experimental approaches when determining the inverter Norton model parameters. However, due to the lack of knowledge on the exact background network information to where the inverter is physically connected, the Norton impedance and source current provided can be inaccurate. Further, the inverter manufacturers provide the worst-case Norton model parameters and hence, the harmonic studies estimate the highest harmonic voltage that the inverter can possibly produce at the PCC [33]. Still, there is a possibility of producing erroneous results for the harmonics emitted by the inverters with this approach, as the interaction between the inverter model with the cable network, transformers and the grid and also, the inverter-to-inverter interactions are not captured when determining the Norton model parameters in a test environment.

In [31], through some experiments carried out under a laboratory environment, the authors show that the inverter Thevenin model parameter values tend to vary even for a specific frequency if the grid voltage contains harmonics, which is the real-life situation, leading to the conclusion that it may be inaccurate to consider an inverter as a Thevenin/Norton model when determining the current harmonic magnitude spectrum at the PCC, when a collection of inverters are operating while connected to the grid.

Based on the above reasons, further investigations are justifiable to determine up to what extent the inverter Thevenin/Norton models can replicate the true behaviour of actual grid connected inverters, paying attention to key reasons which lead to any diversion from the true harmonic behaviour.

2.7 Chapter Summary

This chapter presented a brief overview of voltage source converters and the well-known sinusoidal PWM switching technique, as well as associated performance improvement modulation techniques, such as third harmonic injection PWM technique.

Inverters are commonly known as harmonic sources due to their non-linear behaviour.

Based on previous research work, this chapter covered the most significant root causes for the generation of low order harmonics by grid-connected inverter systems, considering both single-phase and three-phase inverters. This helps not only to understand the complexity of the harmonic generation phenomenon in grid-connected inverter systems, but also to perceive the importance of inverter harmonic modelling.

This chapter also presented a brief introduction to IEC technical report 61000.3.6:2008, which is widely used to manage harmonic voltages in MV, HV and EHV power systems.

The most commonly used frequency domain Norton/Thevenin models of inverters used in harmonic compliance studies was introduced. The fundamentals of the currently used harmonic compliance assessment process were briefly introduced. The drawbacks of using the Norton/Thevenin models in such studies were also described in this chapter which paved the pathway for much of the work presented in this Thesis.

Chapter 3

Harmonics Generated by Single Phase Inverters and their Mitigation Techniques

3.1 Introduction

Current controllers of inverters play a crucial role in regulating the current harmonics, which appear at the inverter output [34]. The most commonly used current controller in the inverters is the Proportional Integral (PI) controller [35], [36]. PI current controllers are known to have good control performance, high reliability and are easy to implement. However, there are some drawbacks of using the PI controllers and hence, Proportional Resonant (PR) controllers have gained popularity as current controllers since they are capable of overcoming the drawbacks of PI controllers [37].

To mitigate the harmonics generated by inverters, it is the common practice to connect harmonic filters, although it is not seen to be the most cost-effective approach. Furthermore, they can make the inverter output harmonic currents even worse due to resonances if multiple inverters are connected in parallel. To control the inverter output current and to mitigate certain harmonic currents simultaneously, advanced current controllers are used nowadays. Multiple Resonant Controller (MRC) is one of them [38]. MRCs are capable of mitigating harmonic currents of specific orders, which is a significant advantage. Repetitive controllers (RCs) are also popular in compensating current harmonics [39]. Theoretically, RCs can suppress all harmonics below the Nyquist frequency (f_s/2; where f_s is the sampling frequency) without any concerns on resonance issues if they are designed properly. However, their increased complexity is a drawback. Furthermore, their response is slow and hence, the stability of the system could become challenging.

In this chapter, low-order harmonic generation mechanisms by single-phase inverters and inverter current controller based harmonic mitigation techniques are investigated. For

that, a complete grid-connected single-phase two-level PV inverter system design is presented, while elaborating on the design methodology, which is simulated using PSCAD^{TM} software in the d-q reference frame.

3.2 Single-phase Inverter Model Development

Comprehensive and open-source single-phase inverter models with the associated control methodology are not readily available for study purposes. To overcome this shortfall, a grid-connected inverter system comprised of a PV array with a Maximum Power Point Tracking (MPPT) system, a dc-dc boost converter, a single-phase inverter, an LCL filter and the grid is considered for simulation. The rated power of the designed single-phase inverter is 5 kW, where the inverter is connected to a 230V/50Hz grid. The significance of this inverter model is that it was designed to control in the d-q reference frame, although it is a single-phase inverter.

3.2.1 PV Array and MPPT Controller

A PV cell can be modelled using a circuit that consists of a current source, an anti-parallel diode, a shunt resistor and a series resistor [40], [41], which is used as the building block of solar arrays. Considering a single PV cell model, the open circuit current and short circuit voltage were calculated employing the equations given in [41]. The number of identical solar cells required to be connected in series and parallel was calculated such that the required power (5 kW) and the required voltage at the solar array output (which is approximately 300V in this model) are attained. With the temperature set at a constant value of 30°C, considering the variable irradiance levels, a set of V-I and P-V curves

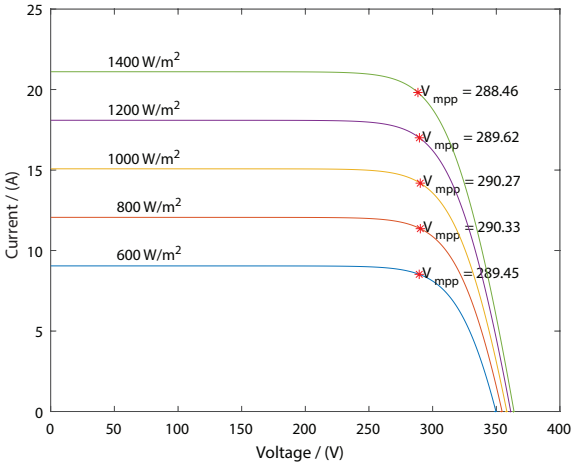

Figure 3.1: V-I characteristic curves for different solar irradiance levels

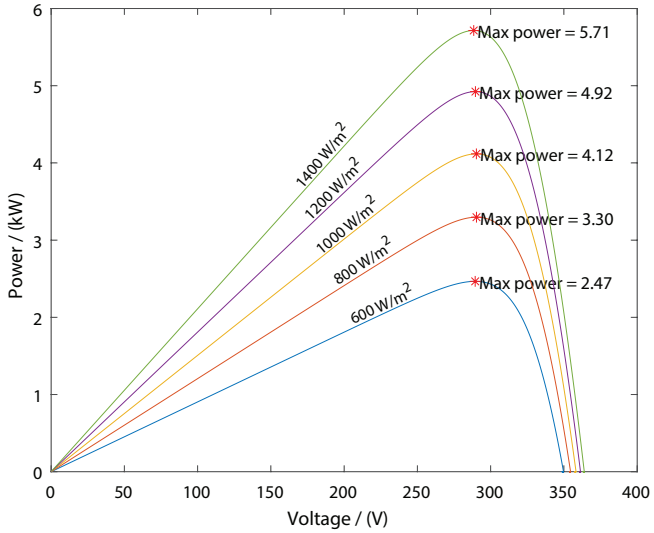

Figure 3.2: V-P characteristic curves for different solar irradiance levels

generated are shown in Figure 3.1 and Figure 3.2 respectively.

In the modelling work undertaken, as per Figure 3.1 and Figure 3.2, the solar irradiance level was selected to be 1200 W/m^2 such that the PV array output voltage is nearly 300V and output power is approximately 5 kW at the maximum power point. To extract the maximum output power from the PV array, an MPPT controller was incorporated into the model to track the maximum power output.

Among the available MPPT algorithms, Perturb and Observe (P&O) method and the Incremental Conductance (InC) method are well known. Although the P&O method is simple to implement, it may fail under fast varying atmospheric conditions. This drawback can be overcome by utilizing the InC method. Hence, the InC method was employed in the simulations, although it is more complicated than the P&O method [42].

3.2.2 DC-DC Boost Converter

The output voltage at the PV array may exhibit variations due to the MPPT system operation. Thus, to achieve a stable dc link voltage at the inverter input, it is common to have a dc-dc boost converter which was designed such that its rated power is 5 kW and the switching frequency is 10 kHz [43]. It was modelled to step-up the incoming nominal voltage of 300 V of the PV array, to a constant voltage, which is 400 V in the simulation model. The PSCAD^{TM} simulated block and the output voltage waveform of the dc-dc boost converter are shown in Figure 3.3 and Figure 3.4 respectively. The switching pulses for the IGBT switch are generated by the MPPT controller.

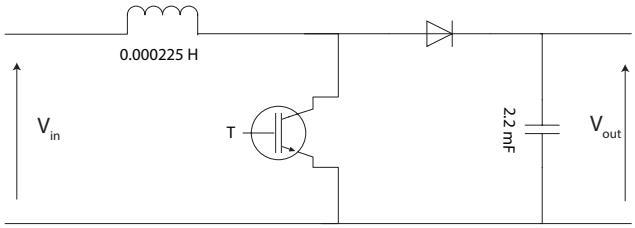

Figure 3.3: dc-dc boost converter

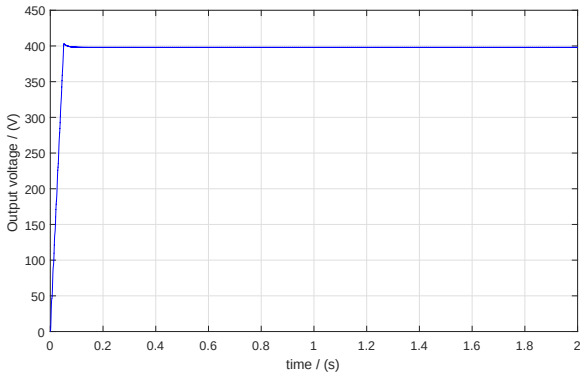

Figure 3.4: dc-dc boost converter output voltage

3.2.3 DC Link Capacitor

The inverter dc link voltage exhibits a ripple component, typically at twice the grid frequency. Hence, a 2200 μF capacitor was selected to limit the voltage ripple present in the dc link to approximately 5% of the intended dc voltage present at the dc link [40].

3.2.4 LCL Filter

In order to reduce the inverter output current harmonics at the inverter switching frequency of 8 kHz (of which the design is covered in Section 3.3), a third-order low-pass LCL filter shown in Figure 3.5 was used where V_i, i_i are the voltage and current at the inverter output, V_c, i_c are the voltage drop and the current flowing through the R_c and C_f. V_g, i_g denote the inverter output voltage, inverter output current, and L_i, R_i, C_f, R_c, L_g and R_g are the inverter side filter inductance, the parasitic resistance of the inverter side inductor, filter capacitance, damping resistance, the grid side filter inductance and the parasitic resistance of the grid side filter inductance respectively.

The transfer function of the filter can be derived as,

$$H = (sR_cC_f + 1)/\{s^3L_gL_iC_f + s^2C_f(L_g(R_c + R_i) + L_i(R_c + R_g)) \\ + s(L_g + L_i + C_f(R_cR_g + R_cR_i + R_gR_i)) + R_g + R_i\} \quad (3.1)$$

The LCL filter was designed following the steps in [44], [45]. This design process essentially consists of two steps where the first step deals with the design of the inverter side inductance (L_i), such that the voltage drop across L_i is below 5-10% of the rated voltage under rated output conditions. Following this, the second step is to design L_g and C_f which represent a second-order low-pass filter. The filter parameters determined are: L_i=0.003 H, L_g=0.0007 H and C_f=16 μF. R_i and R_g set assuming an X/R ratio of the inductors as 10 at the fundamental frequency. Since LCL filters are vulnerable to frequency instability associated with resonance issues, to mitigate the effect of resonance, a damping resistor (R_c) was added to the filter in series with the LCL filter capacitor. The Bode diagram of the designed LCL filter is shown in Figure 3.6.

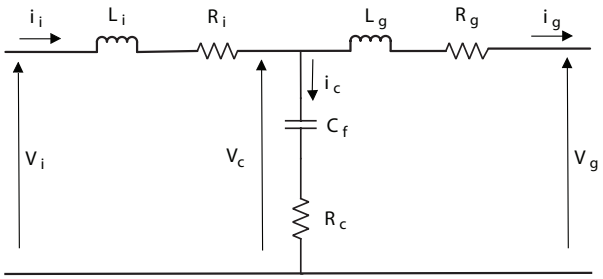

Figure 3.5: LCL filter circuit

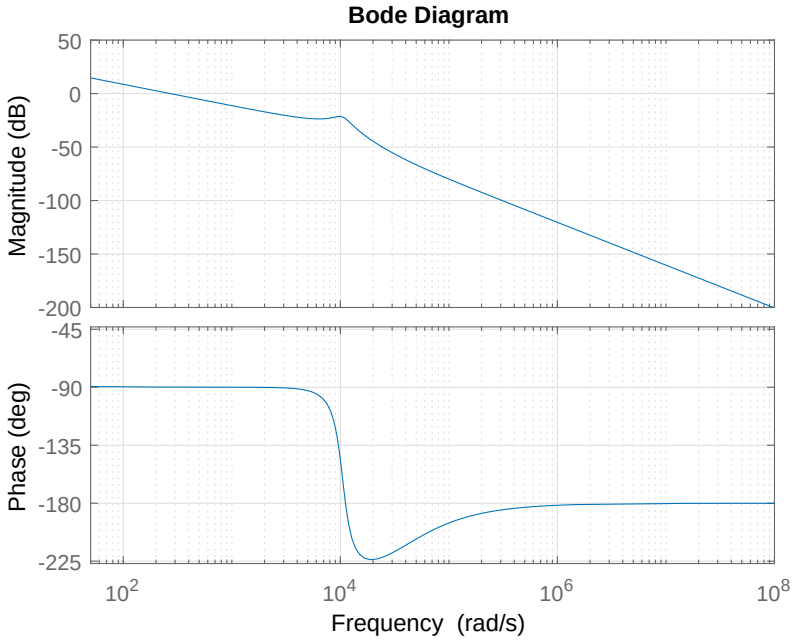

Figure 3.6: Bode diagram of the LCL filter

3.3 Inverter Control Methodology

The full bridge single-phase inverter with IGBTs was assumed to have a switching frequency of 8 kHz.

3.3.1 Controller Design - Proportional Integral Controller

Clark and Park transformations (abc to α-β and abc to d-q transformations respectively) are well-documented in relation to three-phase systems. To achieve this for single-phase systems, first, the current/voltage components should be transformed into stationary reference frame. Although there are various methods to generate the missing orthogonal component, the time delay method was used in this simulation. If there is a signal such as $I = A\ sin(\omega t + \delta)$, it can be phase shifted by 90° to achieve the shifted component. Hence, α-β components of the signal (I) are,

$$\begin{aligned} I_\alpha &= A\ sin(\omega t + \delta) \\ I_\beta &= A\ sin(\omega t + \delta - \pi/2) = -A\ cos(\omega t + \delta) \end{aligned} \tag{3.2}$$

where A, ω and δ are the magnitude, angular frequency and the phase angle of the signal I respectively.

The signals in the α-β reference frame can be transformed to d-q reference frame using (3.3) and the inverse transformation matrix is shown in (3.4).

$$\begin{bmatrix} I_d \\ I_q \end{bmatrix} = \begin{bmatrix} sin(\omega t) & -cos(\omega t) \\ cos(\omega t) & sin(\omega t) \end{bmatrix} \begin{bmatrix} I_\alpha \\ I_\beta \end{bmatrix} \tag{3.3}$$

$$\begin{bmatrix} I_\alpha \\ I_\beta \end{bmatrix} = \begin{bmatrix} sin(\omega t) & cos(\omega t) \\ cos(\omega t) & -sin(\omega t) \end{bmatrix} \begin{bmatrix} I_d \\ I_q \end{bmatrix} \tag{3.4}$$

Aiming to regulate the dc-link voltage and maintain the balance between the ac power supply and the power at the dc-link, a PI controller (transfer function is given in (3.5) based inverter inner loop current controller and an outer loop dc-link voltage controller were designed.

$$H_{PI} = K_P + \frac{K_I}{s} \tag{3.5}$$

where K_P and K_I are proportional and integral constants respectively.

Neglecting the LCL filter capacitor and the damping resistor, the relationship between the inverter output voltage (V_i), inverter output current (i_i) and the grid side voltage (V_g) is as shown in (3.6).

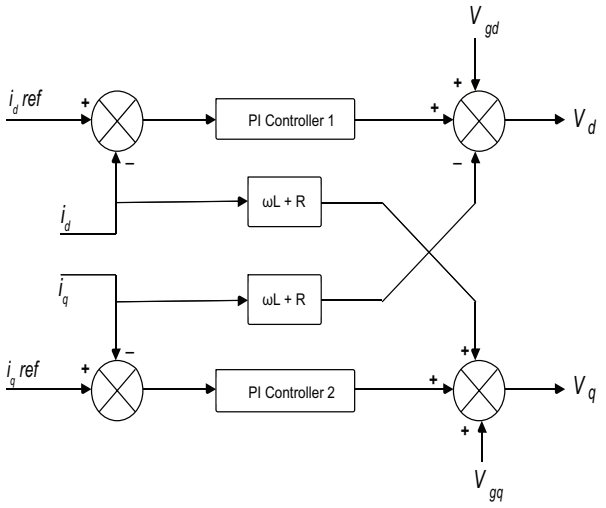

Figure 3.7: Inner current control loop

$$V_i = L\frac{di_i}{dt} + i_i R + V_g \tag{3.6}$$

where, L and R are LCL filter total inductance and total resistance respectively. Equation (3.6) can be converted into synchronous reference frame as shown in (3.7),

$$\begin{aligned} V_d &= L\frac{di_d}{dt} - \omega L i_q + iR + V_{gd} \\ V_q &= L\frac{di_q}{dt} + \omega L i_q + iR + V_{gq} \end{aligned} \tag{3.7}$$

where V_d, V_q are the d-q components of inverter output voltage, i_d, i_q are the inverter output d-q current components and V_{gd}, V_{gq} are the grid side voltage components in d-q reference frame respectively.

The inner current control loop of the inverter was designed based on (3.7). To track the d and q current reference signals, two PI controllers were used in the inner current control loop as shown in Figure 3.7 where $i_d ref$ and $i_q ref$ are the reference current signals in the d-q reference frame. The control system comprises decoupled control of i_d and i_q which leads to speeding up of the system response. Although there are cross-coupling terms, both d-axis and q-axis currents can be independently controlled using PI controller 1 (with K_{p1} and K_{I1} parameter constants) and PI Controller 2 (with K_{p2} and K_{I2} parameter constants) as in Figure 3.7. The inner loop current controller ensures that the ac current components follow the reference values with a fast response. In this simulation, K_p and K_I values for both PI controllers in the inner current control loop were determined by trial and error, leading to $K_{p1} = K_{p2} = 2$ and $K_{I1} = K_{I2} = 100$.

A PI controller is unable to track a sinusoidal reference signal without any steady-state error, which may lead to unacceptable harmonics in the inverter output current. Although this issue can be mitigated by designing the PI controllers in the synchronous reference

frame, this is a complex process, especially for a single-phase inverter and the controller itself may trigger current harmonics at the inverter output.

3.3.2 Controller Design - Proportional Resonant Controller

A single-phase inverter with a PR current controller was designed as an alternative to the PI controller to examine its influence on the harmonic currents of the inverter output. When designing the grid-connected inverter system, the specifications given in the Section 3.2 were used. The transfer function of the ideal PR controller is given in (3.8) where K_P and K_R are gain constants and, ω_0 is the fundamental grid frequency. The primary advantage of using a PR controller as the current controller in a grid-connected inverter system is, the current can be regulated in the natural reference frame. Therefore, it does not require a complex process when using a PR controller as followed in the previous case where PI controllers were used to regulate the inverter output current. In the simulation model developed, the PR controller gains were determined using trial and error, leading to K_P and K_R are 3 and 100 respectively [37], [46], [47].

$$H_{PR} = K_P + K_R \frac{s}{s^2 + \omega_0^2} \tag{3.8}$$

3.3.3 Controller Design - Harmonic Compensation Controller

Harmonic compensation (HC) is commonly used with the PR current controllers to compensate for selective harmonic orders [44], [48], [49]. The transfer functions of an ideal and a non-ideal HC controller designed to compensate for the 3rd, 5th and 7th harmonics (as they are the most prominent harmonics in a single-phase inverter) are given as:

$$H_{Ideal} = \sum_{h=3,5,7} K_{ih} \frac{s}{s^2 + (h\omega_0)^2} \tag{3.9}$$

$$H_{NonIdeal} = \sum_{h=3,5,7} K_{ih} \frac{\omega_c s}{s^2 + 2\omega_c s + (h\omega_0)^2} \tag{3.10}$$

where K_{ih} is the individual resonant gain and ω_c is the cut-off frequency.

For the simulations undertaken, the ideal HC controller was used.

3.3.4 DC Link Voltage Controller

The real power (P) and reactive power (Q) delivered to the ac system by the inverter can be determined in the d-q reference frame as,

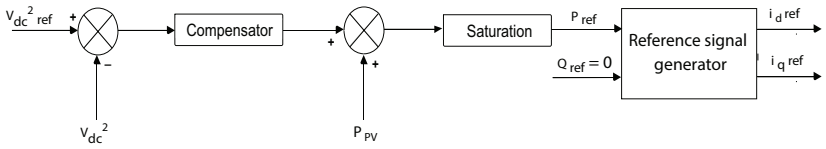

Figure 3.8: Dc link voltage controller block diagram

$$\begin{aligned} P &= \frac{3}{2}(V_{gd}i_d + V_{gq}i_q) \\ Q &= \frac{3}{2}(-V_{gd}i_q + V_{gq}i_d) \end{aligned} \tag{3.11}$$

where V_{gd} and V_{gq} are d-q components of the inverter output (grid side) voltage. i_d and i_q are d-q components of inverter output current. P and Q are the active and reactive power at the inverter output respectively.

Assuming that the inverter is connected to a dc link with a constant voltage, the active and reactive power delivered to the ac system by the inverter can be controlled directly using (3.11). Hence, the reference current components (i_dref and i_qref) required for the inverter current controller can be generated by properly tuning the active and reactive power controllers.

As the inverter is connected to the dc system, comprising the PV array, MPPT controller and the boost converter, the active power delivered by the inverter to the ac network depends on the solar irradiance, the temperature and the control associated with the MPPT system and hence the dc link voltage needs to be regulated at a constant value. Hence a dc link voltage controller was employed in the simulations undertaken to regulate the dc link voltage and to generate the reference signals, i_dref and i_qref for the current controller.

The block diagram of the dc link voltage controller is shown in Figure 3.8 where $V_{dc}ref$ and V_{dc} are the reference dc link voltage and actual dc link voltage respectively, and P_{PV} is the power generated by the PV system. The reference signals for active power (P_{ref}) and reactive power (Q_{ref}) are inputs to the reference signal generator which generates the d-q components of the reference current [1].

3.3.5 Phase Locked Loop

It is well known that voltage source converters (i.e. inverters), that are interfaced with the grid need to be in synchronism with the grid, where this requirement is accommodated by the phase locked loop (PLL). The purpose of using a PLL is to detect the frequency and the phase of the incoming signal and/or to produce an ac signal with the same frequency with the desired phase shift with respect to the incoming signal [50].

A synchronous reference frame phase locked loop (SRF-PLL) was designed as the

interface of the modelled single-phase inverter and the grid of which the block diagram is shown in Figure 3.9. For the operation of the PLL, it is required to generate two orthogonal signals using the grid voltage as done in Section 3.3.1. Using α-β to d-q transformation, the d and q components of the grid voltage can be derived. Assuming the q component of the grid voltage is zero, the grid voltage frequency and phase angle can be tracked by controlling the PI compensator [51].

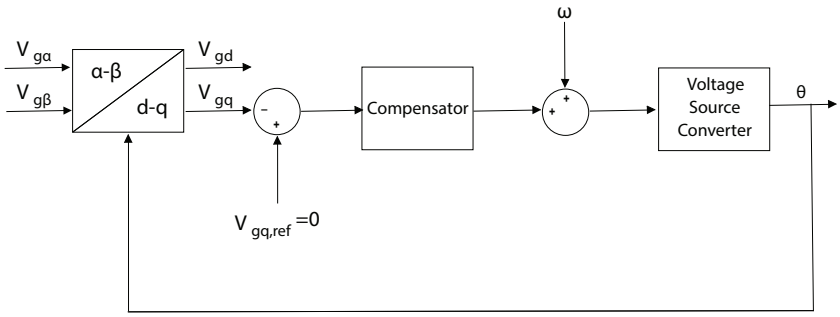

Figure 3.9: PLL block diagram

3.4 Current Harmonics Generated by Single-phase Inverters-Results

The current harmonics generated by single phase inverters may vary with the type of current controllers used in the inverter model. Also, as elaborated in Chapter 2, the voltage ripple present at the inverter dc link can contribute to the generation of the odd order current harmonics at the inverter output.

Initially, the PV inverter was connected to a constant dc link, fixed at 400 V. PI controllers were used to control the grid current such that the inverter output active power is maintained at 5 kW. The corresponding grid current, grid voltage responses and its harmonic spectrum are shown in Figure 3.10. The total harmonic distortion of the current is approximately 1.8%, which can be considered low.

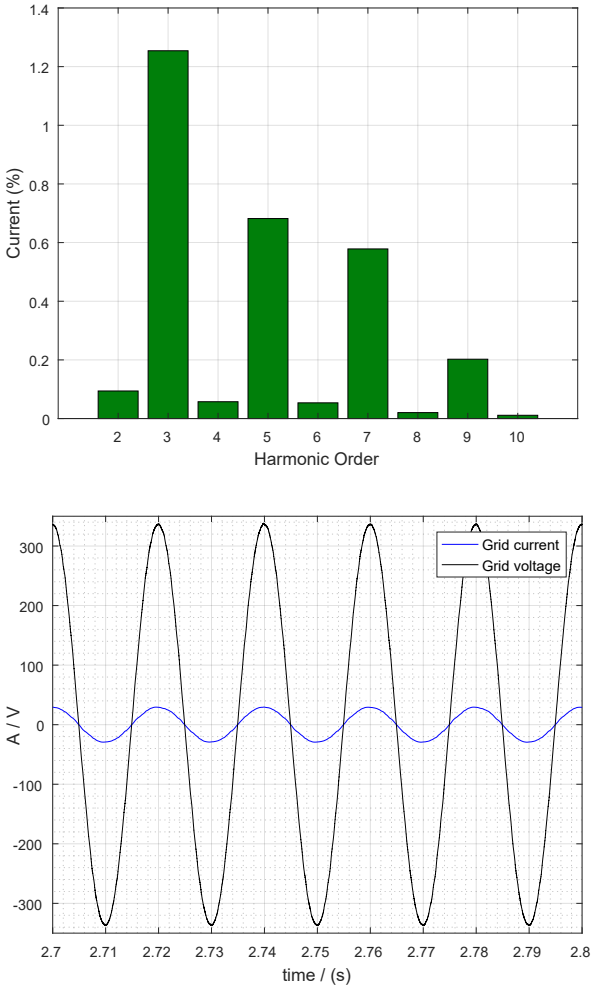

Figure 3.10: Current harmonic spectrum, grid current and grid voltage for the inverter with the PI controller (fixed dc link voltage at 400V)

Following the initial study above, the grid current, inverter output voltage and the current harmonic spectrum of the complete inverter model, controlled with PI current controllers were examined, maintaining the solar irradiance and temperature at 1200 W/m^2 and 30 °C respectively, as shown in Figure 3.11. The waveform of the grid current exhibits a total harmonic distortion of 6.65% which can be considered high.

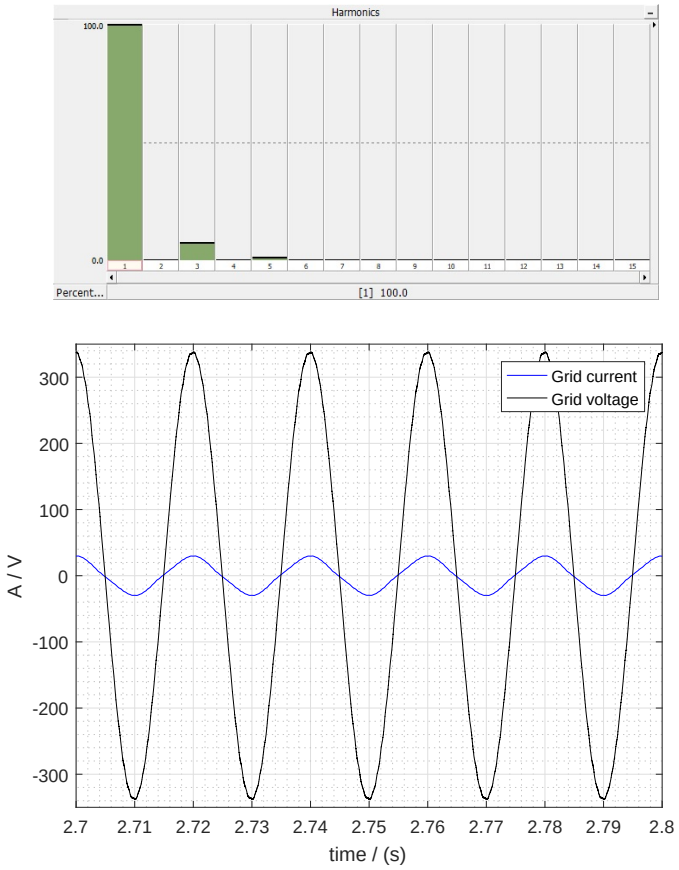

Figure 3.11: Current harmonic spectrum, grid current and grid voltage for the inverter with PI controller

Studies were repeated with the PR current controller, of which the corresponding results are shown in Figure 3.12. It is apparent that the grid current waveform is closer to a sinusoid compared with the case with PI current controllers. The total harmonic distortion of the current is 4.9%, which is less compared with that observed with the complete inverter system with the PI current controller.

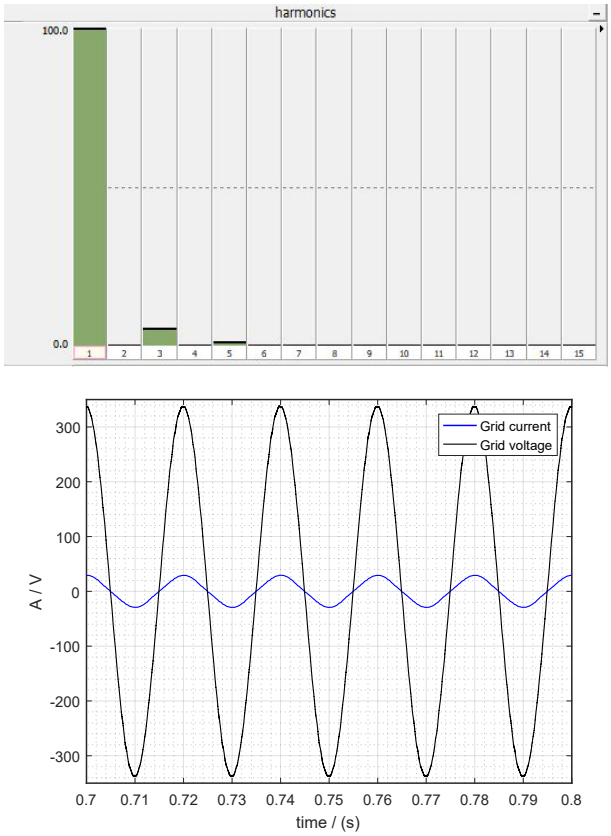

Figure 3.12: Current harmonic spectrum, grid current and grid voltage for the inverter with PR controller

Since the 3rd harmonic current was observed to have the highest harmonic current when the inverter is operating with a PR current controller, an ideal HC was used to reduce the 3rd harmonic current at the inverter output. The resultant grid current waveform and the corresponding harmonic spectrum are shown in Figure 3.13. The total harmonic distortion of the current was observed as 4.3%, which shows some reduction in the current harmonics resulting from the use of the HC controller.

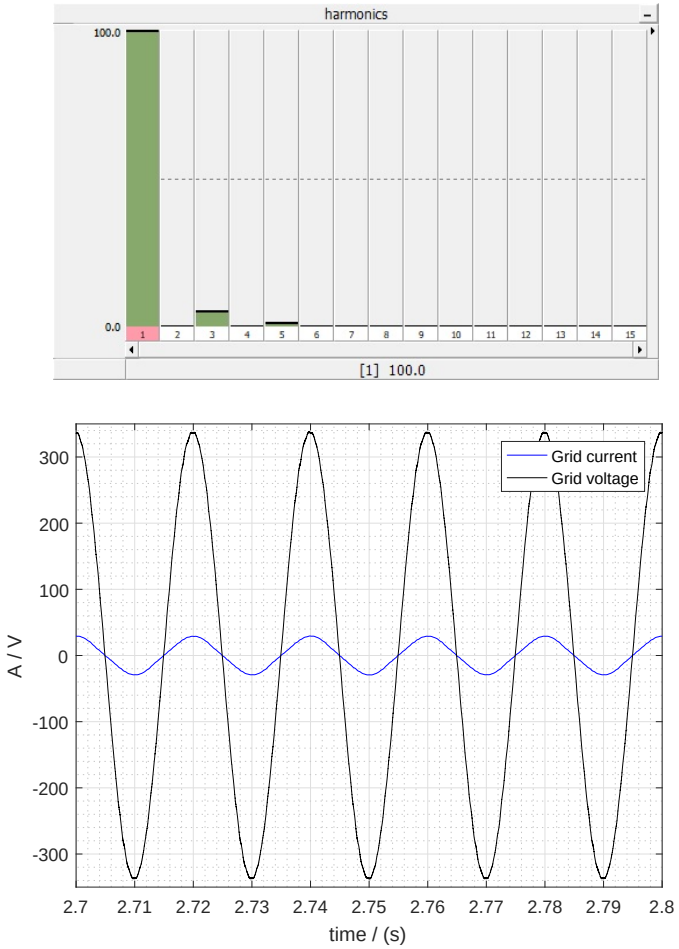

Figure 3.13: Current harmonic spectrum, grid current and grid voltage for the inverter with PR controller and harmonic compensator

Figure 3.14 can be used to compare the inverter output harmonic current variation in the inverters with PI, PR and PR+HC controllers. From the figure, it is evident that odd order harmonics are dominant in the harmonic spectrum and among them, the third order harmonic is the most problematic one. With the use of a PR current controller, the harmonic magnitudes of the odd-order harmonics show some reduction compared to the current harmonics generated by the inverter with PI controllers. Furthermore, after using the HC at the third harmonic, the dominant third order harmonic current show further reduction in magnitude.

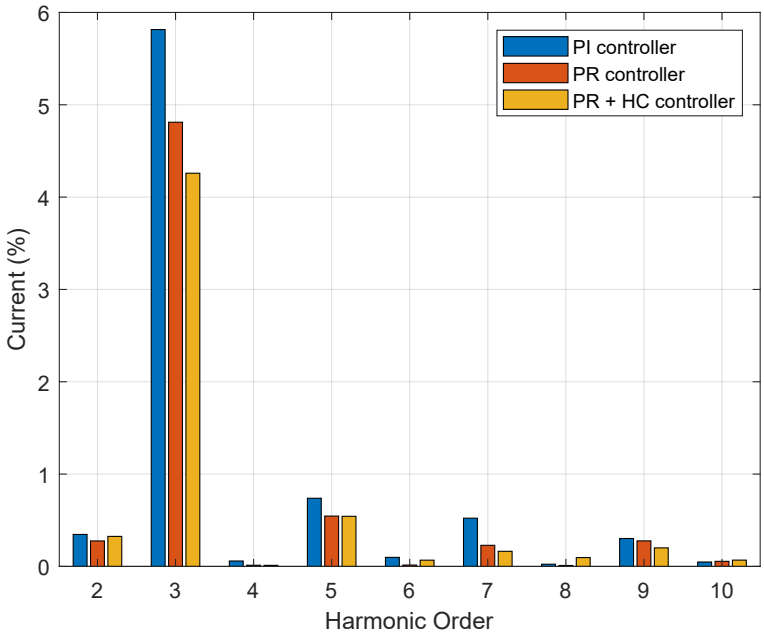

Figure 3.14: Current harmonic spectrum for the inverters with PI, PR and PR+HC controllers

Regardless of the type of controller used, the inverter dc link is seen to have a voltage ripple which varies at 100 Hz (which is twice the grid frequency), as shown in Figure 3.15. The dc link voltage ripple also may have an impact on odd order harmonic current generation at the inverter output. This observation can be consolidated by comparing the harmonic spectrum of the two cases, where, the inverter is connected to a pure dc link voltage (Figure 3.10) with the case where the dc link voltage is not a constant (Figure 3.11). Considerable third order harmonic current increase at the inverter output can be clearly observed in the latter case, even though the current controller and all the other features are the same for these two cases except for the dc system. It is worth noting that the performance and tuning of the current and voltage controllers also may influence the harmonic generation of inverters.

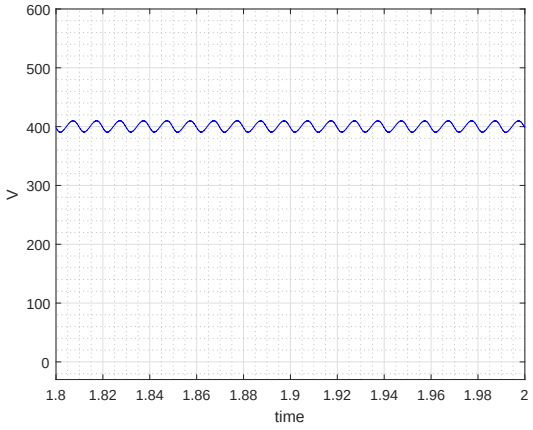

Figure 3.15: Dc link voltage

3.5 Chapter Summary

This chapter mainly focused on examining the generation of, especially, the low order current harmonics by single-phase inverters. For this purpose, a detailed simulation model of a two-level, 5 kW grid-connected single-phase PV system with associated control systems was developed consisting of components such as the PV array, MPPT tracker, dc-dc boost converter, inverter, an LCL filter and the grid. The control architecture of the modelled PV system, including the current controller, a dc-link voltage controller and the SRF-PLL were also described in detail.

Supported by the explanation given in Chapter 2, the grid frequency contributes to the generation of voltage ripple on the inverter dc link, which is at twice the grid frequency. This dc link voltage ripple contributes to the generation of odd order harmonics at the inverter output. This behaviour was investigated based on simulations using two single-phase inverters which have identical parameters, one with a constant dc link voltage and the other with a dc link connected to the rest of the dc network (including the PV array and the dc-dc boost converter). Following this approach, the harmonics generated at the inverter output as a result of the dc link voltage ripple were observed. Moreover, to examine the dependency of the generation of low order current harmonics and their magnitudes on the different controllers, PI, PR and PR + HC current controllers were used since they are the most commonly used current controllers in the literature.

Based on the results established using the simulation model of the PV system, the following conclusions can be derived.

- Low order current harmonics generated by single-phase inverters depend mainly on the inverter operation and grid conditions. The simulation results show that the grid-connected PV system with the inverter connected to a pure dc link voltage has a lower current THD compared to the PV system with the inverter connected to the more detailed dc network model. The current harmonic spectrum at the inverter output also showed that the latter system generates more odd-order harmonics compared to the PV system with pure dc link voltage. Through these observations, it is shown that the inverter dc link voltage ripple contributes in generating odd order harmonics at the inverter output.

- Current controllers play a significant role in regulating the low-order harmonic currents at the inverter output. Based on the current controllers used, the harmonic currents generated at the inverter output may be subjected to vary. Simulations have been performed based on PI, PR and PR + HC current controllers to check how the current harmonics at the inverter output vary depending on the current controller used. From the simulation results, it was proven that the PR + HC controller has better performances compared to the other two controllers considered in regulating

harmonic currents at the inverter output. The PV system with PI current controllers generates the highest odd-order harmonic currents at the inverter output out of the three PV systems.

Chapter 4

Development of an EMT Solar Farm Model

4.1 Introduction

The step by step process of the development of the grid-connected 12.5 MW solar farm model using PSCAD^{TM} software is described in this chapter, where the installation consists of PV panels, five identical 2.5 MW three-phase inverters, each with a dc-link voltage of 1 kV and switching at 3 kHz, their low-pass filters and the step up transformers, MPPT tracking systems, the cable network within the farm, a grid interfacing transformer and the 132 kV, 50 Hz high voltage grid. The parameters of the developed solar farm (including the inverter and the cable parameters) were chosen to replicate a practical grid-connected solar system as nearly as possible.

As stated in Chapter 2, although there are a number of pulse width modulation techniques that can be applied for switching of the inverter, Space Vector Pulse Width Modulation (SVPWM) was adopted in the model developed as it offers a number of advantages, including the optimum utilisation of the dc-link voltage. A user-defined component developed in PSCAD^{TM} to generate the three-phase modulation signals based on the SVPWM technique is also described in this chapter.

4.2 Development of the Grid Connected Three-phase Inverter

One of the most significant challenges in developing an inverter model that is representative of a practical inverter is the unavailability of vital details of such inverters used in practice, including the details associated with the control systems, power electronic inverter switching strategies and many other components. Despite this difficulty, the time domain model developed using PSCAD^{TM} presented in this section employs generic, but

industry recognised control techniques, well-known switching strategies (i.e. SVPWM) and component details, which are as realistic as possible to represent a practical inverter.

4.2.1 PV Array

Taking 1000 Wm^{-2} and 25°C as the reference irradiance and temperature values, 900 Wm^{-2} and 25°C were considered as the actual irradiance and the temperature of the PV array, which was designed to have an output power level, which is slightly higher than the rated value (2.5 MW) noting the power losses in the inverter and the inverter low pass filter. Considering the losses, the number of PV modules connected in series and parallel was determined such that the maximum power delivered by the PV array is around 2.65 MW. The short circuit current and the open circuit voltage per cell were calculated as 2.25 A and 0.83 V respectively. The number of PV modules connected in series to form a string was determined such that the output terminal voltage corresponding to the maximum power point of the PV array (at 900 Wm^{-2} irradiance and 25°C temperature) is nearly 1 kV which is the desired dc link voltage. Considering the PV strings connected in parallel, the current versus voltage and the power versus voltage graphs were developed, from which 1280 was selected as the number of parallel connected strings to produce 2.65 MW of power at the maximum power point of the PV array. The voltage at the PV array output at the maximum power point was noted to be 0.977 kV, which is close to the expected rated dc link voltage of 1 kV.

4.2.2 Three-phase IGBT Inverter, DC-DC Boost Converter and MPPT System

To make the six switch IGBT three-phase inverter switched at 3 kHz representation as close as possible to a practical inverter, an on resistance of 0.0005 Ω was incorporated with the IGBTs and the free wheeling diodes and furthermore, 0.004 kV and 0.001 kV were applied as their forward voltage drops.

The MPPT system and the dc-dc boost converter were developed following the principles described in Sections 3.2.1 and 3.2.2 respectively. The boost converter capacitor and inductor were selected as 2400 μF and 8.468 μH respectively.

4.2.3 Low-pass Filter

LC filters are commonly used in PV inverters to attenuate the high frequency components in the inverter output current [52]–[55]. The filter inductor (L) value of 11.68 μH was determined such that the voltage drop across the inductor is within 5% of the rated inverter output voltage. The filter (C) capacitance of 14458 μF was determined assuming a cut-off

frequency of 400 Hz. The inherent resistance of the inductor was calculated assuming an X/R ratio of 10 calculated at the fundamental frequency.

4.2.4 Inverter Step-up, Grid Interfacing Transformers and the Grid

A large-scale solar farm consists of several PV inverters. Each inverter output voltage is stepped-up using an inverter transformer and connected to the grid interfacing transformer, which again steps up the incoming voltage to the grid voltage. A 2.5 MVA transformer was used as the inverter transformer (delta-wye) to step-up the inverter output voltage from 0.4 kV (line to line rms) to 11 kV (line to line rms). The impedance of the inverter transformer is 0.04 pu. The grid interfacing transformer (wye-delta) was modelled to have a capacity of 100 MVA with a voltage ratio of 11/132 kV and its impedance was specified as 0.1 pu. Most large-scale solar farms are connected to weak grids as they are located in remote areas. However, in the simulation model, the grid impedance was calculated assuming the PV inverter is connected to a relatively strong 132 kV grid with a fault level of 2133 MVA with an X/R ratio of 5 (calculated based on the fundamental frequency), leading to a resistance of 1.6 Ω and inductance 0.0255 H.

4.3 Controllers

A classical PI-based current controller and an inverter dc link voltage controller were developed in the synchronous reference frame [56]–[58]. The inner loop current controller ensures that the current components follow the reference values with a faster response compared to the outer dc link voltage control loop. The controllers were designed adhering to the principles described in Section 3.3.1 and Section 3.3.4 in Chapter 3.

4.4 Inverter Pulse Width Modulation

SVPWM method was used in the simulation work undertaken (although it is relatively more complex to implement compared to sinusoidal pulse width modulation) to generate the inverter switching pulses considering its associated advantages. SVPWM technique effectively reduces the THD of the inverter output voltage and current while allowing optimum utilisation of the dc link voltage [59], [60].

Although an SVPWM library component is available within PSCAD^{TM}, a user defined component was developed as such a custom developed component adds flexibility compared to using the library component. The key steps used in the development are given in Appendix A, the details of which are well covered [61]–[63]. Appendix A explains two methods of developing the user defined SVPWM component and between them, method 1 was used as it is less complicated compared to the other method described. Figure

4.1 shows the flow chart which explains the basic steps followed when developing the SVPWM user-defined component to generate the duty cycles.

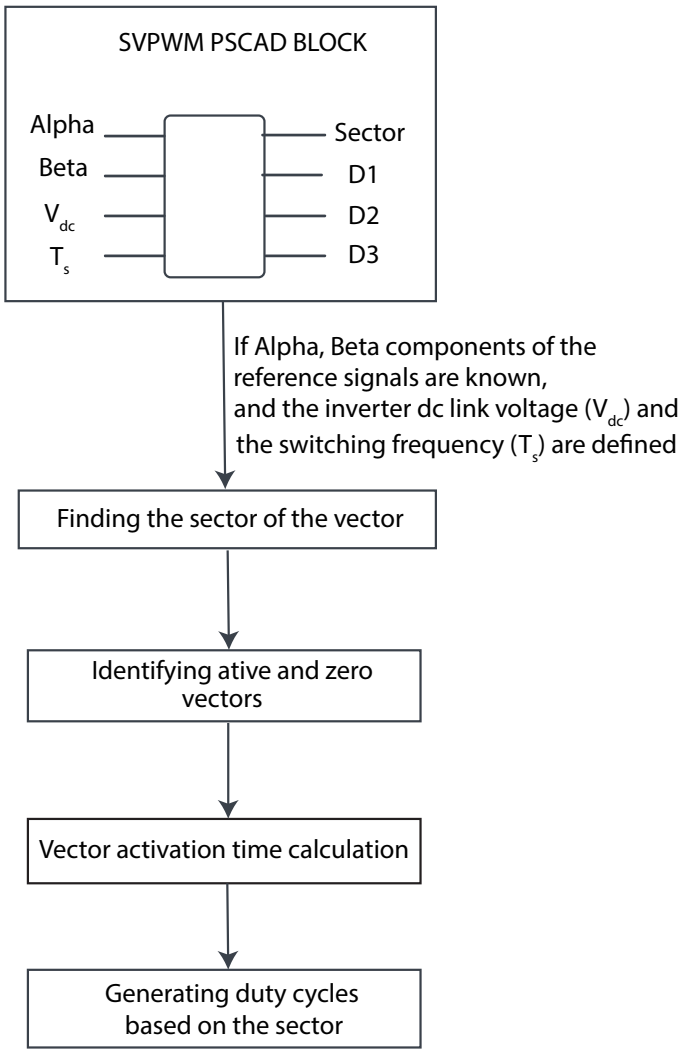

Figure 4.1: Flow chart which shows the generation of the duty cycles based on the SVPWM method

4.5 SVPWM Controlled Grid Connected Inverter Output Performance

As described in Appendix A and also according to the flow chart presented in Figure 4.1, the three-phase reference waveforms generated by the current controller were converted into α-β reference frame using Clark transformation to determine the magnitude and the phase angle of the reference vector. The determined reference vector phase angle is used to identify the exact sector where the reference signal is located. According to the simulation model, the waveforms of the reference phase angle signal and the variation of the sector location of the reference signal are shown in Figure 4.2 and Figure 4.3

respectively.

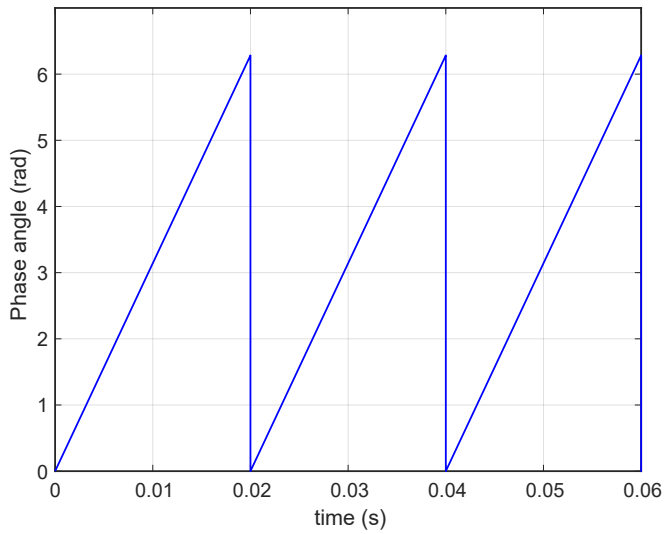

Figure 4.2: Phase angle of the reference signal

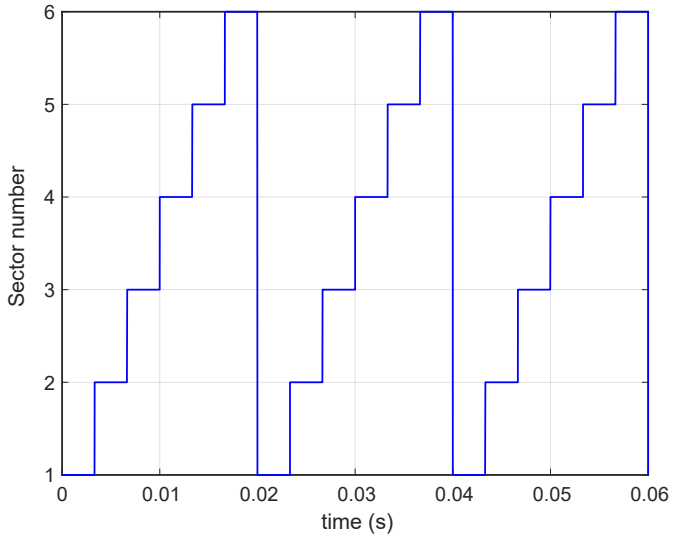

Figure 4.3: Sector location of the reference signal

For each sector where the reference signal is located, corresponding active and zero vectors were identified and the activation times for each active and zero vector were calculated, which are used to generate the duty cycles depending on the reference signal location. The SVPWM modulation signals generated by the developed PSCAD user defined component (of which the details are covered in Appendix A) are shown in Figure 4.4, which can be used to compare with a carrier waveform to generate the switching pulses of the three-phase inverter switches.

Adhering to the procedure described in Section 4.2 - Section 4.4, the complete grid connected time-domain three phase inverter system is developed in the PSCAD^{TM} and

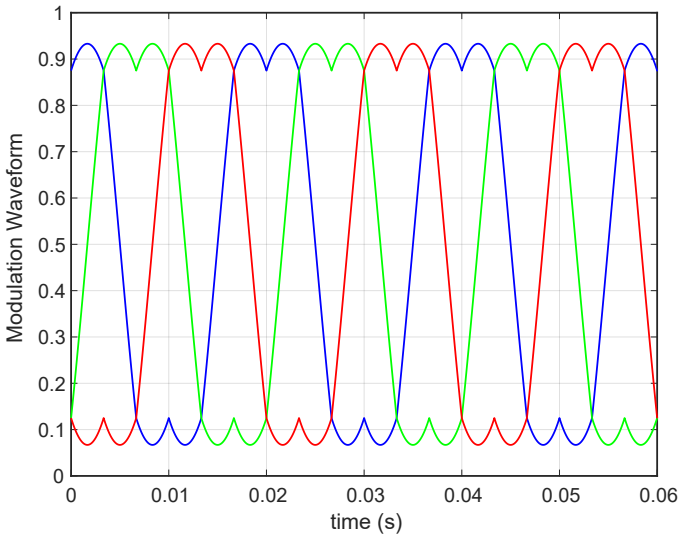

Figure 4.4: SVPWM modulation signal

the schematic diagram of the simulation model is shown in Figure 4.5.

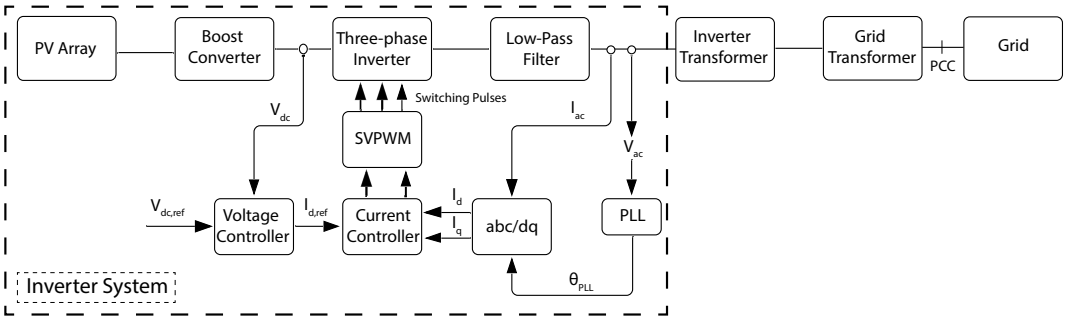

Figure 4.5: Block diagram of the three-phase inverter connected to the grid

With the inverter operating at the rated power level, the current and line to line voltage waveforms observed at the inverter output terminals are shown in Figure 4.6. And the three-phase current and voltage waveforms observed at the PCC are shown in Figure 4.7. As seen from the figures, the voltage and current waveforms are less-distorted. To determine the exact harmonic content of the inverter output current, frequency scanners were used.

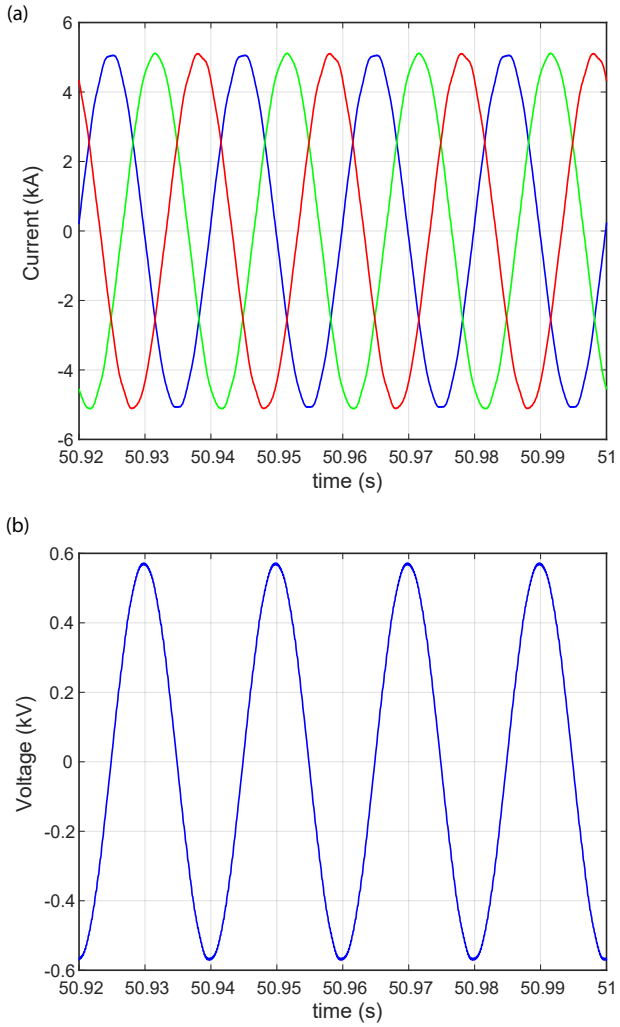

Figure 4.6: (a) Current and (b) voltage waveforms observed at the inverter terminals

The harmonic spectrum of the inverter output current considering an individual phase expressed as a percentage of the rated current is shown in Figure 4.8, which corresponds to a total harmonic distortion of 0.786%. The developed grid-connected inverter system is a balanced one and hence, the other two phases have the same variation as the harmonic spectrum shown in Figure 4.8. It is evident from Figure 4.8 that the 5^{th}, 7^{th}, 11^{th} and 13^{th} are the most significant harmonic components which can be observed in the inverter output current, which is in agreement with the information given in Section 2.3.

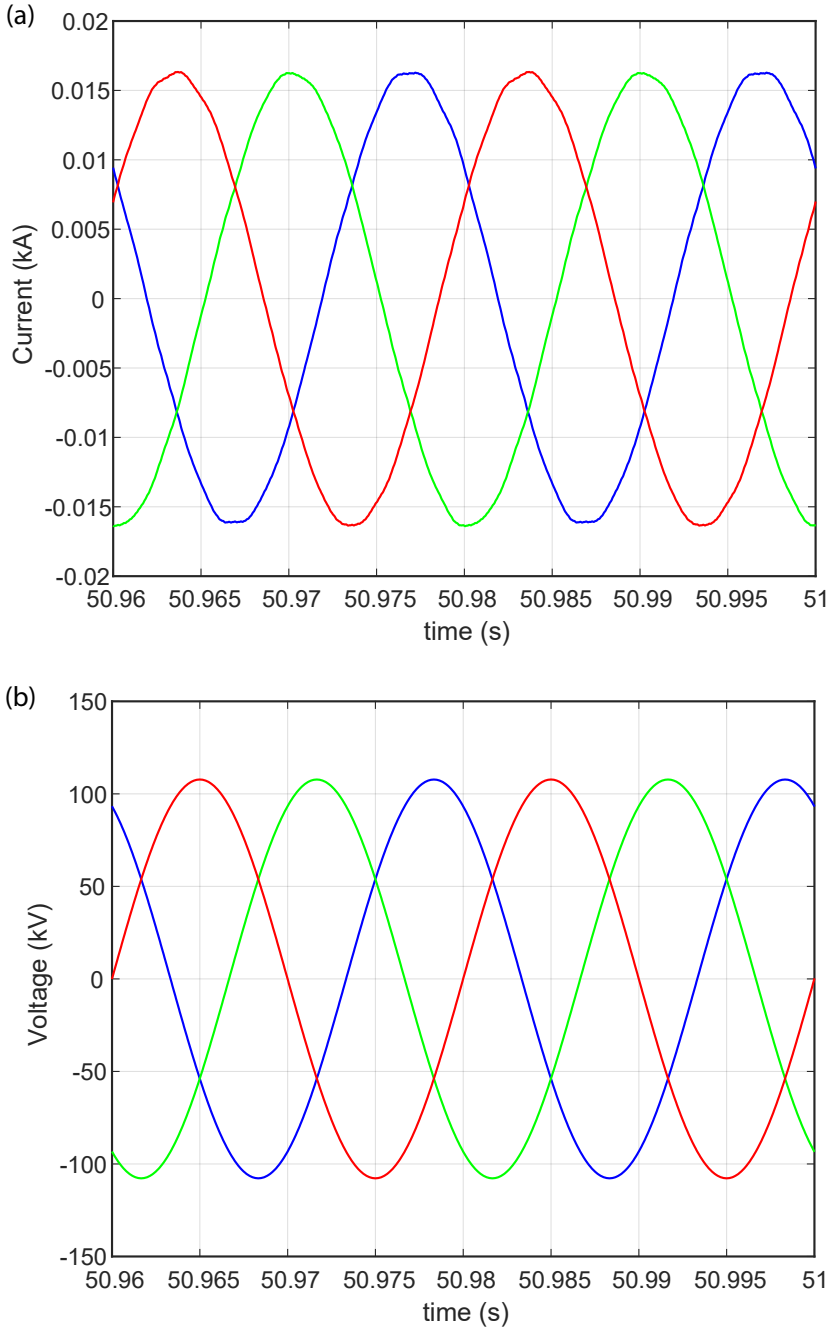

Figure 4.7: (a) Current and (b) voltage waveforms observed at the PCC

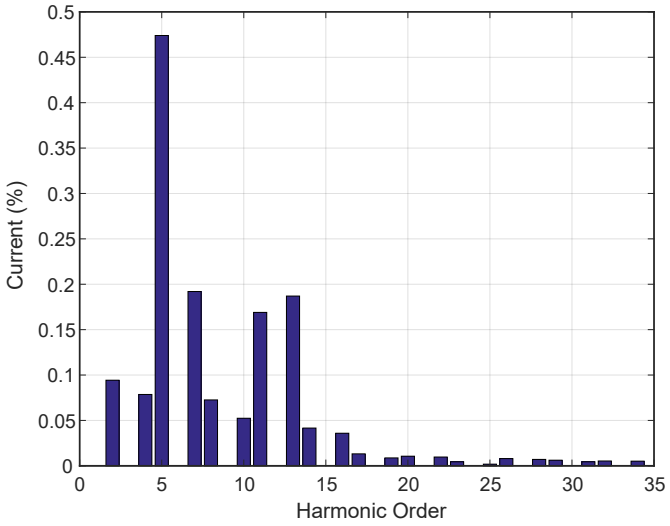

Figure 4.8: Harmonics of the inverter output current at the PCC at the rated power

4.6 Solar Farm Model

To carry out the detailed studies associated with inverter behaviour in a solar farm environment, a 12.5 MW system with five identical 2.5 MW inverters was developed, where the selection of five inverters was a choice to maintain simplicity, although such a small number of inverters will not be sufficient to represent many solar farms. However, this small-scale farm was considered to be adequate to investigate the operational behaviour from a harmonic perspective.

4.6.1 Cable Network

A suitable underground cable network was included within the solar farm model, which is an important part of any solar farm. Such cable networks are neglected in simplistic studies, but it is anticipated that these cable networks may influence the harmonic behaviour as the network harmonic impedance is highly dependent on the cable network in addition to those of the transformers and the grid itself. Cables are more likely to cause resonance at lower frequencies [64]–[68]. Thus, accurate cable modelling is essential in harmonic studies associated with solar farms.

Based on a real solar farm, realistic cable lengths, types and parameters were incorporated in developing the cable network model. Library components of cables are available in PSCAD^{TM}, but they can only be used with very small recommended time steps, whereas this issue can be overcome by using Π sections to represent relatively short cable lengths considering the frequency range of interest in harmonic studies undertaken. The number of Π sections that need to be utilized (or the maximum frequency range represented by a Π line model) can be calculated using (4.1).

$$F_{max} = \frac{Nv}{8l} \tag{4.1}$$

where, F_{max}, N, v and l are the maximum frequency range, number of Π sections, propagation speed in km/s and line length in km respectively. Using (4.1) it was confirmed that to represent the various cable lengths in the solar farm model, a single Π section is adequate.

The complete solar farm layout is shown in Figure 4.9 where each inverter is connected to an inverter transformer which steps up the inverter output voltage of 0.4 kV to 11 kV and the power output by each PV inverter is connected to the underground cables with different cable lengths (representing their geographic locations within the farm) to the 11 kV busbar. The 11 kV busbar is connected to the 11/132 kV grid transformer via 2 km long cable. All parameters of the cables were obtained from a cable catalogue [69]. A summary of the cable information used in the solar farm model is given in Table 4.1.

The current and voltage waveforms of the solar farm measured at the PCC are shown in Figure 4.10. It is evident from the magnitude of the current waveform, that it shows the aggregated current injected by the five parallel connected inverters at the PCC.

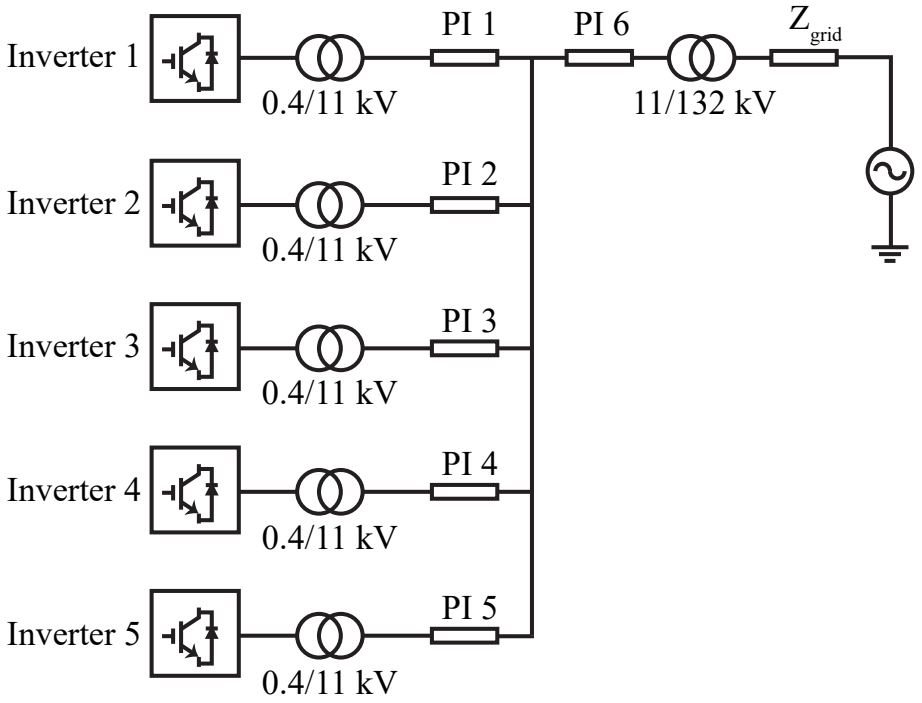

Figure 4.9: Layout of the solar farm

Table 4.1: Cable parameters

Cable	length (km)	R (Ω)	L (H)	C (μF)
PI1	0.31	0.04	1.273E-4	0.152
PI2	0.70	0.09	2.865E-4	0.345
PI3	1.07	0.14	4.138E-4	0.523
PI4	1.44	0.19	5.411E-4	0.704
PI5	1.64	0.21	6.366E-4	0.805
PI6	2.00	0.08	2.690E-4	0.620

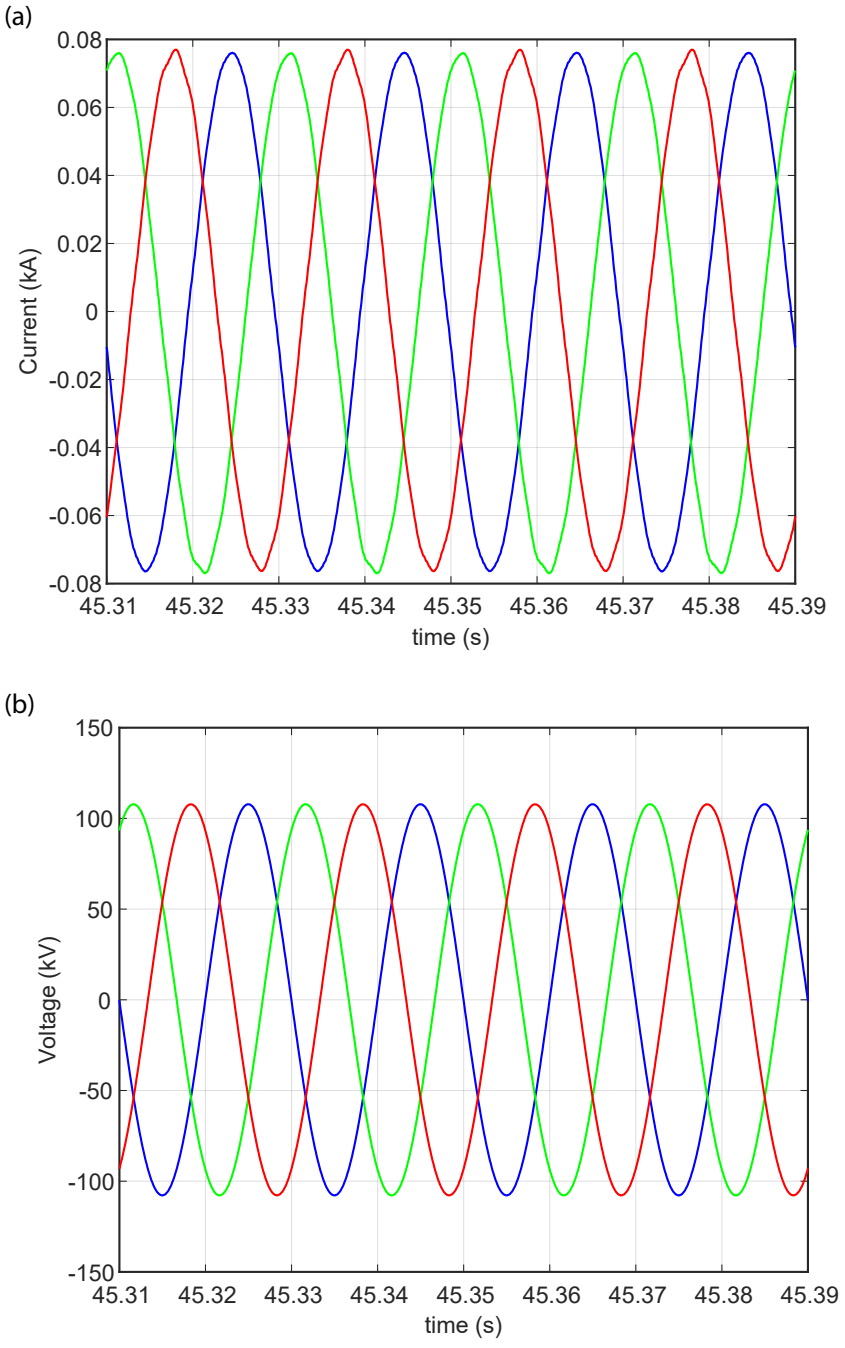

Figure 4.10: (a) Current and (b) voltage waveforms of the solar farm determined at the PCC

4.7 Chapter Summary

It is usually mandatory to carry out harmonic assessments to ensure that the harmonics caused by renewable energy generators such as solar farms comply with the allocated levels. In such harmonic assessment studies, with a view to reduce the computation time, it is the common practice to use frequency domain harmonic models instead of EMT models. To investigate the drawbacks of this process and to carry out the necessary inverter harmonic model development studies, it is required to have a solar farm model which replicates the true behaviour of commercially available solar farm models. To fulfil this necessity, a solar farm model was developed using PSCAD^{TM} software, which consists of five large-scale three-phase inverters. This chapter has mainly focused on developing a single large-scale (2.5 MW) grid-connected three-phase single inverter, followed by the development of a solar farm model with a total rated capacity of 12.5 MW, by incorporating five identical 2.5 MW inverters connected to the high voltage grid via step up transformers and a grid interfacing transformer via an underground cable network.

When developing the solar farm model, not only the parameters of the system, but also the control strategies used in the solar farm model were carefully chosen to replicate a realistic solar farm model. The inverters essentially consist of PI controller based dc link voltage controllers, current controllers and reactive power controllers. SVPWM technique was used as the modulation technique to generate the IGBT switching pulses and a user-defined PSCAD model was developed. The reason for choosing the SVPWM technique among the other well-known modulation techniques such as SPWM, THIPWM and DPWM, is due to its associated advantages, such as resulting in reduced voltage and current THD at the inverter output and efficient utilization of the inverter dc link voltage.

The cable networks of solar farms can be identified as one of the significant features of the developed solar farm model, as it is often neglected when developing grid-connected solar inverter models. The cable network of a solar farm is a crucial component compared to overhead lines, as cables are more likely to cause resonance at lower frequencies. Hence, accurate modelling of the cable network is essential and hence was taken into account in developing the solar farm model.

The current THD observed at the PCC at the rated power level for a single grid-connected inverter system was observed to be 0.786%, which is significantly low. The current and voltage waveforms at the inverter terminals and at the PCC were reported for a single grid-connected inverter operation.

The developed large-scale grid-connected solar farm model will be used in Chapter 5 to develop the corresponding Thevenin/Norton harmonic models and carry out sensitivity studies of using Thevenin/Norton models in the place of inverter EMT models in harmonic studies. Furthermore, the developed grid-connected single inverter model and the solar farm model will be used in deriving mathematical expressions for inverter harmonic

models and inverter harmonic model development based on cross-harmonic generation phenomenon in Chapter 6 and Chapter 7 respectively.

Chapter 5

Inverter Harmonic Model Development and Sensitivity Studies

5.1 Introduction

Inverter manufacturers are known to provide a set of harmonic Norton/Thevenin models of inverters which are known to represent worst-case emissions for each harmonic order. However, inverters are non-linear power electronic devices, and hence the current harmonics injected by them vary depending on their operating power levels and various other internal and external conditions. Hence, it is not possible to derive a unique simplified inverter harmonic model which works for all inverter operating power levels and varying conditions. It is also important to note that the various harmonic current magnitudes do not exhibit a linear relationship with the power output level of an inverter and simple extrapolation is not possible from one power level to another to determine its harmonic currents. Further, the influence of the network within a specific solar plant containing a collection of inverters, the underground cable system and the network external to the solar plant is not represented in the determination of such models carried out under chosen conditions by the manufacturers.

It is extraordinarily challenging to use analytical methods to derive Norton/Thevenin model parameters when dealing with large power electronic systems, and hence one has to resort to the use of numerical and small-signal analysis methods to determine suitable equivalent circuits. Harmonic linearisation is a widely known technique which is used to develop small-signal linear models of time-varying systems [70].

In the studies undertaken, instead of deriving inverter harmonic models corresponding to the worst case scenario of each harmonic under consideration, the harmonic linearisation method is used to determine the inverter harmonic model parameters with the inverter operating at a fixed power level. For this purpose, the EMT model of the inverter system developed in Chapter 4 is injected with perturbing voltage signals from the grid side,

followed by extracting the required voltage or current components at the perturbation frequency to determine the necessary parameters [14], [71].

Once the frequency domain inverter harmonic model parameters are determined, the performance of the inverter EMT models and the frequency domain inverter harmonic models under different inverter internal and external conditions [72] are compared and/or analysed considering, initially, the grid connected single inverter followed by the grid connected multi-inverter solar farm system.

5.2 Determination of the Thevenin/Norton Model Parameters

The Thevenin/Norton model parameters can be determined by superimposing a small harmonic signal on the output side of the inverter and then by extraction of the required voltage or current components at the superimposed frequency. Since the order of significant harmonic components injected by a three-phase inverter are characterised by 6n$\pm$1, only 5^{th}, 7^{th}, 11^{th} and 13^{th} harmonics were considered in addition to the two randomly-picked higher order harmonic orders of 29^{th} and 31^{st} while paying attention to their sequence properties. The total voltage on the grid side can be defined as given in (5.1) and (5.2) considering both positive and negative sequence harmonics stated above.

For a positive sequence perturbation, the total input voltage can be written as,

$$\begin{aligned} v_a(t) &= V_1 sin(2\pi f_1 t) + V_p sin(2\pi f_p t + \theta_p) \\ v_b(t) &= V_1 sin(2\pi f_1 t - \frac{2\pi}{3}) + V_p sin(2\pi f_p t - \frac{2\pi}{3} + \theta_p) \\ v_c(t) &= V_1 sin(2\pi f_1 t - \frac{4\pi}{3}) + V_p sin(2\pi f_p t - \frac{4\pi}{3} + \theta_p) \end{aligned} \tag{5.1}$$

where, V_1, f_1, V_p, f_p and θ_p are fundamental voltage magnitude, fundamental frequency, perturbation voltage magnitude, perturbation frequency and phase angle of the perturbation signal respectively.

For a negative sequence perturbation, the total input voltage can be written as,

$$\begin{aligned} v_a(t) &= V_1 sin(2\pi f_1 t) + V_n sin(2\pi f_n t + \theta_n) \\ v_b(t) &= V_1 sin(2\pi f_1 t - \frac{2\pi}{3}) + V_n sin(2\pi f_n t + \frac{2\pi}{3} + \theta_n) \\ v_c(t) &= V_1 sin(2\pi f_1 t - \frac{4\pi}{3}) + V_n sin(2\pi f_n t + \frac{4\pi}{3} + \theta_n) \end{aligned} \tag{5.2}$$

where, V_n, f_n and θ_n are perturbation voltage magnitude, perturbation frequency and phase angle of the perturbation signal respectively.

The inverter output current that arises as a result of the externally applied perturba-

tion voltage can contain harmonics at different frequencies other than what is injected, due to the non-linear operation of the inverters. Therefore, when determining the inverter harmonic model at a particular frequency, it is mandatory to remove all other harmonic components except the current and voltage component at the harmonic order of perturbation injection, to derive the intended small-signal source voltage and impedance of the inverter.

The inverter harmonic behaviour can be represented using a Norton or a Thevenin model as discussed in Section 2.6. As the inverters inject harmonic currents, it is more realistic to represent the inverters using the corresponding Norton models. However, the Norton model parameters can be converted to the respective Thevenin model parameters easily. Hence, if the inverter harmonic behaviour is represented using a Thevenin equivalent as shown in Figure 5.1, its parameters at the harmonic order (h) of interest can be derived using two independent current and voltage measurements taken at the inverter output terminals in the frequency domain (using FFT analysis), and by applying equation (5.3) [19], [32], [73].

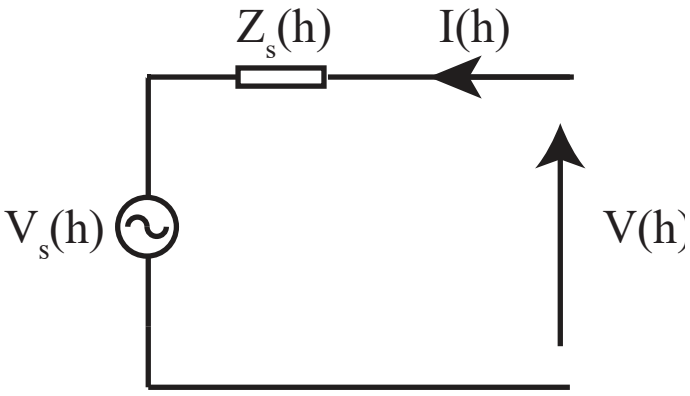

Figure 5.1: Thevenin equivalent model

$$\begin{aligned} V_1(h) &= V_s(h) + Z_s(h)I_1(h) \\ V_2(h) &= V_s(h) + Z_s(h)I_2(h) \end{aligned} \tag{5.3}$$

where, $V_1(h)$ and $V_2(h)$ are the two discrete voltage harmonic components measured at the inverter output terminals corresponding to the two discrete harmonic injection levels applied from the grid side. $I_1(h)$ and $I_2(h)$ are the current harmonics at the considered frequency which flow into the inverter corresponding to those harmonic injection levels, respectively. Hence it is important to note that, the voltage $V(h)$ that appears at the inverter output terminals is a result of the contribution of both the inverter and the background voltage and impedance.

The frequency-dependent Thevenin impedances $Z_s(h)$ and the corresponding source voltage $V_s(h)$ can be derived using the expressions given in (5.4) where it is valid for any two different external signal levels injected assuming the inverter operating conditions

remain unchanged.

$$Z(h) = \frac{V_1(h) - V_2(h)}{I_1(h) - I_2(h)}$$
$$V(h) = \frac{V_2(h)I_1(h) - V_1(h)I_2(h)}{I_1(h) - I_2(h)} \tag{5.4}$$

Voltages with three different magnitudes (1 V, 3 V and 5 V) and for each magnitude, six different phase angles (0°, 60°, 120°, 180°, 240° and 300°) were used as the voltage perturbations injected to examine how the Thevenin equivalent parameters derived using (5.4) vary with the applied voltage perturbations at the inverter rated power level of 2.5 MW. The three different magnitudes of 1 V, 3 V and 5 V were chosen to show the general pattern of the current variation at the inverter output with the applied perturbation voltage from the grid side. Furthermore, the chosen voltage magnitudes were used to test whether the Thevenin equivalent source voltage and the impedance are affected by the applied voltage perturbations. The cable network of the grid-connected inverter system was not used when deriving the Thevenin equivalent parameters since the layout and the parameters of the solar farm cable network are usually not known when determining the inverter harmonic model parameters by the inverter manufacturers in practice.

Figure 5.2 shows the magnitudes of the real and imaginary components of the current ($I(f)$) at the inverter output and Figure 5.3 shows the variation of Thevenin equivalent impedance and source voltage for the different perturbation voltages applied to the system for the 7^{th} harmonic. From Figure 5.3 it is evident that the inverter Thevenin equivalent parameters remain independent of the applied perturbation signal levels or the phase angle. For the 7^{th} harmonic, the derived Thevenin equivalent parameters are:

- Thevenin equivalent impedance = $(0.0276 + 0.0115\text{i})\,\Omega$
- Thevenin equivalent source voltage = $2.932 \times 10^{-4} \angle 131.9^{\circ}$ kV

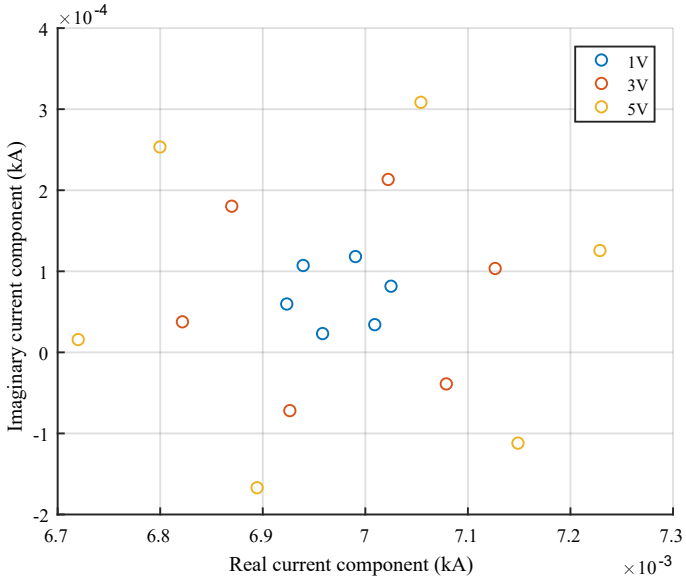

Figure 5.2: Variation of the magnitudes of real and imaginary components of the 7th harmonic current at the inverter terminal for different perturbation voltage levels

Although not shown, behaviour associated with other harmonic orders has similar variations as in Figure 5.2 and Figure 5.3. The Thevenin equivalent parameters derived for the harmonic orders under consideration are given in Table 5.1.

Table 5.1: Thevenin Equivalent Circuit Parameters

harmonic order	Thevenin equivalent source voltage (kV)	Thevenin equivalent impedance (Ω)
5	0.012 + j0.007	$4.357 \times 10^{-4} \angle$ -79.9°
7	0.028 + j0.012	$2.932 \times 10^{-4} \angle$ 131.9°
11	0.011 - j0.046	$1.207 \times 10^{-4} \angle$ -128.4°
13	0.002 - j0.027	$6.775 \times 10^{-5} \angle$ -96.7°
29	2.350×10^{-4} - j0.008	$1.255 \times 10^{-5} \angle$ 122.2°
31	2.243×10^{-4} - j0.008	$1.115 \times 10^{-5} \angle$ -50.0°

To validate the derived Thevenin equivalent models, the EMT model of the inverter system was replaced with the Thevenin equivalent and the harmonic current at the PCC was extracted for each harmonic order. The results are compared with the harmonic currents measured at the PCC with the inverter EMT model connected to the grid and the two sets of observations are given in Table 5.2. From these results, it can be concluded that a single inverter can be confidently replaced by its derived Thevenin model under the assumed inverter conditions.

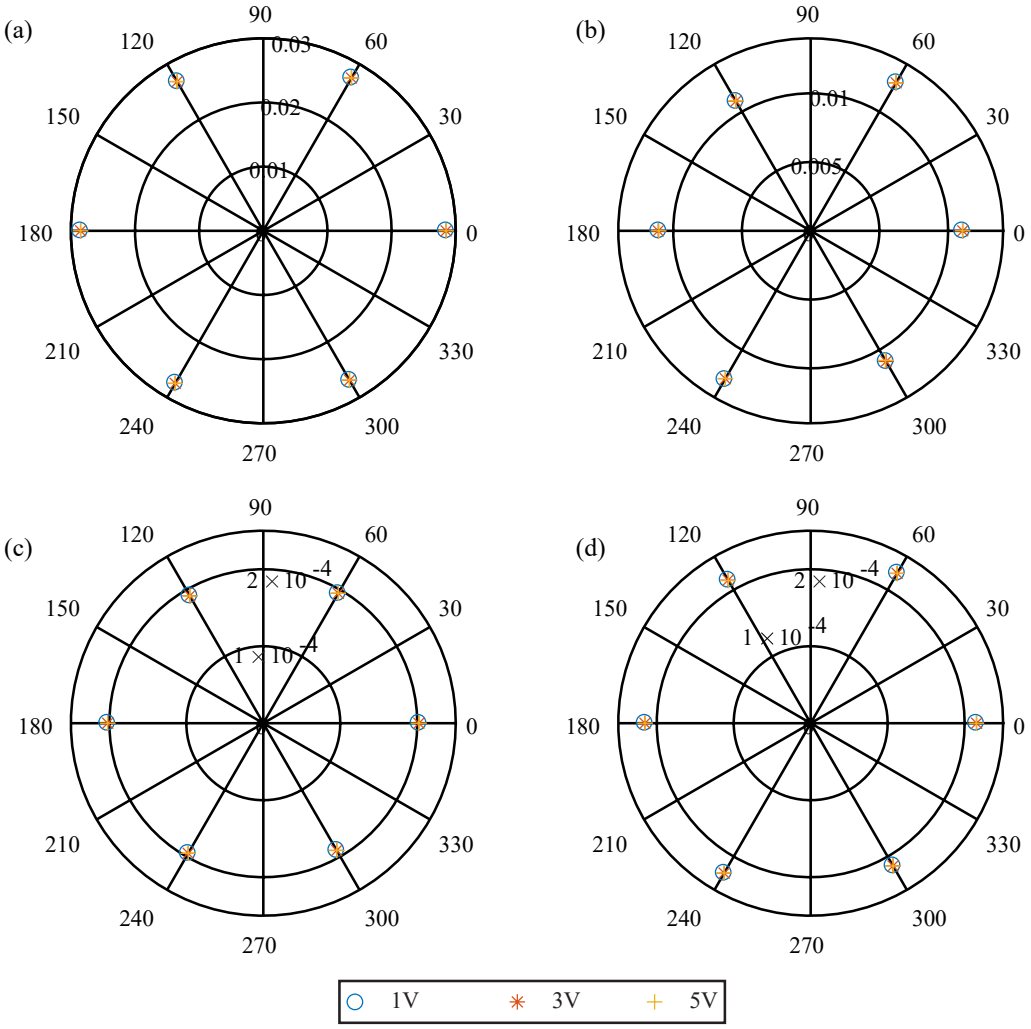

Figure 5.3: Thevenin equivalent source voltage and impedance variation (a) Thevenin equivalent impedance real part (b) Thevenin equivalent impedance imaginary part (c) Thevenin source voltage real part (d) Thevenin source voltage imaginary part

Table 5.2: Harmonic currents at the PCC

harmonic order	with EMT inverter model (kA)	with Thevenin equivalent (kA)
5	5.361×10^{-5}	5.353×10^{-5}
7	2.115×10^{-5}	2.113×10^{-5}
11	1.862×10^{-5}	1.884×10^{-5}
13	2.130×10^{-5}	2.157×10^{-5}
29	5.265×10^{-7}	5.209×10^{-7}
31	4.239×10^{-7}	4.266×10^{-7}

5.3 Performance of the Thevenin Model With the Cable Network - With Variable Cable Lengths

As stated in Section 5.1, the frequency domain inverter harmonic model parameters are usually determined by the manufacturers under specific test conditions considering the worst-case scenarios where the impact of the actual external network to which the inverter is finally connected is not represented. Similarly, the Thevenin model parameters given in Table 5.1 also do not take into account any impedance elements, such as those of the cables external to the inverter. For this reason, there is no certainty that such equivalent harmonic models are able to replicate the true harmonic behaviour when the actual inverters are used together with external cable networks and the external grid.

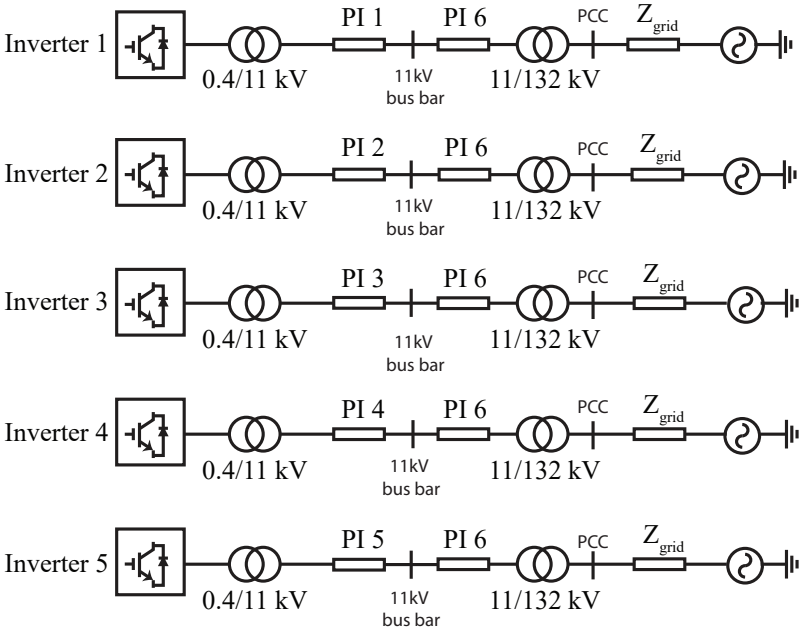

Figure 5.4: Each inverter EMT model connected to the grid with the external cable network

To examine the influence of the external cable network on the harmonic performance of the inverter EMT models and the Thevenin models, each inverter was individually connected to the grid with the corresponding cable that is connected to the secondary of the inverter step up transformer and the 11 kV bus bar (to which other inverters are to be finally connected in the solar farm environment) and the cable between the 11 kV bus bar to the grid interfacing 11 kV/132 kV transformer thus, giving five combinations as shown in Figure 5.4. Noting that the different inverters are geographically dispersed in solar farm environments, in the above set-up, inverter 1 is the closest to the 11 kV bus bar, whereas inverter 5 is the furthest from the 11 kV bus bar. This results in 5 different cable lengths, from the inverter step-up transformer to the grid connection transformer (i.e. 2.31, 2.70,

3.07, 3.44 and 3.64 km). This allows the examination of the dependency of harmonic behaviour of the EMT and the developed frequency domain inverter models on different cable capacitance values which are associated with the different cable lengths.

In the study with EMT models of the inverters, the current harmonics at the PCC were extracted from the current injected into the grid. In order to determine up to what extent the Thevenin model of an inverter can replicate the harmonic currents injected by the inverter EMT models, the same procedure was repeated, replacing the inverter EMT model with the corresponding Thevenin equivalent circuits of which the parameters are given for each harmonic order in Table 5.1. This analysis was carried out for 5^{th}, 7^{th}, 11^{th} and 13^{th} harmonics, which are the most significant harmonics in three-phase inverters. The outcomes of this study are shown in Figure 5.5.

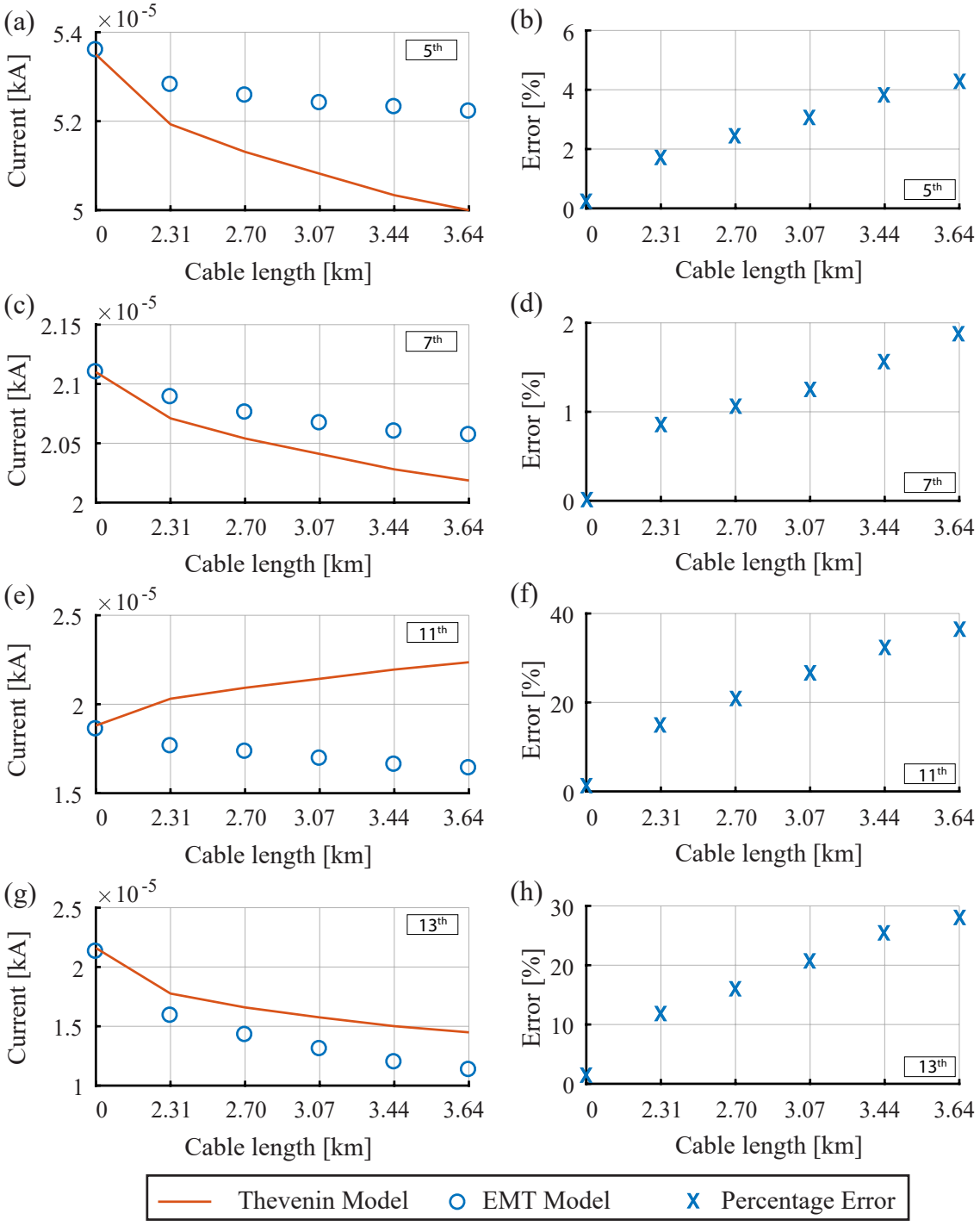

Figure 5.5: Harmonic current magnitudes at the PCC with different cable lengths and their error percentages (a) 5th harmonic current (b) percentage error for the 5th harmonic current (c) 7th harmonic current (d) percentage error for the 7th harmonic current (e) 11th harmonic current (f) percentage error for the 11th harmonic current (g) 13th harmonic current (h) percentage error for the 13th harmonic current

For the purpose of comparison associated with the influence of the cable network, the same investigation was repeated without the solar farm cables, where the corresponding results correspond to '0' on the abscissa in Figure 5.5. With the EMT models of inverters, the harmonic currents at the PCC are seen to decrease with increasing cable lengths of

the system. Taking these as reference values, the absolute errors associated with the harmonic currents determined using Thevenin models are shown in Figures 5.5 (b), (d), (f), and (h). It is seen that although 5^{th} and 7^{th} harmonic currents are underestimated when the Thevenin models are used, the associated error can be accepted for practical purposes. For the 11^{th} harmonic, current variation predicated by the two approaches illustrates contradictory behaviours and also illustrates an unacceptable error as the cable length increases. For the 13^{th} harmonic current, although the trends predicted by the two approaches are similar, the error associated is unacceptable as for the 11^{th} harmonic current. These significant deviations are closely examined next and broad conclusions are reached.

5.3.1 Analysis of Results and Conclusions

Noting that the harmonic current emission behaviour of an inverter can be impacted by impedance variations external to the inverter, e.g. possible resonant conditions, impedance scans were undertaken considering both EMT models and the Thevenin models (given in Table 5.1) of inverter 1 and inverter 5 noting that they are associated with the shortest and the longest cable lengths). Figure 5.6 illustrates the various impedance scans where Figure 5.6 (a) represents the impedance scan of the system external to the output terminals of the two inverters indicating an inductive behaviour. This supports the decreasing trend of the harmonic currents observed with the EMT models as illustrated in Figures 5.5 for all considered harmonics.

Considering the anomaly associated with the 11^{th} harmonic current observed with the corresponding Thevenin model, where the current was seen to increase with increasing cable length, additional harmonic scans were carried out by incorporating the individual Thevenin impedances in the frequency scans to examine the existence of resonance conditions. Figure 5.6 (b) illustrates the outcomes of the frequency scan with the 5^{th} harmonic Thevenin impedance exhibiting an inductive behaviour. This was the case with the 7^{th} harmonic Thevenin impedance as well, although not shown. However, this is not the case with both 11^{th} and 13^{th} Thevenin impedances as illustrated in Figures 5.6 (c) and (d) respectively which demonstrate series resonant conditions where the resonant frequencies are seen to lie within 9^{th} and 15^{th} harmonics.

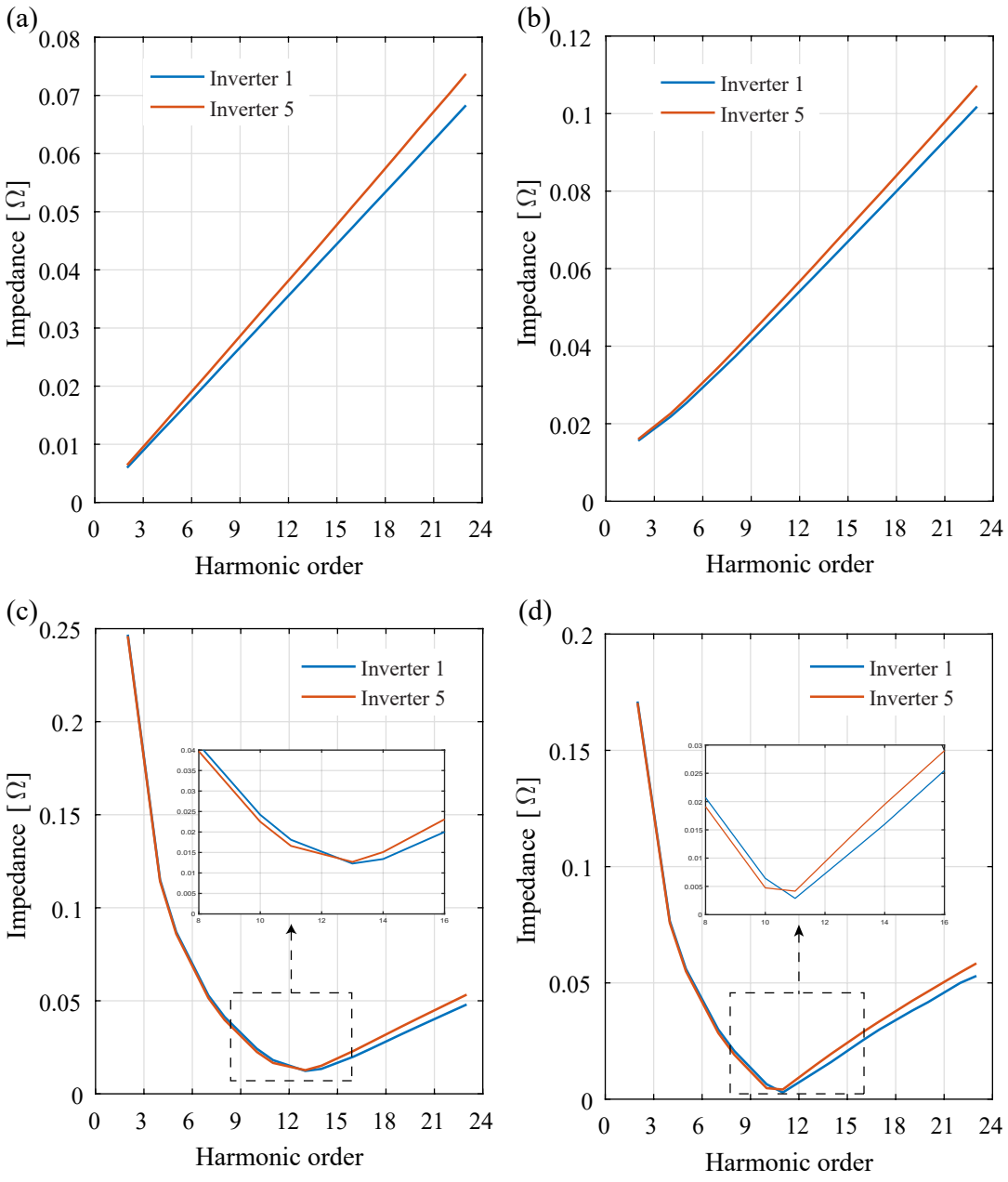

Figure 5.6: Impedance scans (a) conducted at the output terminals of the inverter EMT model (b) with the 5^{th} harmonic Thevenin impedance (c) with the 11^{th} harmonic Thevenin impedance (d) with the 13^{th} harmonic Thevenin impedance

Referring to Figure 5.6 (c), it can be seen that the resonance frequencies associated with both inverter 1 and inverter 5 lie to the right of the 11^{th} harmonic. As the cable length is increased from the shortest to the longest, the net impedance seen by the 11^{th} harmonic Thevenin voltage source decreases, leading to an increase in the corresponding harmonic current. Referring to Figure 5.6 (d), it can be seen that the resonance frequencies associated with both inverter 1 and inverter 5 lie to the left of the 13^{th} harmonic. As the cable length is increased from the shortest to the longest, the net impedance seen by the 13^{th} harmonic Thevenin voltage source increases leading to a decrease in the corresponding harmonic current. These observations are supported with numerical calculations given in

Appendix B.

This preliminary study illustrated possible drawbacks in the use of Thevenin equivalent models in harmonic studies. The interaction of Thevenin equivalent parameters with the external system parameters can exhibit unexpected behaviours leading to inaccurate results in harmonic studies. Furthermore, the Thevenin models, which are derived without considering external cable networks may not exactly replicate the actual inverter harmonic emission behaviour in the presence of external elements such as cable networks within the generating installations.

5.4 Performance of Thevenin Models of Inverters Operating with Reactive Power Injection/Absorption

Grid codes and applicable connection requirements often tend to stipulate reactive power injection/absorption requirements on generators. One such example is the National Electricity Rules (NER) [28] where the minimum reactive power requirement is given by 0.395 times rated active power. Considering the 2.5 MVA inverters (2.5 MW at unity power factor) in the present case, this amounts is 0.9875 MVAr (both leading and lagging). However, several reactive power injection/absorption levels were used with a single inverter, i.e. 0.5 MVAr, 0.75 MVAr and 0.98 MVAr, with the corresponding curtailed real power levels of 2.44 MW, 2.38 MW and 2.30 MW. Both single and multi-inverter arrangements connected to the common 11 kV bus bar interfaced with the 132 kV grid are considered where the current harmonics injected at the PCC by the inverter EMT models are compared with those obtained using the inverter Thevenin models.

As the Thevenin model parameters vary with different inverter operating conditions (e.g. output power levels), the corresponding parameters need to be determined. Although in the present study it was the case, in practice, the inverter manufacturers provide only a fixed set of Thevenin/Norton model parameters for each harmonic of interest, considering the worst-case scenario from a harmonic perspective measured over a range of power levels. Hence, such parameters tend to have statistical significance and may not represent the true harmonic performance of an inverter referred to a specific operating condition.

5.4.1 0.5 MVAr of Reactive Power Injection/Absorption

The Thevenin model parameters determined with a single inverter operating at 0.5 MVAr of reactive power injection and absorption modes are given in Table 5.3 and Table 5.4 respectively. It is to be noted that these Thevenin model parameters were determined by neglecting the cable network of the system so that the influence of the cable network on the inverter Thevenin models can be removed.

Table 5.3: Inverter Thevenin equivalent circuit parameters with P = 2.44 MW and Q = 0.5 MVAr

Harmonic order	Thevenin equivalent impedance (Ω)	Thevenin equivalent source voltage (kV)
5	0.0115 + j0.0068	$2.487 \times 10^{-4} \angle$ -134.4°
7	0.0266 + j0.0108	$1.036 \times 10^{-5} \angle$ 133.4°
11	0.0118 - j0.0468	$1.119 \times 10^{-4} \angle$ 89.4°
13	0.0017 - j0.0273	$5.226 \times 10^{-5} \angle$ 116.4°
29	2.336×10^{-4} - j0.008	$1.036 \times 10^{-5} \angle$ 133.4°
31	2.218×10^{-4} - j0.007	$1.198 \times 10^{-5} \angle$ -59.5°

Table 5.4: Inverter Thevenin equivalent circuit parameters with P = 2.44 MW and Q = -0.5 MVAr

Harmonic order	Thevenin equivalent impedance (Ω)	Thevenin equivalent source voltage (kV)
5	0.0116 + j0.0078	$6.879 \times 10^{-4} \angle$ -42.2°
7	0.0276 + j0.0125	$1.555 \times 10^{-4} \angle$ -27.2°
11	0.0108 - j0.0450	$2.879 \times 10^{-4} \angle$ -42.2°
13	0.0021 - j0.0268	$1.142 \times 10^{-5} \angle$ -44.8°
29	2.407×10^{-4} - j0.008	$8.277 \times 10^{-6} \angle$ 124.2°
31	2.276×10^{-4} - j0.007	$1.344 \times 10^{-5} \angle$ -44.82°

For both cases, the grid current observed at the PCC with inverter EMT models and Thevenin models are shown in Figure 5.7 and Figure 5.8 together with corresponding percentage error levels.

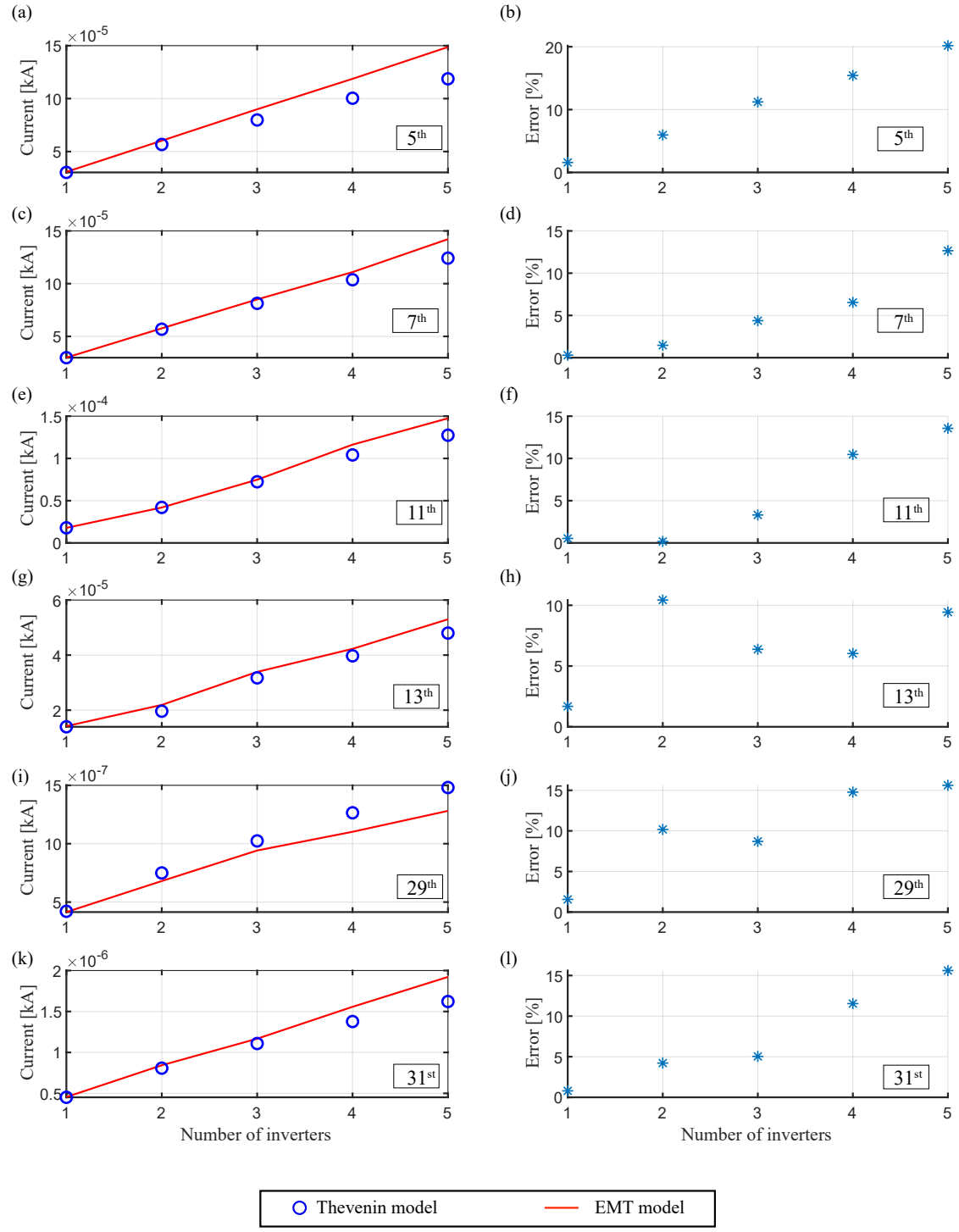

Figure 5.7: The variation of the harmonic current levels at the PCC for different harmonic orders with the number of inverters when the inverters operate at P = 2.44 MW and Q = 0.5 MVAr

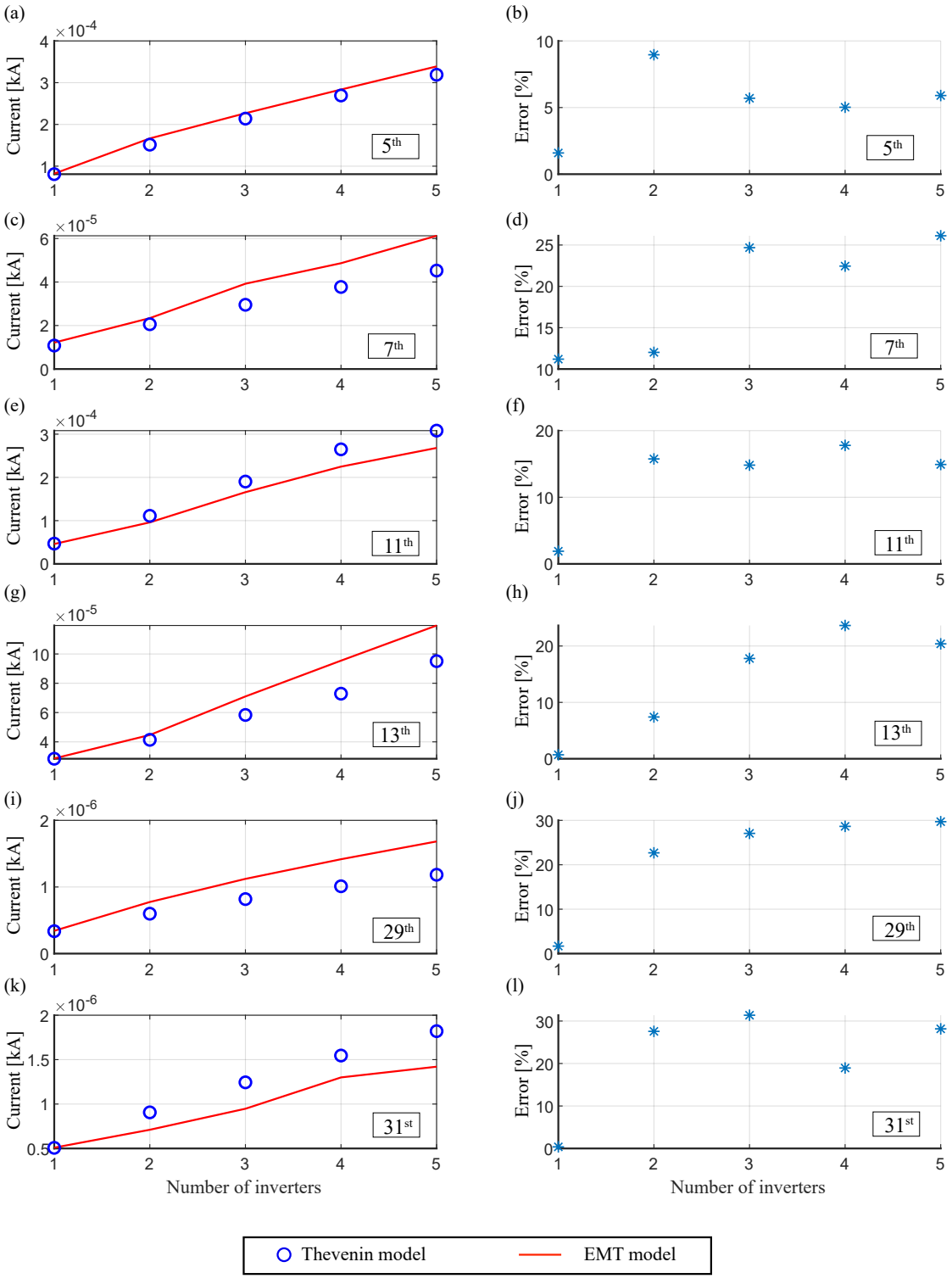

Figure 5.8: The variation of the harmonic current levels at the PCC for different harmonic orders with the number of inverters when the inverters operate at P = 2.44 MW and Q = -0.5 MVAr

Analysis of the Results

From the results presented in Figure 5.7 and Figure 5.8, it is evident that as the number of inverters connected to the grid increases, the percentage error levels associated with the

harmonic currents predicted using the Thevenin models are seen to increase.

5.4.2 0.75 MVAr Reactive Power Injection/Absorption

Similar to the previous case described in Section 5.4.1, the Thevenin model parameters determined when the inverters operate with 0.75 MVAr of reactive power injection and absorption modes are given in Table 5.5 and Table 5.6 respectively. As in the previous case (in Section 5.4.1), the cable network was left out when determining the inverter Thevenin model parameters.

Table 5.5: Inverter Thevenin equivalent circuit parameters with P = 2.38 MW and Q = 0.75 MVAr

Harmonic order	Thevenin equivalent impedance (Ω)	Thevenin equivalent source voltage (kV)
5	0.0120 + j0.0058	$1.267 \times 10^{-4} \angle 169.8°$
7	0.0240 + j0.0091	$3.048 \times 10^{-4} \angle 143.6°$
11	0.0134 - j0.0464	$8.604 \times 10^{-5} \angle 1.7°$
13	0.0035 - j0.0267	$5.797 \times 10^{-5} \angle$ -2.9°
29	2.381×10^{-4} - j0.0082	$1.078 \times 10^{-5} \angle 116.3°$
31	2.283×10^{-4} - j0.007	$1.237 \times 10^{-5} \angle$ -48.71°

Table 5.6: Inverter Thevenin equivalent circuit parameters with P = 2.38 MW and Q = -0.75 MVAr

Harmonic order	Thevenin equivalent impedance (Ω)	Thevenin equivalent source voltage (kV)
5	0.0135 + j0.0060	$7.839 \times 10^{-4} \angle$ -39.5°
7	0.0274 + j0.0124	$2.590 \times 10^{-4} \angle 28.9°$
11	0.0013 - j0.0298	$2.419 \times 10^{-5} \angle$ -179.5°
13	0.0028 - j0.0277	$1.639 \times 10^{-4} \angle 73.2°$
29	2.305×10^{-4} - j0.008	$1.429 \times 10^{-5} \angle 76.3°$
31	4.222×10^{-4} - j0.007	$3.111 \times 10^{-6} \angle$ -0.9°

For both cases, the grid current observed at the PCC with inverter EMT models and Thevenin models for the considered harmonic orders are shown in Figure 5.9 and Figure 5.10 together with corresponding percentage error levels.

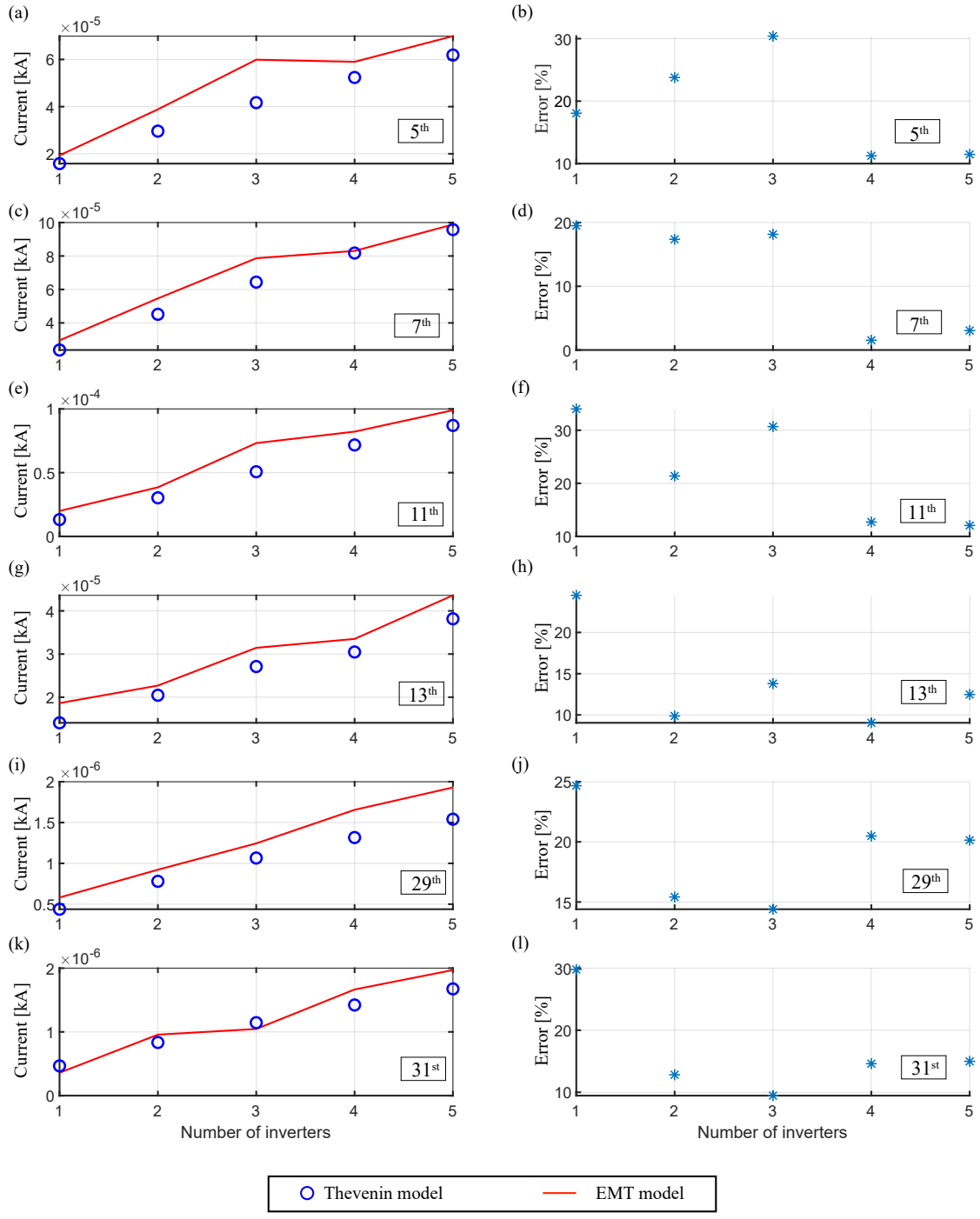

Figure 5.9: The variation of the harmonic current levels at the PCC for different harmonic orders with the number of inverters when the inverters operate at P = 2.38 MW and Q = 0.75 MVAr

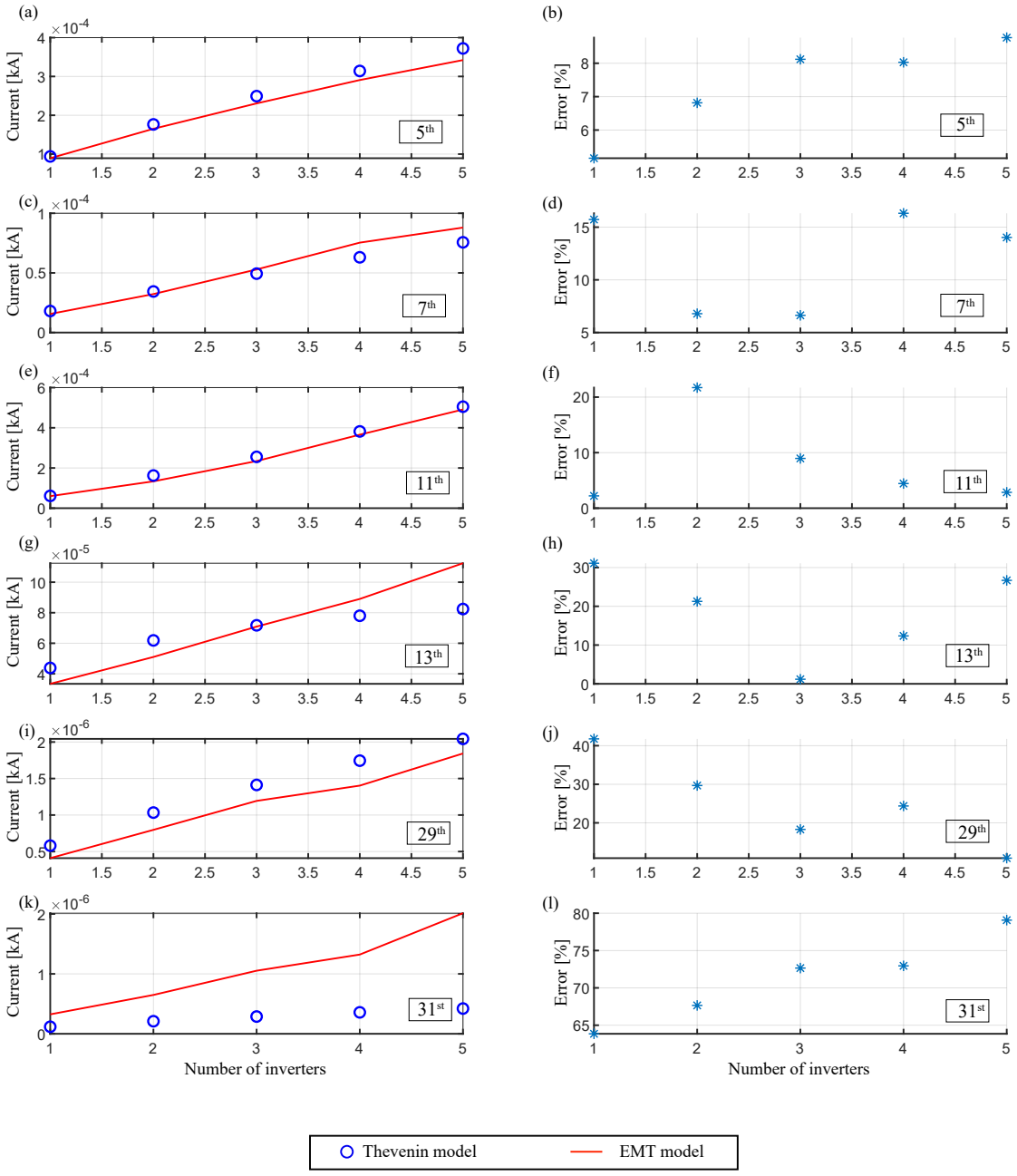

Figure 5.10: The variation of the harmonic current levels at the PCC for different harmonic orders with the number of inverters when the inverters operate at P = 2.38 MW and Q = -0.75 MVAr

Analysis of the Results

From Figure 5.9, it can be observed that for all harmonic orders, the percentage error levels are quite high, even in the case of the single grid connected inverter. The same can be observed based on the results presented in Figure 5.10 and hence, it can be concluded that for the considered cases, the Thevenin models cannot replicate the harmonic performance predicted by the EMT models.

5.4.3 0.98 MVAr Reactive Power Injection/Absorption

In this scenario, the harmonic currents generated by the inverters at the PCC were evaluated considering three different cases.

- Case 1: Each inverter operating at P = 2.3 MW and Q = 0 MVAr reactive power
- Case 2: Each inverter operating at P = 2.3 MW and Q = +0.98 MVAr reactive power
- Case 3: Each inverter operating at P = 2.3 MW and Q = -0.98 MVAr reactive power

For each case, the corresponding Thevenin model parameters were determined at the corresponding power levels in the absence of the cable network (as in the cases covered in Sections 5.4.1 and 5.4.2). For each of the three cases above, the determined Thevenin model parameters are given in Table 5.7, Table 5.8 and Table 5.9.

Table 5.7: Inverter Thevenin equivalent circuit parameters for case 1

Harmonic order	Thevenin equivalent impedance (Ω)	Thevenin equivalent source voltage (kV)
5	0.0112 + j0.0069	$4.688 \times 10^{-4} \angle$ -74.3°
7	0.0270 + j0.0107	$2.478 \times 10^{-4} \angle$ -128.6°
11	0.0111 - j0.0469	$1.534 \times 10^{-4} \angle$ -114.2°
13	0.00216 - j0.0271	$7.916 \times 10^{-5} \angle$ -78.9°
29	2.362×10^{-4} - j0.0082	$1.055 \times 10^{-5} \angle$ 118.9°
31	1.969×10^{-4} - j0.0076	$9.870 \times 10^{-6} \angle$ -45.1°

Table 5.8: Inverter Thevenin equivalent circuit parameters for case 2

Harmonic order	Thevenin equivalent impedance (Ω)	Thevenin equivalent source voltage (kV)
5	0.0120 + j0.0064	$2.659 \times 10^{-4} \angle$ 144.8°
7	0.0240 + j0.0093	$4.259 \times 10^{-4} \angle$ 131.7°
11	0.0142 - j0.0471	$1.716 \times 10^{-4} \angle$ 25.1°
13	0.0026 - j0.0278	$7.147 \times 10^{-5} \angle$ 19.9°
29	2.597×10^{-4} - j0.0082	$5.340 \times 10^{-6} \angle$ 76.1°
31	2.289×10^{-4} - j0.0076	$1.649 \times 10^{-5} \angle$ -39.3°

Table 5.9: Inverter Thevenin equivalent circuit parameters for case 3

Harmonic order	Thevenin equivalent impedance (Ω)	Thevenin equivalent source voltage (kV)
5	0.0119 + j0.0066	$7.199 \times 10^{-4} \angle$ -11.7°
7	0.0291 + j0.0152	$2.989 \times 10^{-4} \angle$ 96.8°
11	0.0108 - j0.0444	$2.808 \times 10^{-4} \angle$ 71.0°
13	0.0021 - j0.0266	$1.068 \times 10^{-4} \angle$ 131.4°
29	2.381×10^{-4} - j0.0082	$9.164 \times 10^{-6} \angle$ 102.3°
31	2.282×10^{-4} - j0.0076	$9.155 \times 10^{-6} \angle$ -35.8°

For the three cases considered, the harmonic current magnitudes observed at the PCC with the inverter EMT models and the corresponding Thevenin models are shown in Figure 5.11, Figure 5.12 and Figure 5.13 respectively together with the associated percentage error levels.

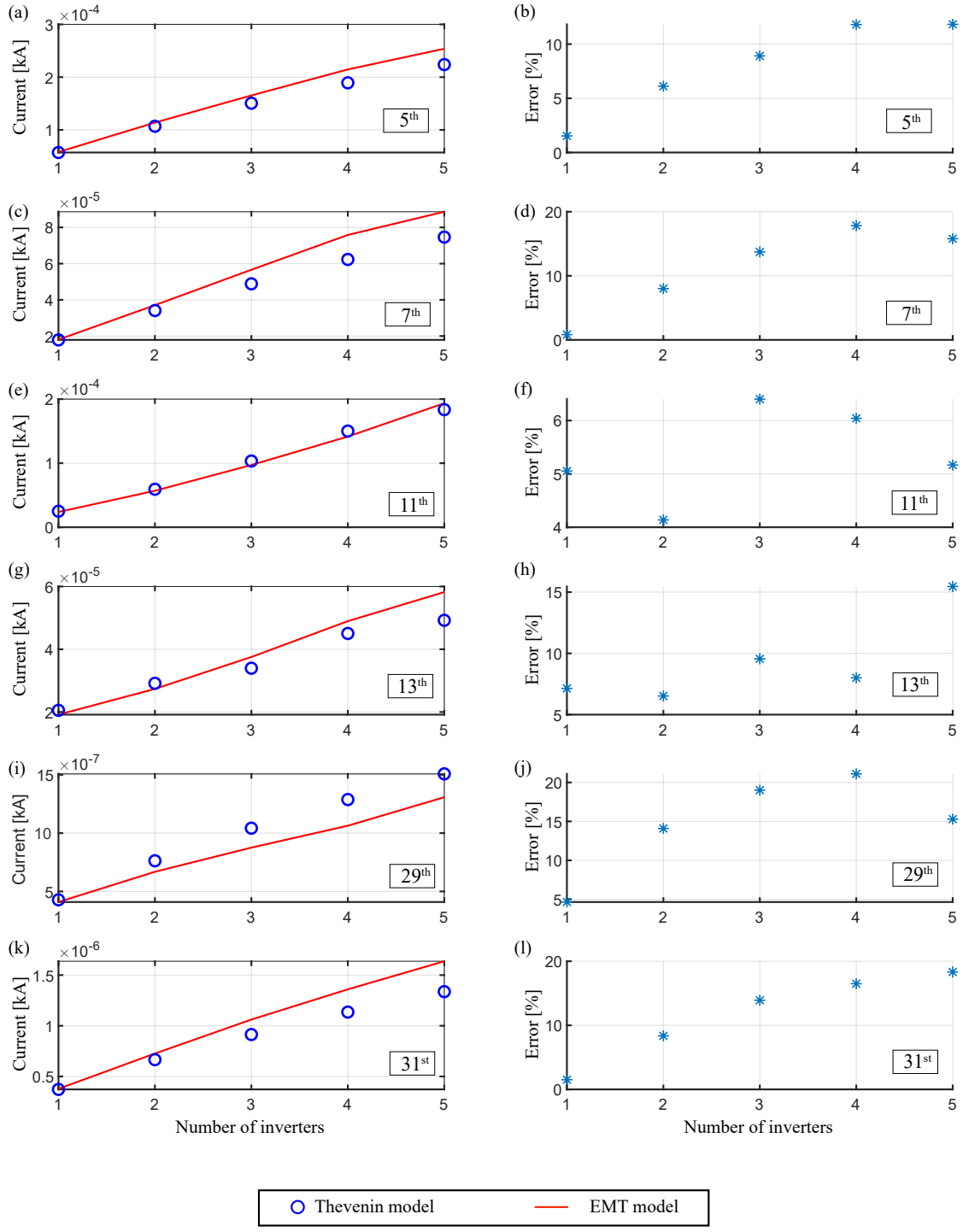

Figure 5.11: The variation of the harmonic current levels at the PCC for different harmonic orders with the number of inverters when the inverters operate at P = 2.3 MW and Q = 0 MVAr

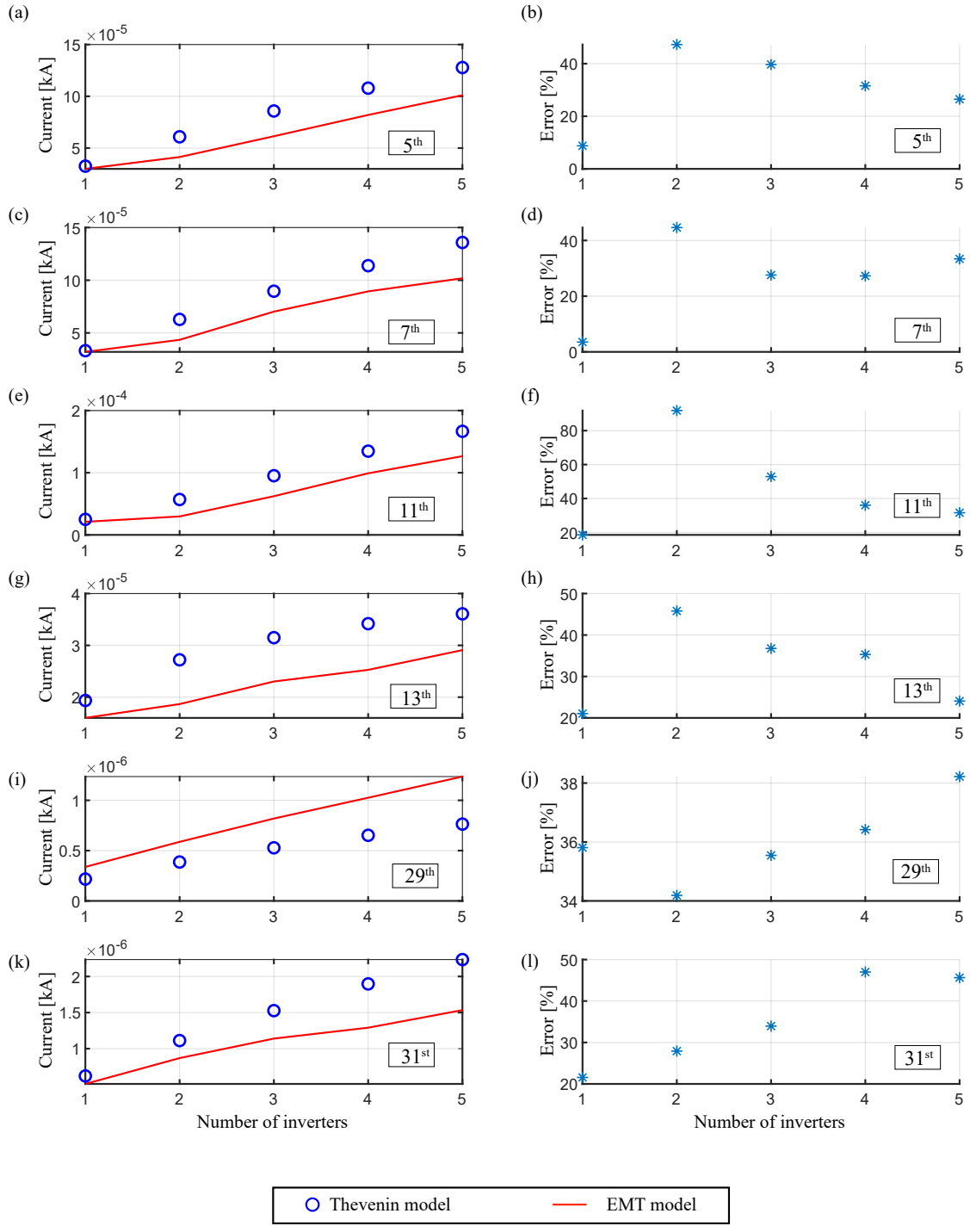

Figure 5.12: The variation of the harmonic current levels at the PCC for different harmonic orders with the number of inverters when the inverters operate at P = 2.3 MW and Q = 0.98 MVAr

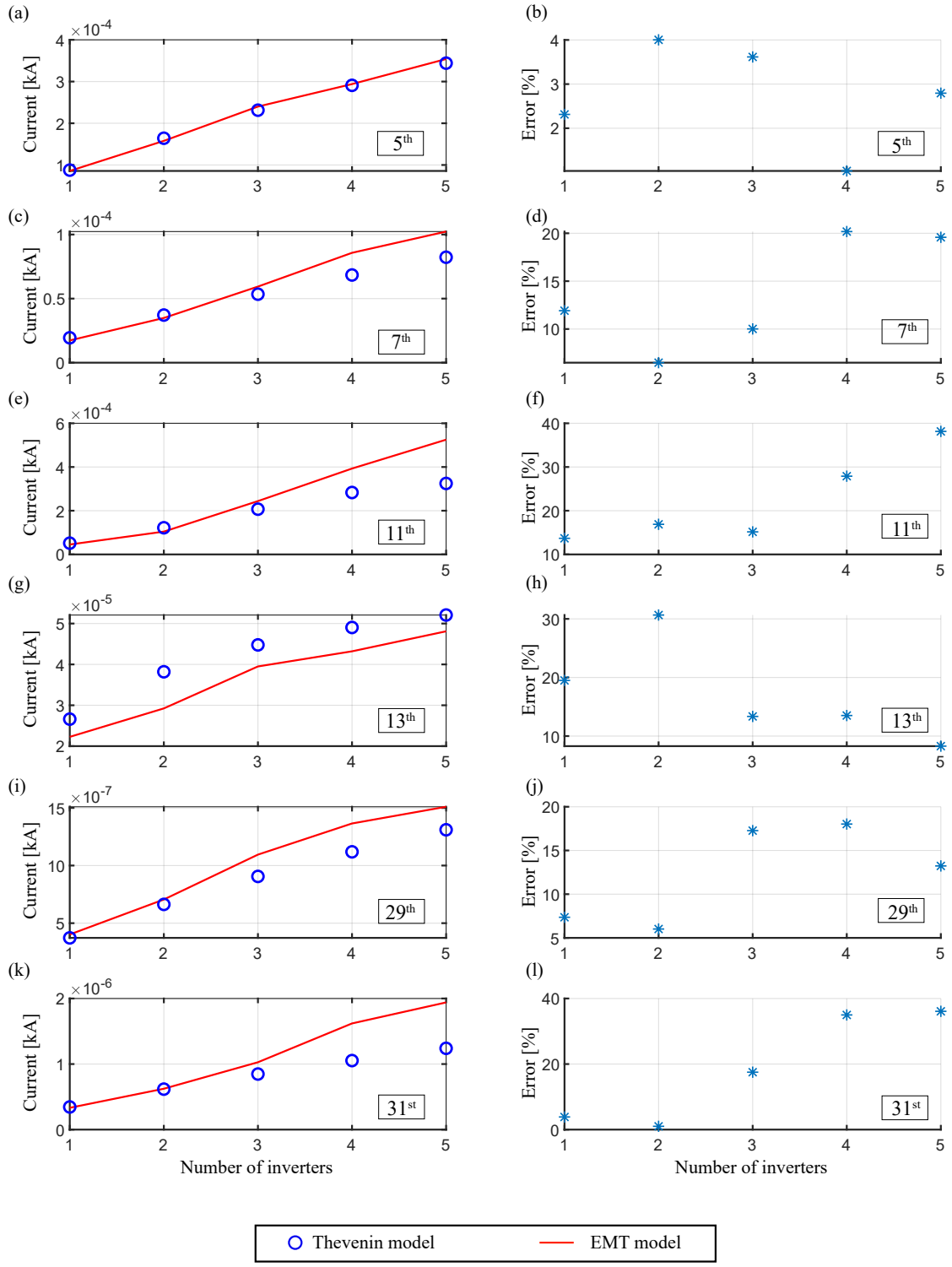

Figure 5.13: The variation of the harmonic current levels at the PCC for different harmonic orders with the number of inverters when the inverters operate at P = 2.3 MW and Q = -0.98 MVAr

Analysis of the Results

Based on the Thevenin model parameters determined for the three cases that are given in Tables 5.7, 5.8 and 5.9, it is evident that, although grid-connected inverters operate at a

particular active power level, depending on the reactive power level, the corresponding harmonic model parameters vary where the variation associated with Thevenin voltage levels far outweigh the variations associated with the Thevenin impedances.

From the results presented, it can be seen that for the case where the inverters operate with an active power of 2.3 MW and zero reactive power, for all the considered harmonic orders, the percentage error levels stay below 20% approximately even when the number of inverters is increased up to five.

When the inverters are controlled such that each of the inverters injects/absorbs a reactive power of 0.98 MVAr, the error percentages show higher values compared to case 1. When the inverters are in the reactive power injection mode (case 2), the error percentages are observed to be higher than when the inverters are operating at 0.98 MVAr reactive power absorption mode (case 3). Most importantly, the error percentages for both cases 2 and 3 have upward trends with the increasing number of inverters. Hence it is apparent that, in a practical solar farm, where the number of inverters connected is far greater than the maximum number of inverters considered in this study, the resulting error can become substantial.

When the 0.5 MVAr, 0.75 MVAr and 0.98 MVAr reactive power injection scenarios are considered, comparing the results shown in Figures 5.7, 5.9 and 5.12, the error percentages seem to increase with the increasing reactive power level.

5.5 Variation of the Current Harmonics at the PCC With Different Fault Levels

In the developed grid-connected solar farm model (refer to Section 4.2.4 of Chapter 4), the fault level at the PCC was 2133 MVA with an X/R ratio of 5 (calculated based on the fundamental frequency). In this section, the fault level at the PCC was varied while maintaining the same X/R to examine its influence on harmonic performance. With the original fault level of 2132.7 MVA denoted as 'FL', the grid impedances were adjusted to represent cases of FL*5, FL*3, FL*0.1 and FL*0.3. In this test, the inverters were controlled such that each inverter injected 0.98 MVAr of reactive power to the grid. Furthermore, the cable network of the solar farm was included in the studies. Since the inverter internal parameters are kept constant, the inverter harmonic model parameters were selected to be the same as the Thevenin model parameters given in Table 5.8. With the inverters operating under the described conditions, the harmonic currents injected by the inverter models at the PCC are compared by employing the Thevenin models and the EMT models, as illustrated in Figure 5.14.

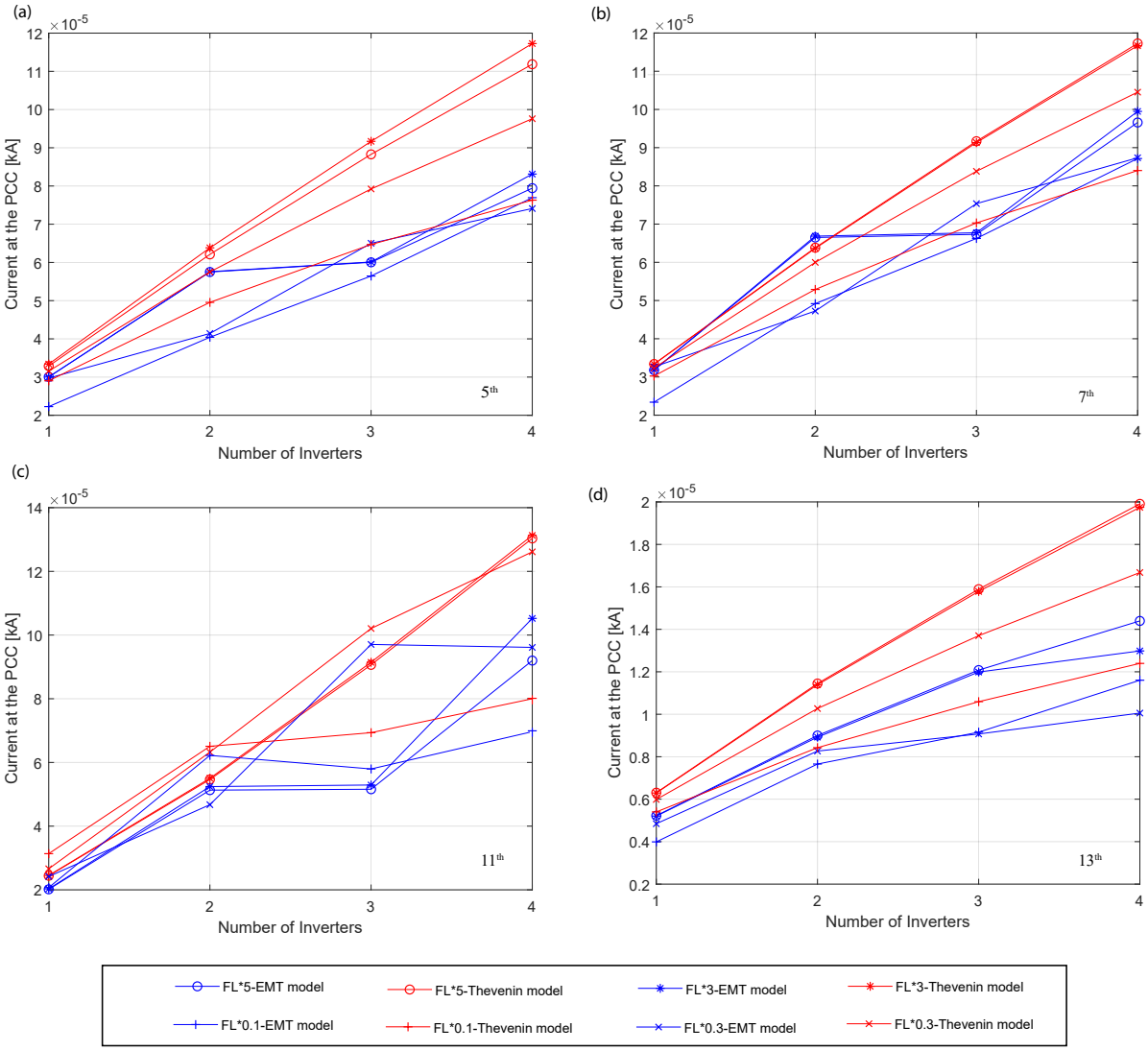

Figure 5.14: Harmonic currents observed for different grid fault levels at the PCC for the harmonic orders of (a)5^{th} (b)7^{th} (c)11^{th} and (d) 13^{th}

5.5.1 Analysis of the Results

From Figure 5.14, it can be seen that for some cases, the EMT simulation results show a reduction in harmonic current magnitudes with increasing number of inverters. This implies that the current injected by the inverters may vary depending on the grid conditions, inverter operating conditions and the number of inverters connected in parallel. Even though the error percentages have not been presented here for each considered fault level, from the results, it can be seen that for most of the cases, the harmonic currents at the PCC determined using the EMT simulation results do not agree with those currents observed employing the Thevenin models.

5.6 Variation of the Current Harmonics at the PCC With Unbalanced Grid Voltages

The grid voltage unbalance can occur due to a number of reasons where such unbalance can be expected to influence the harmonics injected by grid connected inverters and the aim of this section is to examine this impact with the unbalanced grid conditions and with the cable network, when the inverters operate at unity power factor at the rated power level.

The fundamental frequency grid voltage unbalance was represented considering two cases with the following phase voltages:

- Case 1: V_a = 0.95 pu, V_b=1 pu, V_c =1 pu
- Case 2: V_a = 1.05 pu, V_b=1 pu, V_c =1 pu

With the above unbalanced voltages, EMT models of the inverters were used to examine the variation of the positive sequence harmonic currents at the PCC as illustrated in Figure 5.15. In addition, the results obtained using Thevenin models (using the parameters given in Table 5.1) and the EMT models of the inverters under balanced grid voltage conditions are also shown for comparison purposes. The results determined with the Thevenin models for Case 1 and Case 2 are almost identical to the results obtained using the Thevenin models under balanced grid voltage conditions. Taking the results obtained using EMT simulations of the inverters for each condition (balanced grid voltage condition, Case 1 and Case 2) as the reference, the percentage error levels associated with the above two cases and the balanced grid voltage condition are also illustrated in Figure 5.15.

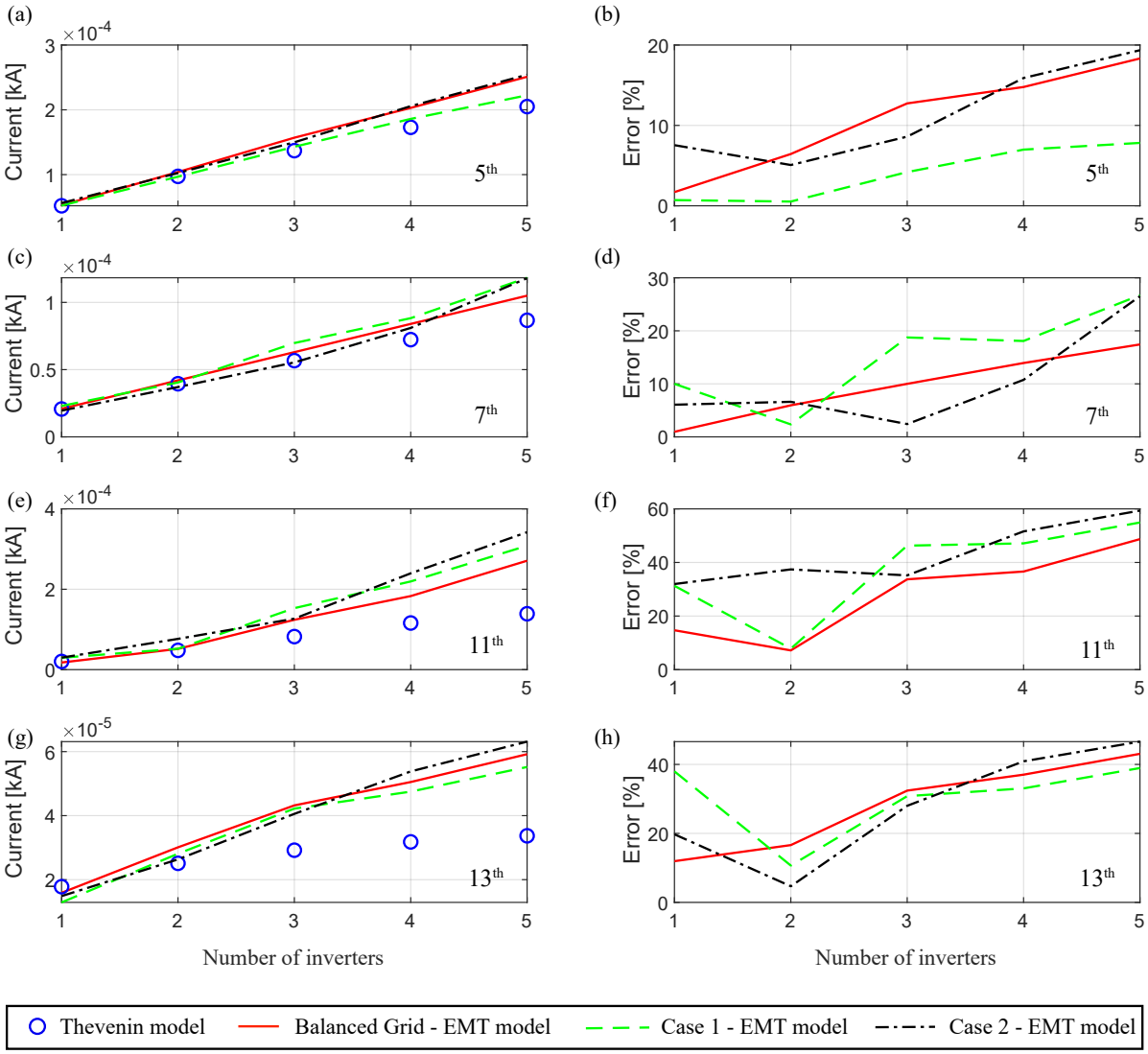

Figure 5.15: Harmonic currents at the PCC observed with balanced and unbalanced grid conditions and their percentage error levels: (a) and (b) 5^{th}, (c) and (d) 7^{th}, (e) and (f) 11^{th}, and (g) and (h) 13^{th} harmonic orders

5.6.1 Analysis of the Results

The results show that the percentage errors for the considered 2 cases increase as the number of inverters increases. Furthermore, the effect of the unbalanced grid voltage on the harmonic current generation is comparably low (compared to the results with the balanced grid condition) and it can be clearly seen by observing the harmonic current magnitudes variations shown in Figure 5.15 (a), (c), (e) and (g). Still, for all three (grid balanced and unbalanced) cases and for the considered harmonic orders, the Thevenin models fail to replicate the true harmonic behaviour of the inverters.

5.7 Variation of the Harmonic Currents at the PCC With Balanced Background Harmonic Voltages

5.7.1 Inverter Harmonic Models Performance With a Single Background Harmonic Voltage

Background harmonic voltages in electricity grids can influence the harmonic performance of inverters and hence entire solar farm connections, where such harmonic levels are not known unless measurements are carried out. Further, these levels vary daily, weekly and seasonally. The manufacturer provided Thevenin/Norton model parameters are usually determined under controlled grid harmonic conditions; however, their influence on the harmonic model parameters is usually unknown as it is nearly impossible to materialise pure grid conditions in testing inverters.

Since the practical worst-case inverter Norton model parameter determination process is not very well known, in this study, the performance of the derived inverter Norton models of the developed three-phase inverter model were investigated when the grid is polluted with 5^{th}, 7^{th}, 11^{th}, 13^{th}, 29^{th} and 31^{st} voltage harmonics. For simplicity, firstly, only a single harmonic voltage was assumed to be present in the grid at a time, and the current harmonics that arose at the PCC were observed at the corresponding harmonic order. The number of inverters connected to the grid was increased from one to five, and the study was carried out with both inverter EMT models and the corresponding inverter Thevenin models. Since the magnitudes of the background grid voltage harmonic orders are not usually known until measurements are carried out, to investigate the worst-case harmonic outcomes, the planning levels [26] of 5^{th}, 7^{th}, 11^{th}, 13^{th}, 29^{th} and 31^{st} harmonics were selected as 2%, 2%, 1.5%, 1.5%, 0.59% and 0.59% respectively as background harmonic voltage magnitudes. With respect to each harmonic order 0°, 120°, 240° and 300° phase angles were considered.

The harmonic currents observed at the PCC using the EMT models and Thevenin models for 5^{th}, 7^{th}, 11^{th}, 13^{th}, 29^{th} and 31^{st} harmonic orders are given in Figures 5.16, 5.17, 5.18, 5.19, 5.20 and 5.21 respectively. The sub-figures (a), (c), (e) and (g) show the current magnitudes at the PCC for 0°, 120°, 240° and 300° phase angles and sub-figures (b), (d), (f) and (h) illustrate the percentage error levels of the harmonic currents using results from EMT simulations as the reference levels.

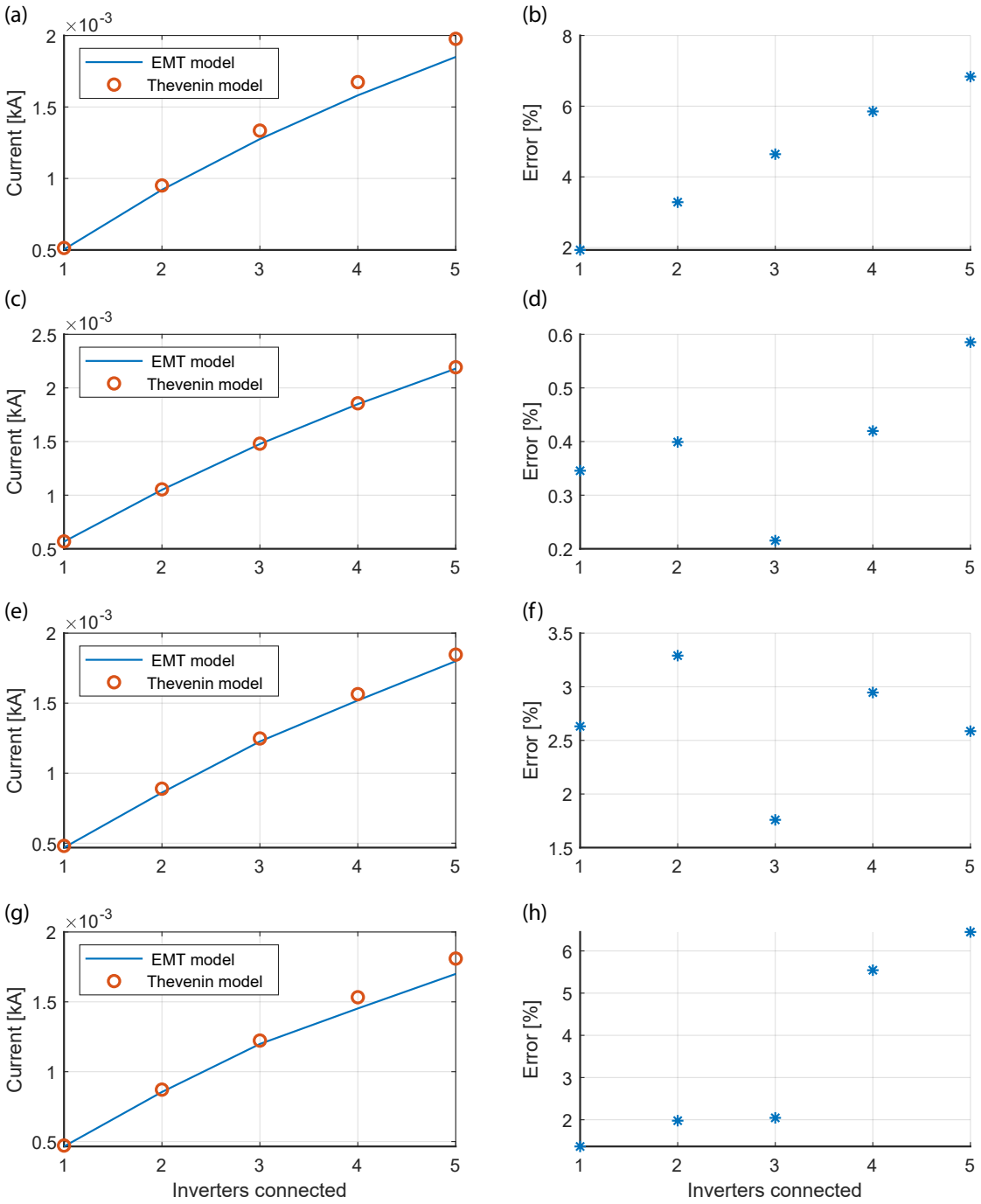

Figure 5.16: The variation of the 5th harmonic current at the PCC with 5th harmonic background voltage present in the grid

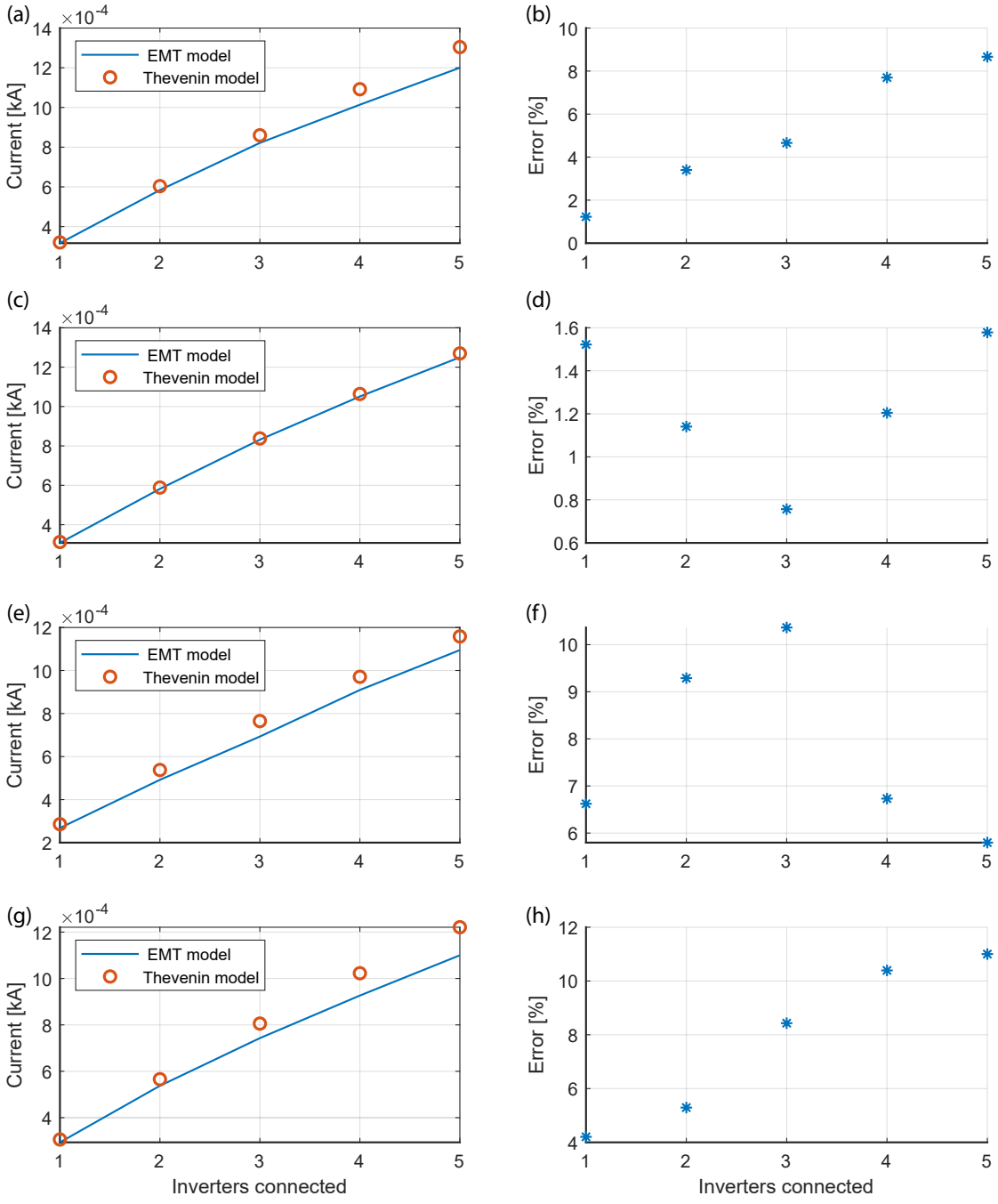

Figure 5.17: The variation of the 7th harmonic current at the PCC with 7th harmonic background voltage present in the grid

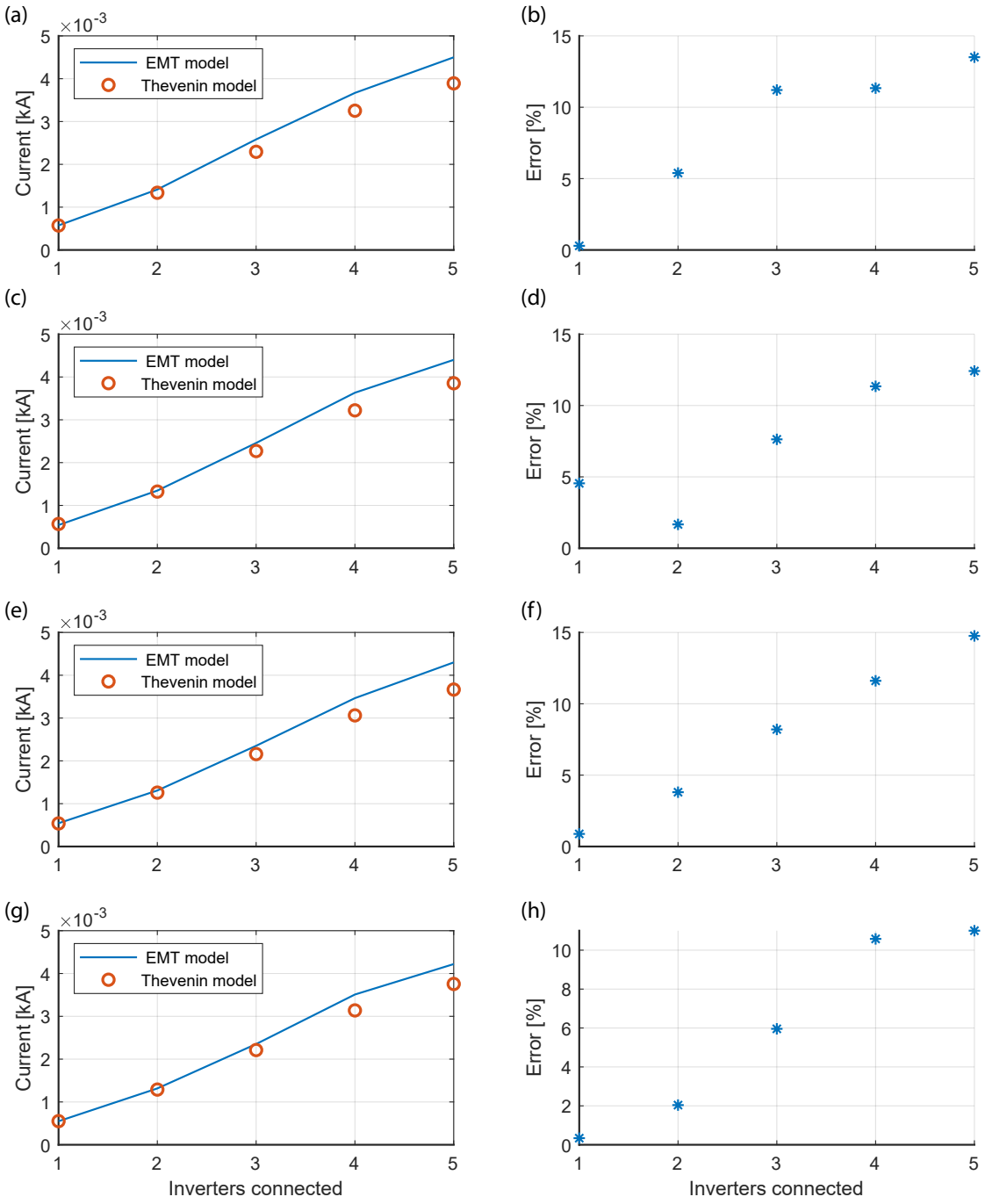

Figure 5.18: The variation of the 11th harmonic current at the PCC with 11th harmonic background voltage present in the grid

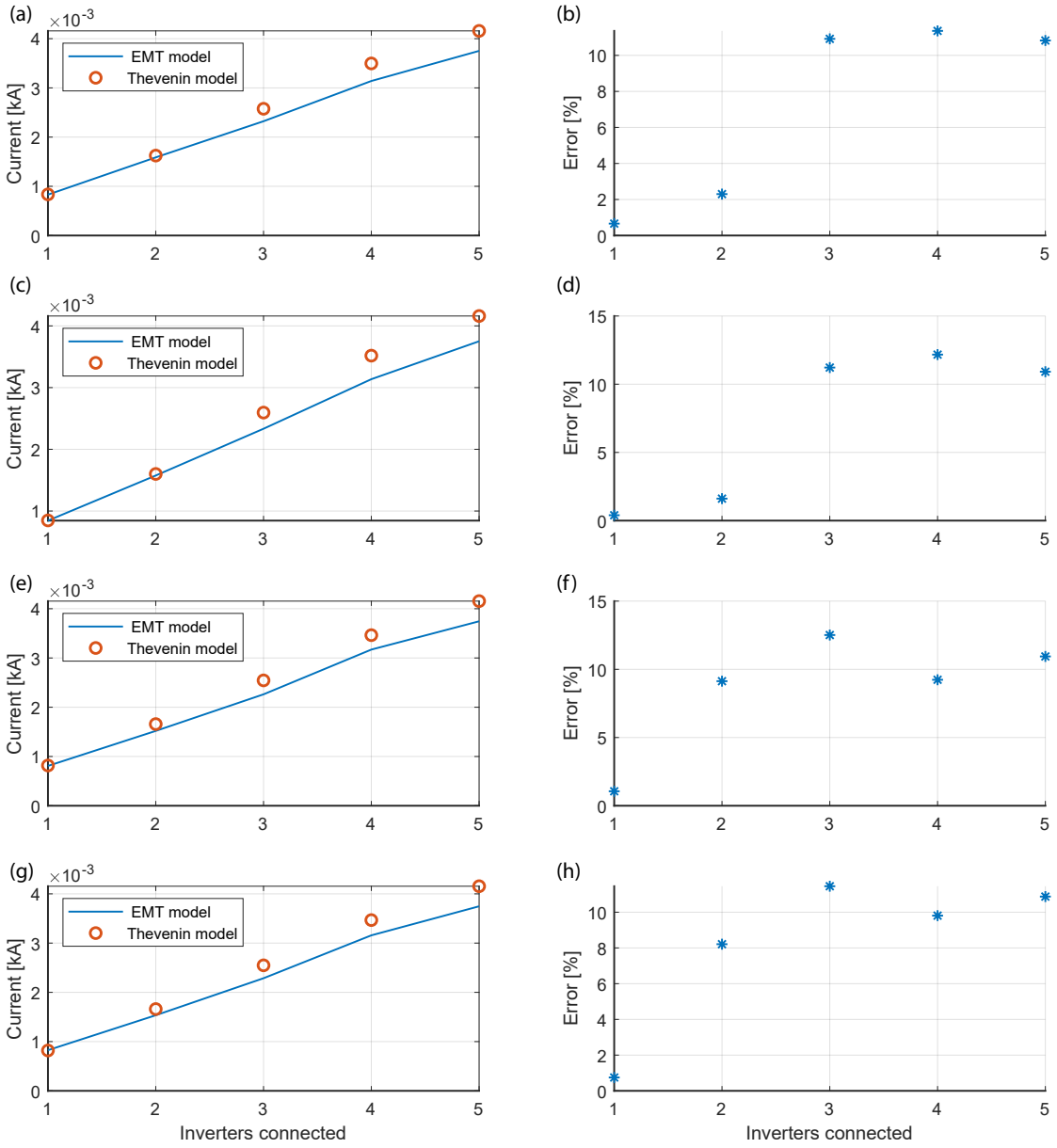

Figure 5.19: The variation of the 13th harmonic current at the PCC with 13th harmonic background voltage present in the grid

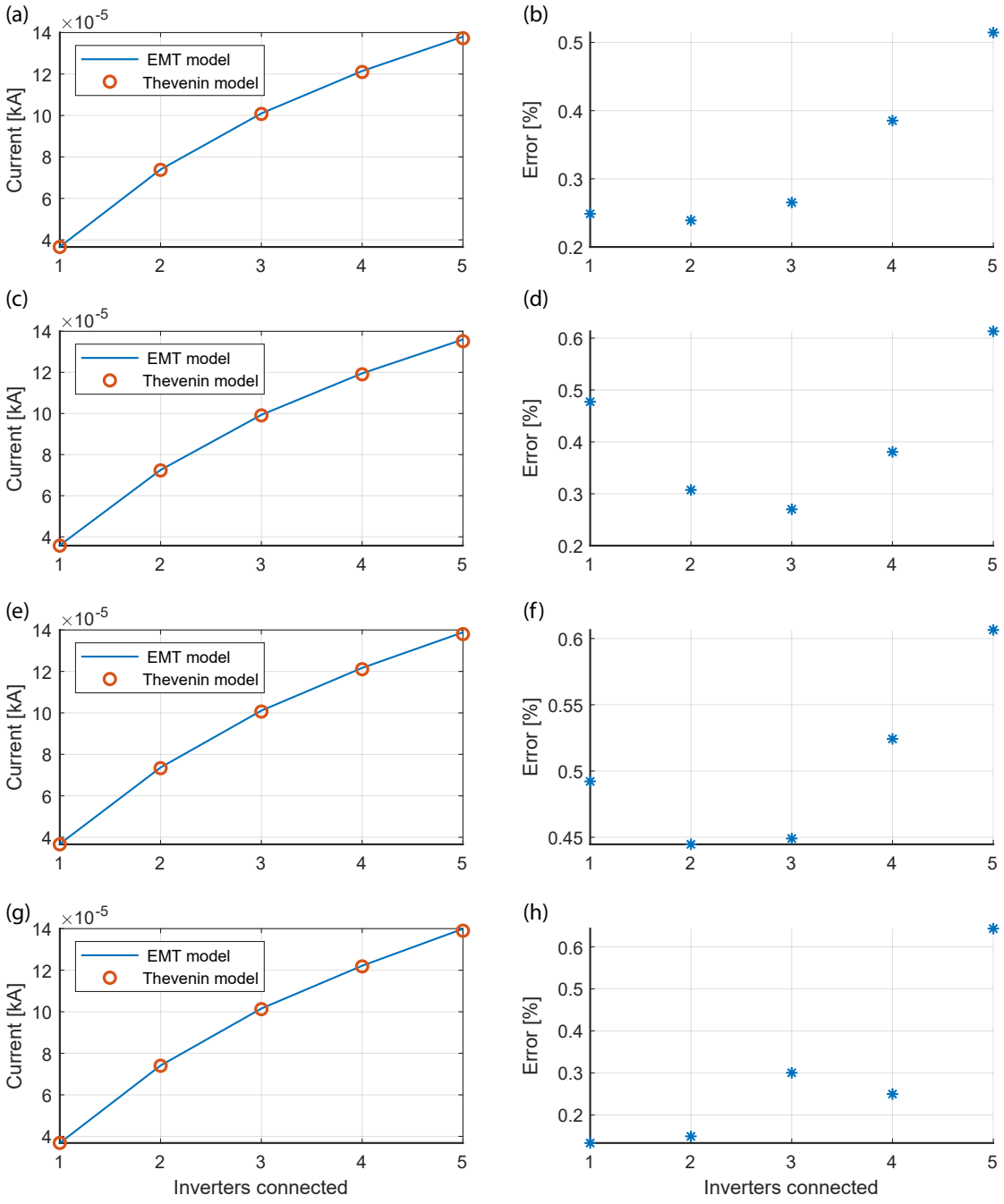

Figure 5.20: The variation of the 29th harmonic current at the PCC with 29th harmonic background voltage present in the grid

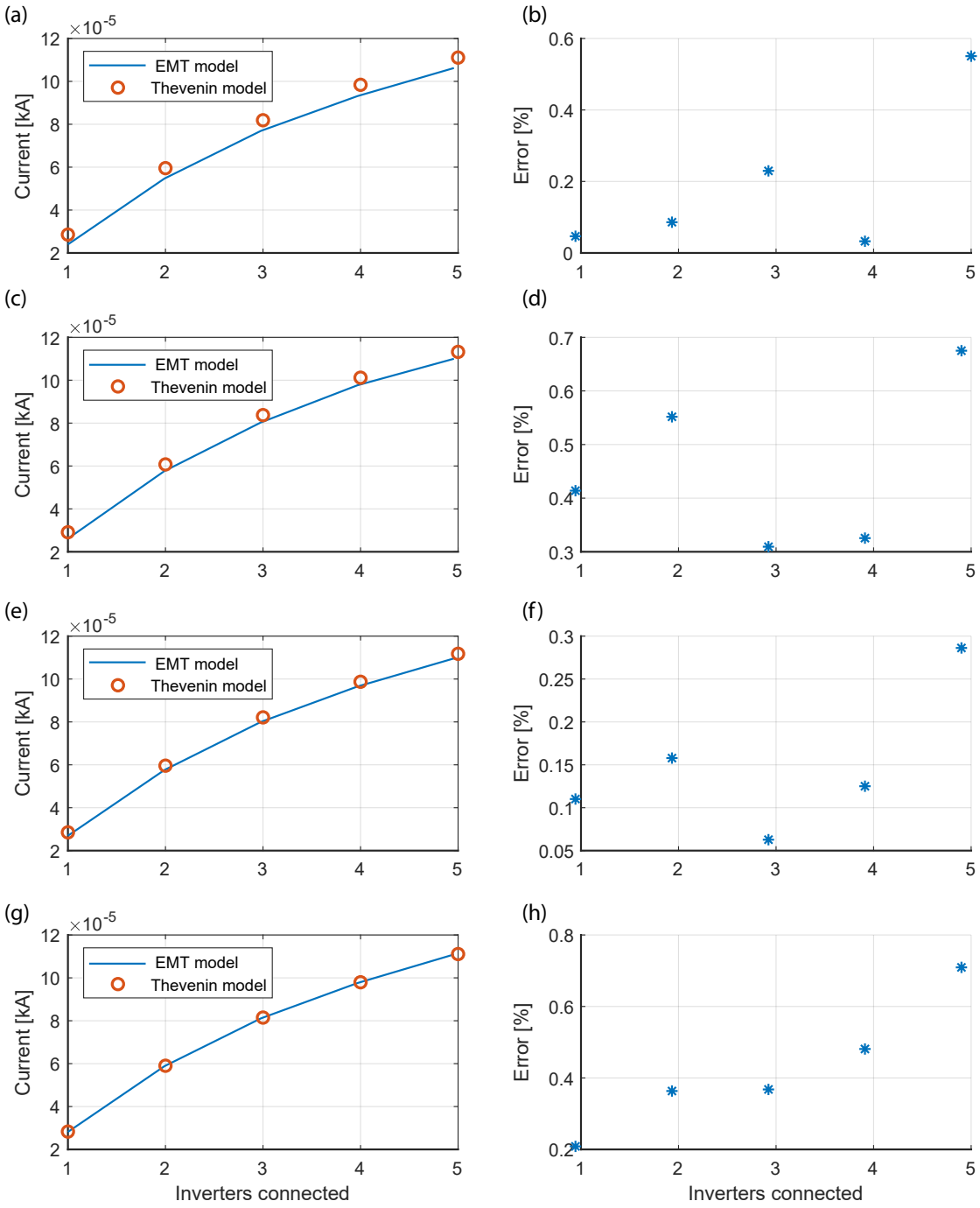

Figure 5.21: The variation of the 31st harmonic current at the PCC with 31st harmonic background voltage present in the grid

Analysis of the Results

Corresponding to the harmonic orders, 5th, 7th, 11th and 13th, the percentage error levels seem to increase with increasing number of inverters for most of the considered phase angles. It can also be observed that for each harmonic order, for certain phase angles, the percentage error levels are noted to exceed 6%. This dependency is most likely related to the relative phase angles of the corresponding harmonics arising from the inverter side

and the grid side, leading to additions or cancellations. Considering the maximum error percentages observed for each harmonic order as the worst case scenario, it can be concluded that the Thevenin models fail to predict the actual grid harmonic currents when the number of inverters connected to the grid increases in the presence of grid voltage harmonics, noting that only one harmonic at a time was considered to be present in the grid.

In relation to 29^{th} and 31^{st} harmonics, it is evident that the percentage error levels have an increasing trend when the number of connected inverters increases. However, the percentage error levels are significantly low compared to the other considered low-order harmonics. This observation tends to suggest that the use of Thevenin models of inverters may be adequate in the case of such relatively higher-order harmonics in place of EMT. However, noting the discrepancies observed with low order harmonics, such a conclusion may be somewhat premature to arrive at without further investigations.

5.7.2 Inverter Harmonic Model Performance With Balanced Multiple Background Harmonic Voltages

The analysis of the inverter performances will be quite complex when there are multiple background voltage harmonics present in the grid, mainly due to the cross-harmonic generation phenomenon. Even a single voltage harmonic present in the grid at a particular harmonic order can lead to current harmonics at the PCC both at the same harmonic order and at the cross harmonic order, an aspect that was not considered in Section 5.7.1. A summary of the coupling harmonics generated by three-phase grid-connected inverters due to the voltage harmonics injected from the grid is given in Table 5.10, where f_p, f_n and f_1 denote the positive sequence, negative sequence and fundamental frequency respectively.

Table 5.10: Coupled frequencies generated due to applied perturbation frequencies

Perturbation		Response	
Frequency	Sequence	Frequency	Sequence
f_p	Positive	f_p	Positive
		$f_p - 2f_1$	Negative
f_n	Negative	f_n	Negative
		$f_n + 2f_1$	Positive

While inverter EMT models can be expected to demonstrate cross harmonic generation phenomena, the frequency domain Norton models cannot be expected to demonstrate the same. Cross harmonic generation by inverters requires its own treatment as it is a complex phenomenon, where related preliminary studies will be covered in Chapter 7.

5.8 The Aggregated Current of the Solar Farm at the PCC

5.8.1 Introduction to Summation Law

The IEC Technical Report [26] covers a set of guidelines to keep harmonics emitted by installations under control. In this regard, when there are multiple harmonic sources connected to a PCC, the general summation law given in (5.5) is to be applied to determine the net harmonic level.

$$U_h = \sqrt[\alpha]{\sum_{i=1}^{N} U_{hi}^{\alpha}} \tag{5.5}$$

where, U_h is the total current/voltage of h^{th} harmonic order at the PCC; N is the number of harmonic sources connected to the PCC; U_{hi} is the h^{th} harmonic voltage/current generated by the i^{th} source. The recommended values of the summation exponent α are:

$$\alpha = \begin{cases} 1.0 & h < 5 \\ 1.4 & 5 \leq h \leq 10 \\ 2.0 & h > 10 \end{cases}$$

According to [74], [75], the application of standard summation exponents (α) to practical systems is disputable. Since a large solar farm is built-up by connecting identical inverters where there is little diversity between their harmonic behaviour, the total harmonic current at a particular order at the PCC can be argued to be the arithmetic sum of the individual harmonic currents. This hypothesis can be examined using the inverter EMT models considered in a solar farm environment. The inverter Norton/Thevenin models can also be used for comparison purposes in the same investigation.

5.8.2 Summation Laws Applied to the Solar Farm

In this study, the developed solar farm model was used to examine the applicability of the general summation law and the simple arithmetic summation to establish the net harmonic current at the PCC, with inverters operating at rated power. The Thevenin equivalent models were also used to determine the same. The harmonic current levels were observed by connecting one inverter at a time within the solar farm (with the associated cable network) until all five inverters were connected. The study covered 5^{th}, 7^{th}, 11^{th} and 13^{th} harmonics and the results are shown in Figure 5.22.

In summary, Figure 5.22 (a), (c), (e) and (g) illustrate the observations derived considering the 5^{th}, 7^{th}, 11^{th} and 13^{th} harmonics in relation to the following cases.

- EMT models of the individual inverter systems are added one by one in parallel,

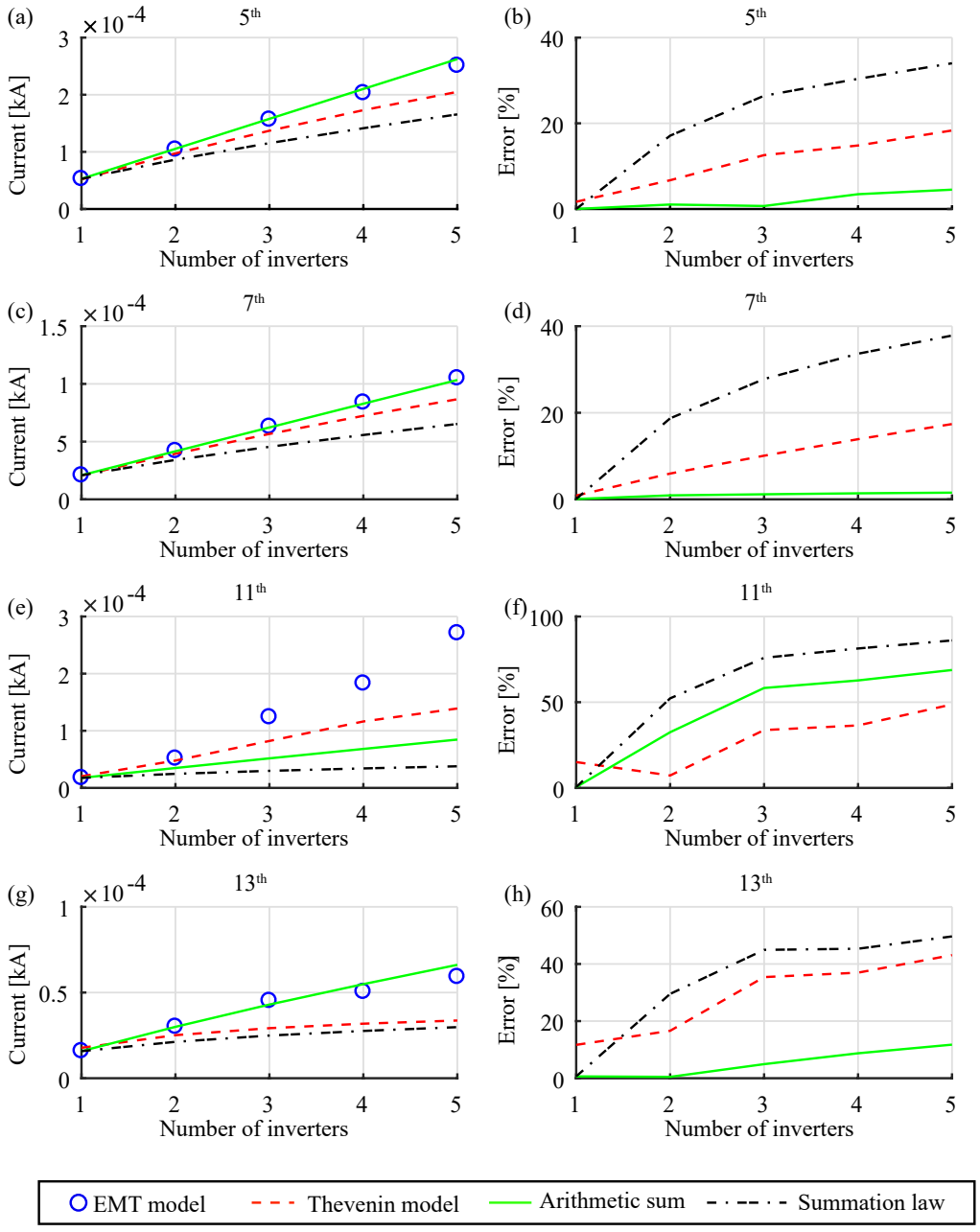

Figure 5.22: Summation results for the most significant harmonic orders

observing the harmonic current emission levels of the inverters at the PCC for each case. In Figure 5.22, these results have been labelled as 'EMT model'.

- EMT model of the individual inverter systems is considered one at a time, observing harmonic current emission levels of the inverter and that at the PCC with a view of determining the resultant harmonic current levels at the PCC using arithmetic summation (approach 1) and general summation law (approach 2)

- Thevenin models of all inverter systems considered at the same time observing the resultant harmonic current levels (approach 3)

Considering the case where the resultant harmonic current levels were determined solely using the EMT models as the reference (simulation results), the error levels associated with the other three approaches given above are shown in Figure 5.22 (b), (d), (f) and (h).

In addition to the low order harmonics considered above, studies were extended to cover higher-order 29th and 31st harmonics as well. These harmonic orders were chosen arbitrarily, where the study outcomes are shown in Figure 5.23.

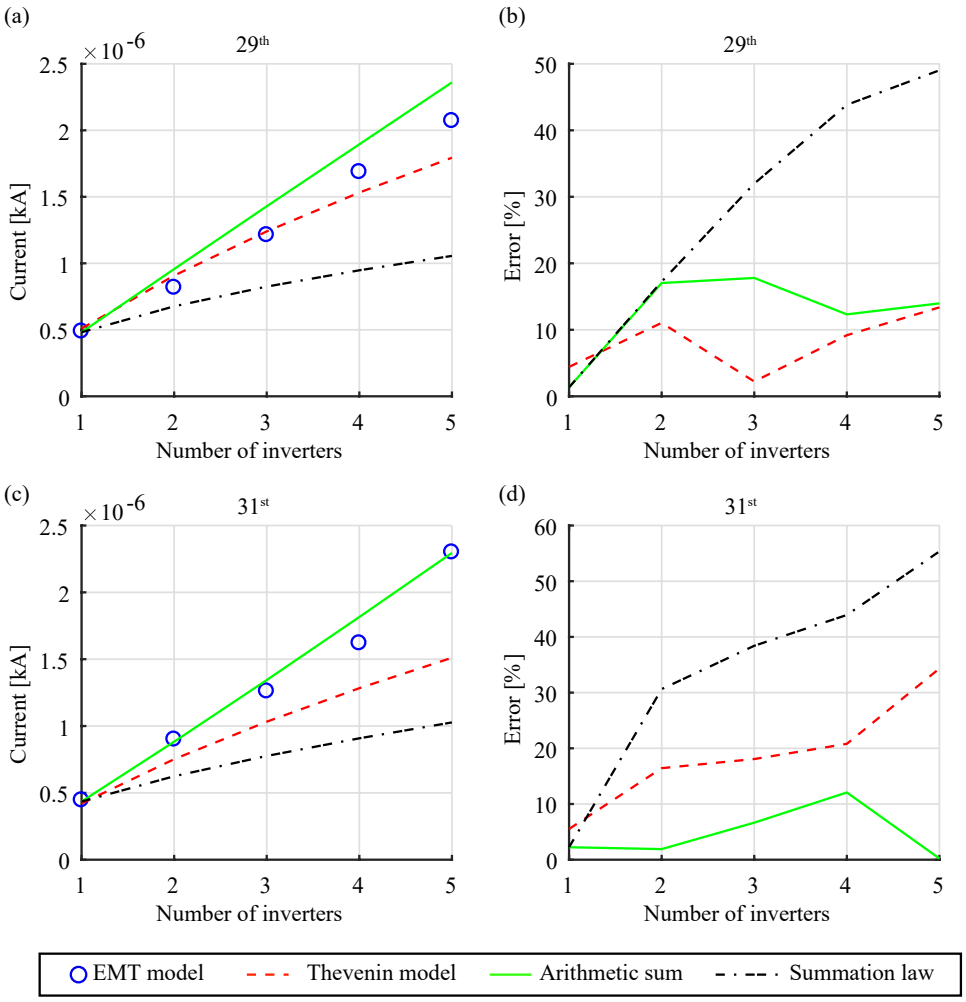

Figure 5.23: Thevenin equivalent model

5.8.3 Analysis of the Results

From the results illustrated in Figure 5.22, it is evident that except for the 11th harmonic, the other harmonic current levels at the PCC tend to agree with arithmetic summation of the individual harmonic currents as evident from acceptable error levels. The application of the general summation law has led to results which are significantly inferior even when compared with the results obtained using the Thevenin models.

With the 11^{th} harmonic, as the number of connected inverters grew from one to five employing the EMT models, it was noted that each new connection led to an approximately linear increase in the 11^{th} harmonic currents of all the already connected inverters to a new, nearly equal level, whereas this was not the case with regard to other harmonics considered. This individual inverter behaviour at the 11^{th} harmonic can be easily related to the collective trend illustrated by the resultant current at the PCC. This trend was also noted in the variation of the 11^{th} harmonic voltage at the PCC.

The distinct difference in the case of the 11^{th} harmonic requires detailed studies as it involves a multi-inverter scenario combined with the solar farm cable network and the supply system. In addition, there is also the possibility of some harmonic amplification leading to harmonic currents that exceed simple arithmetic summation. Considering these possibilities, a relatively simplistic study hypothesising possible resonance conditions was undertaken by carrying out impedance scans at the terminals of one inverter as the other inverters were added to the network one by one. It is, however, to be noted that such impedance scans require all active 11^{th} harmonic sources to be short-circuited in the network. This approximate study was conducted at one of the inverter output terminals with the cables associated with each inverter introduced one by one, but the corresponding inverters were removed while the supply network was connected. This scan represents any resonance conditions associated with the cable network. These impedance scans clearly demonstrated series resonance conditions at around the 11^{th} harmonic, thus supporting a corresponding increase in the 11^{th} harmonic current as the number of inverters connected was increased. As an example, Figure 5.24 gives the outcomes of the impedance scan at one inverter terminal considering the network containing the cable network of three inverters together with the supply system, which clearly shows the series resonance conditions at around 11^{th} harmonic.

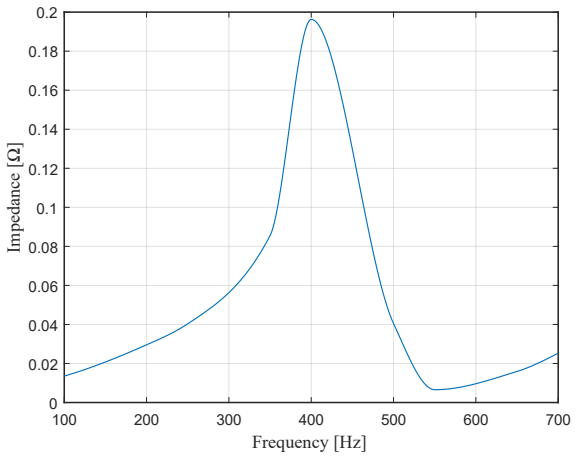

Figure 5.24: Thevenin equivalent model

5.8.4 Discussion

From the results in Figure 5.22 and Figure 5.23, it can be concluded that the arithmetic summation and the actual harmonic currents present at the PCC are in good agreement when the inverters are operating at the rated power level. Moreover, it is apparent from the results that more accurate results for the harmonic currents at the PCC can be achieved when the actual inverters are replaced by the corresponding Thevenin equivalent model, compared to the results calculated by standard summation law. Out of the three considered methods, the standard summation law results show the least agreement with the actual current at the PCC.

5.9 Chapter Summary

An inverter is a highly non-linear and complex power-electronic system where the harmonic currents generated can vary depending on the inverter internal and external operating conditions, such as operating power levels, grid voltage harmonics, and grid fault level. Although this is the practical scenario, the fixed Thevenin model parameters provided by the inverter vendors represent the worst case scenario of the harmonics injected. The exact methods used by the inverter manufacturers to determine these harmonic model parameters are not well known. In this chapter, the performance of the inverter Thevenin models under different inverter internal and external conditions in a solar farm environment was closely examined, comparing such outcomes with those obtained using EMT models.

At the very outset of the chapter, the Thevenin model parameter determination process was described. By employing these models, the harmonic currents injected by the inverters were investigated under different inverter internal and external conditions as the number of inverters increased in the considered solar farm, comparing the results with those obtained using corresponding EMT simulations. The studies were carried out under different conditions such as variable cable lengths, inverter reactive power injection/absorption levels, different grid fault levels, background voltage harmonics and the voltage unbalance conditions of the grid. For each study, the percentage error levels of the harmonic currents at the PCC when the inverter Thevenin models are used were calculated by taking the actual harmonic currents at the grid with the inverter EMT models as the reference case.

From the results, it was observed that for most of the cases, the percentage error levels increase with increasing the number of inverters connected in the solar farm model. This shows that the Thevenin models are less reliable in harmonic studies of large-scale solar farms. Furthermore, it was also observed that the inverter Thevenin impedances may interact with the rest of the network impedances leading to unexpected outcomes. These

observations show that, when performing the harmonic studies, Thevenin models may not give reliable results in many of the cases. Hence further analyses and/or more advanced processes need to be developed in harmonic studies to determine the harmonic compliance of solar farm models.

The aggregated harmonic currents at the PCC were determined employing arithmetic summation and the general summation laws, with the inverters operating at the rated power level. From this, it was concluded that the arithmetic summation is a suitable approach compared to the use of general summation law in determining the resultant harmonic current at the PCC of a solar farm.

Chapter 6

Analytical Derivation of Three Phase Inverter Harmonic Model Parameters

6.1 Introduction

As elaborated previously in Section 1.1, low order harmonics are more problematic compared to high order harmonics in relation to large scale inverters where their management at the connection points is crucial and hence pre-compliance harmonic studies take a prominent place. In such studies, it is quite common to use frequency domain models and Chapter 5 described how the parameters of these models can be determined using the harmonic injection method, whereas manufacturers tend to provide such models mainly based on measurements at test sites which have specific characteristics. Chapter 5 also examined how frequency domain models can lead to problematic outcomes, comparing the results of such studies with those derived using EMT models.

Noting that the Thevenin/Norton impedance of power electronic converters is known to depend on a range of factors, it is seen to be a significant step to examine how the equivalent impedance of a large scale inverter can be determined by employing a theoretical approach so that experimentally determined or the parameters established using the harmonic injection method can be validated. Some of the above influencing factors in relation to inverters are: the type of controllers used to regulate the inverter output current and hence the real and reactive power, the type of low-pass filter used at the inverter output terminals, the Phase Locked Loop (PLL) and the inverter modulation technique. Mathematical approaches for the determination of such impedances have become a topic of interest with regard to inverter/converter instability that can arise due to the interaction between the inverters and the grid installations [76]–[78].

This chapter presents a novel mathematical approach for the determination of inverter harmonic model parameters, where some of the principles are based on the existing work. The existing work consists of derivation of the output impedance of an inverter, which is

connected to a constant dc link voltage and a simple L filter which operates in d-q reference frame [76]–[78]. In this chapter, the procedure which was followed to derive the mathematical expressions for the output impedance of two types of three phase inverter configurations is given, assuming the inverters are connected to a pure dc link voltage. The method used to determine the Norton model parameters, including the Norton source current is given using the derived inverter output impedances. The process has been extended for a three-phase grid-connected inverter, considering the dc link dynamics as well.

Out of the inverter configurations used in this chapter, the first and the second inverter configurations are connected to a pure dc link, controlled in $\alpha - \beta$ reference frame and d-q reference frames respectively. The configuration of the three-phase inverter controlled in the d-q reference frame is vastly different from the configuration of the three-phase inverter controlled in the α-β reference frame. These two configurations are considered to illustrate the fact that mathematical modelling is not limited to a particular configuration. The third inverter configuration consists of both ac and dc networks and hence, mathematical expressions are derived for the inverter output harmonic impedance, taking into account the ac and dc network dynamics. Following the determination of inverter output impedance, the Norton model harmonic currents are determined using only one set of inverter output voltage and current measurements. For selected harmonic orders, the theoretical model outcomes are compared with simulation outcomes.

6.2 Development of Mathematical Expressions for Inverter Output Impedance Assuming Constant Inverter DC Link Voltage

6.2.1 Grid-connected Three-phase Inverter in the α-β Reference Frame

A grid-connected three-phase inverter with an LCL low pass filter controlled in the $\alpha - \beta$ reference frame is first modelled. Although LCL low pass filters are commonly used

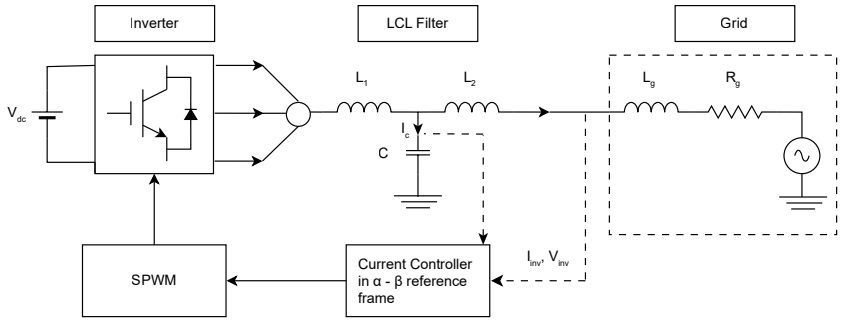

Figure 6.1: Three-phase inverter controlled in alpha-beta reference frame

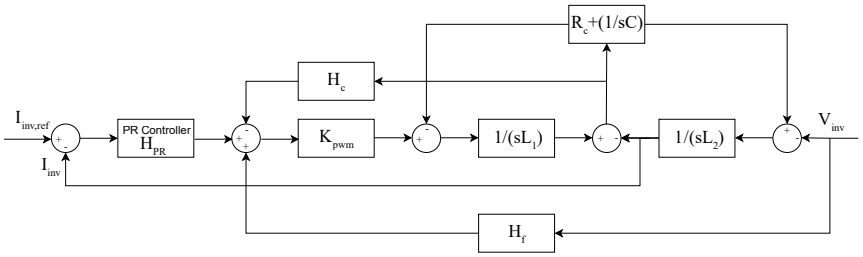

Figure 6.2: The schematic diagram showing the three-phase inverter operation

to attenuate high order harmonics at the inverter output, they may lead to resonances. The capacitor-current feedback active damping method is used when modelling the three-phase grid-connected inverter in this study to mitigate this issue [79]. The SPWM technique is used to generate the switching pulses of the inverter. Furthermore, the dc voltage of the inverter is assumed to be constant. A PR controller is used to control the grid current of the inverter.

The schematic diagram of the modelled grid-connected inverter is shown in Figure 6.1. The inverter and its control system can be represented using the block diagram shown in Figure 6.2. The components L_1, L_2 and C are the inverter side inductance, grid side inductance and the capacitance of the LCL filter respectively. Inverter gain is denoted by K_{pwm}. H_{f}, H_{c} and H_{PR} are the grid voltage feed-forward gain, capacitor current feedback gain and the transfer function of the PR current controller respectively.

Using the details in Figure 6.2, an expression for the inverter output impedance can be derived as given in (6.1).

$$Z_{\text{inv}}(s) = \frac{L_1L_2Cs^3 + K_{\text{pwm}}H_{\text{c}}L_2Cs^2 + (L_1+L_2)s + K_{\text{pwm}}H_{PR}}{L_1Cs^2 + K_{\text{pwm}}(H_{\text{c}}Cs - H_{\text{f}}) + 1} \tag{6.1}$$

Using (6.1), the inverter output impedances at different frequencies can be determined. This however is used only when the inverter operates at its rated power level as the inverter active power controller has not been taken into consideration when developing the mathematical expressions.

6.2.2 Grid-connected Three-phase Inverter in the d-q Reference Frame

In this section, a mathematical expression for the output impedance of a grid-connected three-phase inverter controlled in the d-q reference frame is developed, and following this, both positive and negative sequence impedances are established. Since the inverter dc link voltage is assumed to be constant, the small-signal behaviour of the inverter that can be observed at its ac terminals can be described by the admittance matrix given in (6.2).

$$\begin{pmatrix} \bar{I}_p \\ \bar{I}_n \end{pmatrix} = \begin{pmatrix} Y_{pp} & Y_{pn} \\ Y_{np} & Y_{nn} \end{pmatrix} \begin{pmatrix} \bar{V}_p \\ \bar{V}_n \end{pmatrix} \tag{6.2}$$

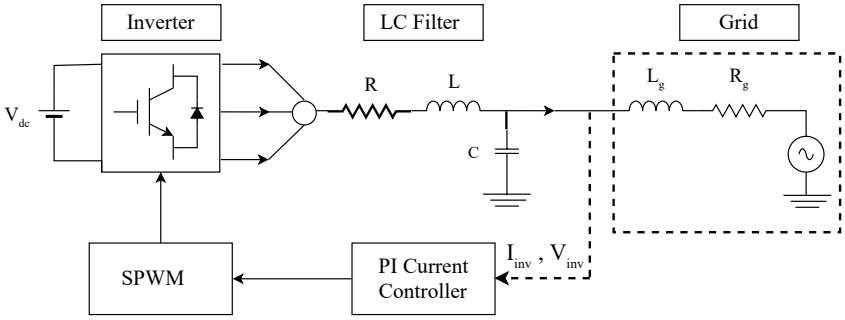

Figure 6.3: Three-phase inverter controlled in d-q reference frame

where, $\bar{I_p}$, $\bar{I_n}$, $\bar{V_p}$ and $\bar{V_n}$ denote the small signal notations of positive sequence current, negative sequence current, positive sequence voltage and negative sequence voltage respectively. Y_{pp}, Y_{nn} are positive and negative sequence inverter output impedances, respectively. In this section, the coupling between the negative and positive sequence dynamics is ignored for simplicity.

A schematic diagram of the grid-connected three-phase inverter is shown in Figure 6.3 which is modelled in the d-q reference frame. The SPWM technique is used as the switching technique of the inverter and its grid current is controlled using PI controllers with grid voltage feed-forward. Noting their widespread use in industry level three-phase inverters, an LC filter is used in the work undertaken. The inverter dc bus voltage is assumed to be constant.

The derivations of the mathematical expressions for the inverter output impedance with and without considering the Phase Locked Loop (PLL) dynamics are described below:

Without Considering the PLL Dynamics

Based on the schematic diagram shown in Figure 6.3, the relationship between the inverter output current (I_{inv}) and the voltage (V_{inv}) can be shown using (6.3).

$$K_{\mathrm{m}}V_{\mathrm{dc}}m_{\mathrm{a}} = (Ls+R)I_{\mathrm{inv}} + (LCs^2+RCs+1)V_{\mathrm{inv}} \tag{6.3}$$

where, L, R, C are LC filter inductance, parasitic resistance, LC filter capacitance respectively. $K_{\mathrm{m}}, V_{\mathrm{dc}}, m_{\mathrm{a}}$ are inverter gain, dc link voltage and modulating signal respectively. Furthermore, I_{inv} and V_{inv} are inverter output current and voltage respectively.

For the purpose of deriving the inverter output impedance, two small positive and negative sequence voltage signals are injected from the grid side. Thus, the inverter phase voltage on the grid side can be expressed in the time domain as,

$$V_{\mathrm{inv}}(t) = V_1\cos(2\pi f_1 t) + V_{\mathrm{p}}\cos(2\pi f_{\mathrm{p}} t + \theta_{\mathrm{p}}) + V_{\mathrm{n}}\cos(2\pi f_{\mathrm{n}} t + \theta_{\mathrm{n}}) \tag{6.4}$$

where, V_1, V_{p} and V_{n} are fundamental voltage, positive and negative sequence voltage magnitudes respectively. f_1, f_{p} and f_{n} are fundamental, positive sequence and negative

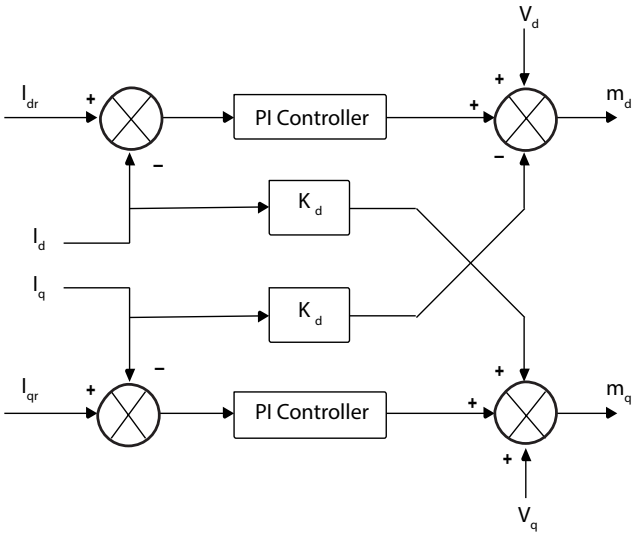

Figure 6.4: Current controller in d-q reference frame

sequence frequencies, and θ_{p} and θ_{n} are positive and negative sequence voltage phase angles respectively. The inverter current in the same phase resulting from the resultant applied voltage can be written as,

$$I_{\mathrm{inv}}(t) = I_1 \cos(2\pi f_1 t + \theta_{\mathrm{i1}}) + I_p \cos(2\pi f_{\mathrm{p}} t + \theta_{\mathrm{ip}}) + I_{\mathrm{n}} \cos(2\pi f_{\mathrm{n}} t + \theta_{\mathrm{in}}) \tag{6.5}$$

where, I_1, I_p and I_{n} are fundamental, positive and negative sequence current magnitudes respectively. θ_{i1} is the phase angle of the fundamental current. θ_{ip} and θ_{in} are the phase angles of positive and negative sequence currents respectively.

Hence, the voltage and current on the grid side in the frequency domain can be given as,

$$V_a(f) = \begin{cases} \bar{V_1}, & f = \pm f_1 \\ \bar{V_{\mathrm{p}}}, & f = \pm f_{\mathrm{p}} \\ \bar{V_{\mathrm{n}}}, & f = \pm f_{\mathrm{n}} \end{cases} \tag{6.6}$$

$$I_a(f) = \begin{cases} \bar{I_1}, & f = \pm f_1 \\ \bar{I_p}, & f = \pm f_{\mathrm{p}} \\ \bar{I_{\mathrm{n}}}, & f = \pm f_{\mathrm{n}} \end{cases} \tag{6.7}$$

where, $\bar{V_{\mathrm{p}}} = (\frac{V_{\mathrm{p}}}{2}) \exp(\pm j\theta_{\mathrm{p}})$ and all associated voltages and currents ($\bar{V_1}$, $\bar{V_{\mathrm{n}}}$, $\bar{I_1}$, $\bar{I_{\mathrm{n}}}$ and $\bar{I_{\mathrm{p}}}$) in this section have notations similar to that of $\bar{V_{\mathrm{p}}}$.

Since the dynamics of the PLL are not considered in this section and assuming the PLL angle to be given by $\theta_{\mathrm{PLL}} = 2\pi f_1 t$, the d-q components of the current at the inverter output

can be given as,

$$I_d(f) = \begin{cases} I_1 \cos\theta_{\mathrm{i1}}, & f = dc \\ \bar{I}_p, & f = \pm(f_\mathrm{p} - f_1) \\ \bar{I}_\mathrm{n}, & f = \pm(f_\mathrm{n} + f_1) \end{cases} \tag{6.8}$$

$$I_q(f) = \begin{cases} I_1 \sin\theta_{\mathrm{i1}}, & f = dc \\ \mp j\bar{I}_p, & f = \pm(f_\mathrm{p} - f_1) \\ \pm j\bar{I}_\mathrm{n}, & f = \pm(f_\mathrm{n} + f_1) \end{cases} \tag{6.9}$$

The d and q components of the inverter output voltage can also be derived in a similar manner as given in (6.10) and (6.11).

$$V_d(f) = \begin{cases} V_1, & f = dc \\ \bar{V}_p, & f = \pm(f_\mathrm{p} - f_1) \\ \bar{V}_\mathrm{n}, & f = \pm(f_\mathrm{n} + f_1) \end{cases} \tag{6.10}$$

$$V_q(f) = \begin{cases} \mp j\bar{V}_p, & f = \pm(f_\mathrm{p} - f_1) \\ \pm j\bar{V}_\mathrm{n}, & f = \pm(f_\mathrm{n} + f_1) \end{cases} \tag{6.11}$$

The expressions for the modulation signals in the d-q reference frame can be derived using the schematic diagram of the inverter current controller shown in Figure 6.4, according to which m_d and m_q are the d and q components of the modulating signal which can be derived as,

$$\begin{aligned} m_\mathrm{d} &= (I_\mathrm{dr} - I_\mathrm{d})H(s) - I_\mathrm{q}K_\mathrm{d} + K_\mathrm{f}V_\mathrm{d} \\ m_\mathrm{q} &= (I_\mathrm{qr} - I_\mathrm{q})H(s) + I_\mathrm{d}K_\mathrm{d} + K_\mathrm{f}V_\mathrm{q} \end{aligned} \tag{6.12}$$

where, H(s) and K_d denote the PI current controller transfer function and the decoupling gain of the current controller respectively. The effect of grid voltage feed-forward has been taken into consideration in deriving the inverter output impedance where K_f denotes the grid voltage feed-forward gain. I_dr and I_qr are the d and q axis reference currents respectively.

Using equations (6.8), (6.9), (6.10), (6.11) and (6.12), an expression for the modulation signal in the time domain can be derived and by substituting it in (6.3), the positive and negative sequence inverter output impedances can be derived as,

$$Z_{\mathrm{p}} = \frac{-V_p}{I_{\mathrm{p}}} = \frac{Ls + R + K_{\mathrm{m}}V_{\mathrm{dc}}H(s - j2\pi f_1) - jK_{\mathrm{d}}K_{\mathrm{m}}V_{\mathrm{dc}}}{LCs^2 + RCs + 1 - K_{\mathrm{m}}V_{\mathrm{dc}}K_{\mathrm{f}}}$$
$$Z_{\mathrm{n}} = \frac{-V_{\mathrm{n}}}{I_{\mathrm{n}}} = \frac{Ls + R + K_{\mathrm{m}}V_{\mathrm{dc}}H(s + j2\pi f_1) + jK_{\mathrm{d}}K_{\mathrm{m}}V_{\mathrm{dc}}}{LCs^2 + RCs + 1 - K_{\mathrm{m}}V_{\mathrm{dc}}K_{\mathrm{f}}} \tag{6.13}$$

Derivation of Inverter Output Impedance Incorporating the PLL Dynamics

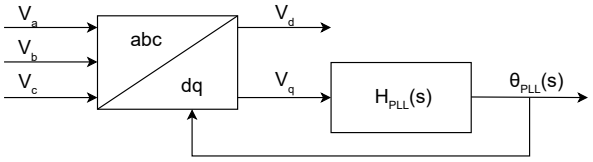

Figure 6.5: Block diagram for a basic PLL

Figure 6.5 shows the basic configuration of a PLL, which consists of a Park transformation block and a loop compensator which has a transfer function of H_{PLL}. When a voltage perturbation signal is injected from the grid side, the PLL response can be written as,

$$\theta_{\mathrm{PLL}} = \theta_1 + \Delta\theta \tag{6.14}$$

where, θ_{PLL} is the PLL output angle, θ_1 is the fundamental PLL output angle in the absence of the perturbation signal and $\Delta\theta$ is the angle difference caused by the voltage perturbation injection on the grid side.

As a consequence of the change in PLL output angle, the Park transformation needs some modifications as shown in (6.15).

$$P(\theta_{\mathrm{PLL}}) = \begin{pmatrix} \cos(\Delta\theta) & \sin(\Delta\theta) & 0 \\ -\sin(\Delta\theta) & \cos(\Delta\theta) & 0 \\ 0 & 0 & 1 \end{pmatrix} P(\theta_1) \tag{6.15}$$

where, $P(\theta_{\mathrm{PLL}})$ denotes the Park transformation, if the PLL response is θ_{PLL}. And, $P(\theta_1)$ is the park transformation when there is not any perturbation present from the grid side.

Due to the voltage perturbation injection and as a result of the deviation of the PLL angle by $\Delta\theta$, the expressions derived for I_d, I_q, V_d and V_q shown in (6.8), (6.9), (6.10) and (6.11) in frequency domain require some modifications. If the modified current and voltage parameters in the frequency domain are represented by $I_{d,mod}$, $I_{q,mod}$, $V_{d,mod}$ and $V_{q,mod}$ respectively, using (6.10), (6.11), (6.15) and considering small signal modelling, expressions for $V_{\mathrm{q,mod}}$ and $V_{\mathrm{d,mod}}$ in time domain can be derived as,

$$V_{\mathrm{q,mod}}(t) \approx -\Delta\theta(t)V_{\mathrm{d}}(t) + V_{\mathrm{q}}(t)$$
$$V_{\mathrm{d,mod}}(t) \approx \Delta\theta(t)V_{\mathrm{q}}(t) + V_{\mathrm{d}}(t) \tag{6.16}$$

Assuming the deviation of the PLL angle ($\Delta\theta$) to be proportional to the applied disturbance voltage, expressions for $\Delta\theta$ in both positive and negative sequences can be written as,

$$\Delta\theta(s) = \begin{cases} H_{\mathrm{p}}(s)\bar{V}_{\mathrm{p}}, & f = \pm(f_{\mathrm{p}} - f_1) \\ H_{\mathrm{n}}(s)\bar{V}_{\mathrm{n}}, & f = \pm(f_{\mathrm{n}} + f_1) \end{cases} \tag{6.17}$$

where, H_{p} and H_{n} are proportional transfer functions in the positive and negative sequences respectively.

Using the equations (6.10), (6.11), (6.16) and (6.17) expressions for the $V_{\mathrm{q,mod}}$ and $V_{\mathrm{d,mod}}$ in positive and negative sequences can be derived as shown in (6.18) and (6.19).

$$V_{\mathrm{q,mod}}(s) = \begin{cases} [-H_{\mathrm{p}}(s)V_1 \mp j]\bar{V}_{\mathrm{p}}, & f = \pm(f_{\mathrm{p}} - f_1) \\ [-H_{\mathrm{n}}(s)V_1 \pm j]\bar{V}_{\mathrm{n}}, & f = \pm(f_{\mathrm{n}} + f_1) \end{cases} \tag{6.18}$$

$$V_{\mathrm{d,mod}}(s) = \begin{cases} [(\mp j)H_{\mathrm{p}}(s)V_1 + 1]\bar{V}_{\mathrm{p}}, & f = \pm(f_{\mathrm{p}} - f_1) \\ [(\pm j)H_{\mathrm{n}}(s)V_1 + 1]\bar{V}_{\mathrm{n}}, & f = \pm(f_{\mathrm{n}} + f_1) \end{cases} \tag{6.19}$$

According to Figure 6.5, $\theta_{\mathrm{PLL}} = H_{\mathrm{PLL}}V_q$. Therefore, expressions for $H_{\mathrm{p}}(s)$ and $H_{\mathrm{n}}(s)$ can be derived as given in (6.20).

$$\begin{aligned} H_{\mathrm{p}}(s) &= [\mp jH_{\mathrm{PLL}}(s)]/[1 + V_1H_{\mathrm{PLL}}(s)] \\ H_{\mathrm{n}}(s) &= [\pm jH_{\mathrm{PLL}}(s)]/[1 + V_1H_{\mathrm{PLL}}(s)] \end{aligned} \tag{6.20}$$

From (6.15), (6.18) and (6.20) expressions for $\cos(\theta_{\mathrm{PLL}})$ and $\sin(\theta_{\mathrm{PLL}})$ for positive and negative perturbations can be derived as given in (6.21) and (6.22).

$$\cos(\theta_{\mathrm{PLL}})(s) = \begin{cases} \dfrac{H_{\mathrm{PLL}}(s - j2\pi f_1)V_{\mathrm{p}}}{2[1 + V_1H_{\mathrm{PLL}}(s - j2\pi f_1)]}, & f = \pm(f_{\mathrm{p}} - f_1) \\ \dfrac{H_{\mathrm{PLL}}(s + j2\pi f_1)V_{\mathrm{p}}}{2[1 + V_1H_{\mathrm{PLL}}(s + j2\pi f_1)]}, & f = \pm(f_{\mathrm{n}} + f_1) \end{cases} \tag{6.21}$$

$$\sin(\theta_{\mathrm{PLL}})(s) = \begin{cases} \dfrac{\mp jH_{\mathrm{PLL}}(s - j2\pi f_1)V_{\mathrm{p}}}{2[1 + V_1H_{\mathrm{PLL}}(s - j2\pi f_1)]}, & f = \pm(f_{\mathrm{p}} - f_1) \\ \dfrac{\pm jH_{\mathrm{PLL}}(s + j2\pi f_1)V_{\mathrm{p}}}{2[1 + V_1H_{\mathrm{PLL}}(s + j2\pi f_1)]}, & f = \pm(f_{\mathrm{n}} + f_1) \end{cases} \tag{6.22}$$

From (6.21) and (6.22), it is evident that due to the applied small signal voltage components, the Park transformation is affected resulting from the angle variation that is reflected in the PLL response. Hence, the inverter output current in the d-q reference frame ($I_{d,mod}(f)$ and $I_{q,mod}(f)$) can be given using the expressions given in (6.23) and (6.24).

$$I_{d,mod}(s) = \begin{cases} I_1 \cos\theta_{i1}, & f = dc \\ \bar{I_p} + I_1 \sin\theta_{i1} H_{\mathrm{PLL}}(s) \bar{V}_{\mathrm{p}}, & f = \pm(f_{\mathrm{p}} - f_1) \\ \bar{I}_{\mathrm{n}} - I_1 \sin\theta_{i1} H_{\mathrm{PLL}}(s) \bar{V}_{\mathrm{n}}, & f = \pm(f_{\mathrm{n}} + f_1) \end{cases} \tag{6.23}$$

$$I_{q,mod}(s) = \begin{cases} I_1 \sin\theta_{i1}, & f = dc \\ \mp j\bar{I_p} - I_1 \cos\theta_{i1} H_{\mathrm{PLL}}(s) \bar{V}_{\mathrm{p}}, & f = \pm(f_{\mathrm{p}} - f_1) \\ \pm j\bar{I}_{\mathrm{n}} + I_1 \cos\theta_{i1} H_{\mathrm{PLL}}(s) \bar{V}_{\mathrm{n}}, & f = \pm(f_{\mathrm{n}} + f_1) \end{cases} \tag{6.24}$$

From (6.18), (6.19) and (6.20), expressions for $V_{\mathrm{q,mod}}$ and $V_{\mathrm{d,mod}}$ can be derived as shown in (6.25) and (6.26).

$$V_{\mathrm{q,mod}}(s) = \begin{cases} \dfrac{\mp j\bar{V}_{\mathrm{p}}}{1 + V_1 H_{PLL}}, & f = \pm(f_{\mathrm{p}} - f_1) \\ \\ \dfrac{\pm j\bar{V}_{\mathrm{n}}}{1 + V_1 H_{PLL}}, & f = \pm(f_{\mathrm{n}} + f_1) \end{cases} \tag{6.25}$$

$$V_{\mathrm{d,mod}}(s) = \begin{cases} \dfrac{\bar{V}_{\mathrm{p}}}{1 + V_1 H_{PLL}}, & f = \pm(f_{\mathrm{p}} - f_1) \\ \\ \dfrac{\bar{V}_{\mathrm{n}}}{1 + V_1 H_{PLL}}, & f = \pm(f_{\mathrm{n}} + f_1) \end{cases} \tag{6.26}$$

The expressions for the modulation signals in the d-q reference frame can be derived using the schematic diagram of the inverter current controller shown in Figure 6.4 according to which new modulation signals in the d-q reference frame given by $m_{\mathrm{d,mod}}$ and $m_{\mathrm{q,mod}}$ can be derived as;

$$\begin{aligned} m_{\mathrm{d,mod}} &= (I_{\mathrm{dr}} - I_{\mathrm{d,mod}})H(s) - I_{\mathrm{q,mod}} K_{\mathrm{d}} + K_{\mathrm{f}} V_{\mathrm{d,mod}} \\ m_{\mathrm{q,mod}} &= (I_{\mathrm{qr}} - I_{\mathrm{q,mod}})H(s) + I_{\mathrm{d,mod}} K_{\mathrm{d}} + K_{\mathrm{f}} V_{\mathrm{q,mod}} \end{aligned} \tag{6.27}$$

where, H(s) and K_{d} denote the PI current controller transfer function and the decoupling gain of the current controller respectively. The effect of grid voltage feed forward has been taken into consideration in deriving the inverter output impedance where K_{f} denotes the grid voltage feed forward gain. I_{dr} and I_{qr} are the d and q axis reference currents respectively. Hence, the inverter output impedance in the frequency domain can be established using equations (6.3), (6.23), (6.24) and (6.27). The derived expressions for the inverter output impedance in the positive and negative sequence domain are given in (6.28).

$$Z_{\mathrm{p}}(s) = \frac{Ls + R + K_{\mathrm{m}}V_{\mathrm{dc}}H(s - j2\pi f_1) - jK_{\mathrm{d}}K_{\mathrm{m}}V_{\mathrm{dc}})}{LCs^2 + RCs + 1 - K_{\mathrm{m}}V_{\mathrm{dc}}K_{\mathrm{f}} - (M + H(s - j2\pi f_1)\frac{I_1 e^{j\phi_1}}{2} - \frac{jK_{\mathrm{d}}I_1 e^{j\phi_1}}{2}T_{\mathrm{PLL}}\frac{K_{\mathrm{m}}V_{\mathrm{d}}}{V_1})}$$

$$Z_{\mathrm{n}}(s) = \frac{Ls + R + K_{\mathrm{m}}V_{\mathrm{dc}}H(s + j2\pi f_1) + jK_{\mathrm{d}}K_{\mathrm{m}}V_{\mathrm{dc}})}{LCs^2 + RCs + 1 - K_{\mathrm{m}}V_{\mathrm{dc}}K_{\mathrm{f}} - (M + H(s + j2\pi f_1)\frac{I_1 e^{-j\phi_1}}{2} - \frac{jK_{\mathrm{d}}I_1 e^{-j\phi_1}}{2}T_{\mathrm{PLL}}\frac{K_{\mathrm{m}}V_{\mathrm{d}}}{V_1})} \tag{6.28}$$

where;

$$\begin{aligned} M &= \frac{V_1 + j\omega_1 L I_1 e^{j\phi_1} - K_{\mathrm{m}}V_{\mathrm{dc}}K_{\mathrm{f}}V_1}{K_{\mathrm{m}}V_{\mathrm{dc}}} \\ T_{\mathrm{PLL}}(s) &= \frac{V_1 H_{\mathrm{PLL}}(s)}{1 + V_1 H_{\mathrm{PLL}}(s)} \end{aligned} \tag{6.29}$$

6.2.3 Inverter Harmonic Model Parameter Determination

It has been conventional that inverters are usually represented as Norton models, and the connected grid is represented as a Thevenin model. Using these conventions, the grid-connected inverter system can be represented using Figure 6.6, in which, $Y_g(s)$ and $V_g(s)$ represent the grid impedance and grid voltage, respectively. If the output admittance ($Y_{\mathrm{s}}(s)$) is known, the inverter Norton model source current can be determined using (6.30).

$$I_{\mathrm{s}}(s) = I_{\mathrm{inv}}(s) + V_{\mathrm{inv}}(s)Y_{\mathrm{s}}(s) \tag{6.30}$$

where, I_{inv}, V_{inv}, I_{s} and Y_{s} are inverter output current, inverter terminal voltage, Norton model source current and source admittance respectively.

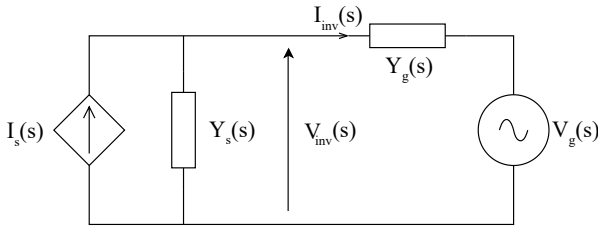

Figure 6.6: Grid-connected inverter harmonic model

The frequency dependent Norton impedance of the inverter can be determined using (6.28) and the corresponding Norton harmonic source current can be determined using (6.30) depending on the inverter controller configuration and the harmonic sequence. The harmonic currents (I_{inv}) injected by the inverter and the voltage harmonics (V_{inv}) which appear at the inverter terminal can be determined using FFT analysis under normal operating conditions.

Table 6.1: Key parameters of the three-phase inverters controlled in α-β and d-q reference frames

Parameter	Value (α-β)	Value (d-q)
Rated power	10 kW	2.5 MW
DC link voltage	1 kV	1kV
Inverter switching frequency	5 kHz	3kHz
Low pass filter Inverter side inductor	0.0013 H	11.68 μH 0.000367 Ω
Low pass filter Grid side inductor	0.0002 H	-
Low pass filter capacitor	20 μF	4819.33 μF
Grid voltage/frequency	0.38 kV / 50 Hz	0.4 kV / 50 Hz

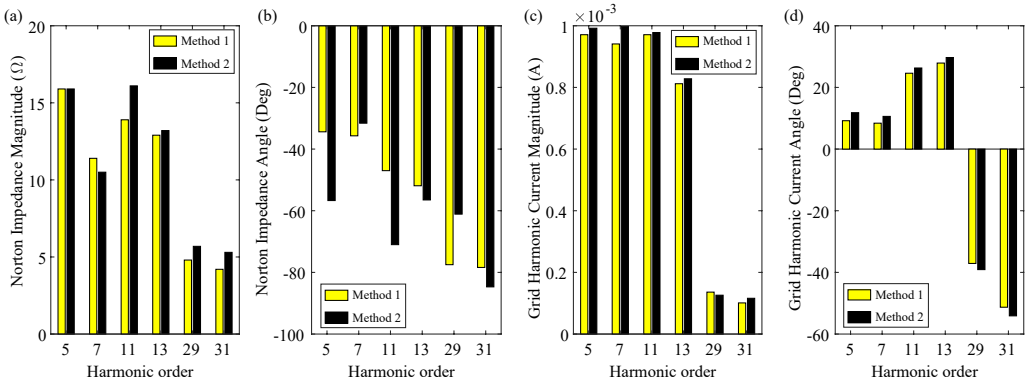

Figure 6.7: Inverter Norton impedances and grid harmonic currents of the grid connected three-phase inverter controlled in the α-β reference frame

6.2.4 Results and Discussion

Key parameters of the grid connected three-phase inverter controlled in the α-β reference frame and d-q reference frame are given in Table 6.1. The Norton model parameters determination process using (6.1), (6.28), (6.29) and (6.30) for these inverters will be referred to as 'Method 1' hereinafter. The Norton model parameters for each of the above grid connected inverters were also determined using the traditional harmonic injection method where each of these inverters was modelled in PSCAD^{TM}. This approach will be referred to as 'Method 2' hereinafter.

In addition to inverter parameters corresponding to low order harmonic orders (e.g. 5th, 7th, 11th, 13th), that are usually of significant concern with regard to three-phase grid-connected inverters, those associated with higher order harmonics (e.g. 29th and 31st), were also determined to examine the robustness of the theoretical methodology. It is worthy of noting that the higher order harmonics are sometimes known to be problematic with regard to large scale inverters used in solar farms.

The calculated harmonic model impedances using 'Method 1' and 'Method 2' for the

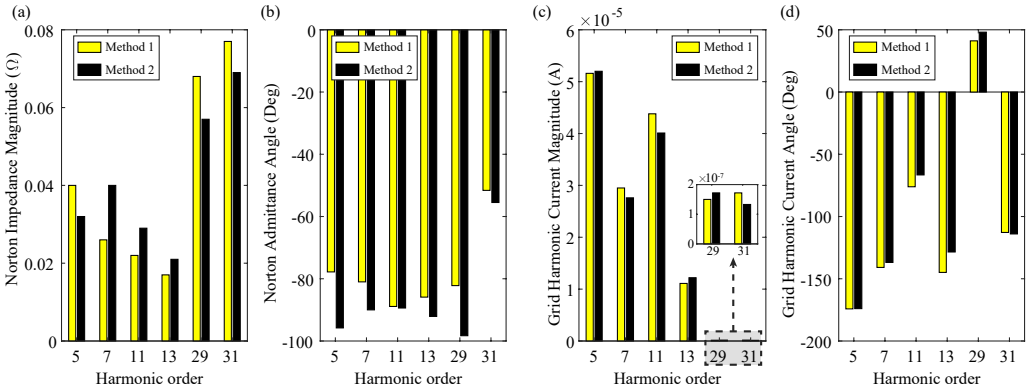

Figure 6.8: Inverter Norton impedances and grid harmonic currents of the grid connected three-phase inverter controlled in the d-q reference frame

inverter controlled in the α-β reference frame are shown in Figures 6.7 (a) and (b), and the same calculated for the inverter controlled in the d-q reference frame are shown in Figures 6.8 (a) and (b). From these, it is evident that the Norton equivalent circuit parameters calculated using 'Method 1' closely resemble those calculated using 'Method 2'.

In addition, the harmonic currents injected to the grid as predicted by 'Method 1' were compared with the actual harmonic currents observed utilising the PSCAD^{TM} simulations of the grid connected inverters. The results are shown in Figures 6.7 (c) and (d) for the inverter controlled in the α-β reference frame and Figures 6.8 (c) and (d) for the inverter controlled in the d-q reference frame, where it can be observed that there is close agreement between grid harmonic currents determined using 'Method 2' and the same determined using 'Method 1'.

6.3 Development of Mathematical Expressions for Output Impedance of Three Phase Inverters Considering the dc Link Dynamics

In the previous section, mathematical expressions were developed for three-phase inverter output impedance, assuming the inverter dc link to be constant. In this section, the focus is to develop mathematical expressions for inverter output impedance considering the dynamics of both ac and dc systems of the network containing three phase inverter developed in Chapter 4.

The ac and dc systems of the network in a grid connected inverter system are interconnected through the inverter, and hence, in the determination of the inverter output impedance, it is necessary to consider the dc system of the network as well considering its dynamics. If a sinusoidal small signal perturbation is applied to the ac side of the network, a small signal perturbation will also appear on the dc side of the inverter reflected in

both dc voltage (V_{dc}) and dc current (I_{dc}). If the voltage perturbation is at either positive sequence ($f_z + f_1$) or negative sequence ($f_z - f_1$), where, f_1 is the fundamental frequency, the perturbation which arise on the dc side of the inverter reflected in both V_{dc} and I_{dc} are at the frequency of f_z after convolution with the modulation signals. Similarly, if a small sinusoidal perturbation is applied to the dc side of the inverter network, which is at the frequency of f_z, then the small signal perturbations that will appear on the ac side of the network are at the frequencies of $f_z + f_1$ and $f_z - f_1$, which are at positive and negative sequence frequencies respectively.

This clearly shows that the dc and ac sides of an inverter are coupled together and hence, the coupling cannot simply be ignored when deriving mathematical expressions for three-phase inverter output impedance. Hence, in this study, the mathematical expressions for the inverter output impedance are derived considering both dc and ac network dynamics of the inverter and for that, (6.2) can be modified as shown in (6.31) [80], in which the first column and the first row capture the coupling between the dc and ac network dynamics of the three-phase inverter.

$$\begin{pmatrix} \bar{I_{dc}} \\ \bar{I_p} \\ \bar{I_n} \end{pmatrix} = \begin{pmatrix} Y_{dd} & Y_{dp} & Y_{dn} \\ Y_{pd} & Y_{pp} & Y_{pn} \\ Y_{nd} & Y_{np} & Y_{nn} \end{pmatrix} \begin{pmatrix} \bar{V_{dc}} \\ \bar{V_p} \\ \bar{V_n} \end{pmatrix} \tag{6.31}$$

where, $\bar{I_{dc}}$ and $\bar{V_{dc}}$ are the small signal representation of the inverter input dc current and the dc voltage respectively. Y_{dd}, Y_{dp}, Y_{dn}, Y_{pd} and Y_{nd} denote the components in the admittance matrix which can be defined as follows:

$$Y_{dd} = \frac{\bar{I}_{dc}}{\bar{V}_{dc}}, Y_{dp} = \frac{\bar{I}_{dc}}{\bar{V}_p}, Y_{dn} = \frac{\bar{I}_{dc}}{\bar{V}_n}, Y_{pd} = \frac{\bar{I}_p}{\bar{V}_{dc}}, Y_{nd} = \frac{\bar{I}_n}{\bar{V}_{dc}} \tag{6.32}$$

Considering the ac side of the inverter, since an LC filter is connected at the inverter output, same as the three-phase inverter model used in Section 6.2.2, (6.33) can be used to express the relationship between the inverter ac side current and the voltage.

$$V_{\mathrm{dc}} K_m m_{\mathrm{a,b,c}} = (Ls + R) i_{\mathrm{a,b,c}} + (LCs^2 + RCs + 1) v_{\mathrm{a,b,c}} \tag{6.33}$$

where, L is the LC filter inductance, R is the internal resistance of the inductor, C is the capacitance of the LC filter. V_{dc} is the dc link voltage, $m_{a,b,c}$ denote the modulation signals, $v_{a,b,c}$ are the voltages at the inverter terminals for the three phases and $i_{a,b,c}$ are the inverter three phase output currents.

The link between the three phase inverter output currents and the current flowing through the inverter dc link can be shown using (6.34).

$$I_{dc} = m_a i_a + m_b i_b + m_c i_c \tag{6.34}$$

where, I_{dc} is the inverter dc link current, and i_a, i_b and i_c are the currents at the inverter output.

This can be expressed in the d-q domain as,

$$I_{dc} = \frac{3}{2}(m_d I_d + m_q I_q) \tag{6.35}$$

If small signal voltage perturbations in positive sequence and negative sequence are injected from the ac side of the network as given in (6.4), the expressions for Y_{pp} and Y_{nn} can be determined following the steps given in Section 6.2.2.

If a small signal voltage perturbation is applied in the positive sequence from the ac side of the inverter, as a result of the applied voltage perturbation, a current perturbation will induce on the dc side of the inverter. Neglecting the coupling between the positive sequence and negative sequence current components on the ac side to reduce the complexity, an expression can be derived, extending equation (6.35) as,

$$\bar{I_{dc}} = \frac{3}{2}(\bar{m_d} I_d + m_d \bar{I_d} + \bar{m_q} I_q + m_q \bar{I_q}) \tag{6.36}$$

If m_d and m_q are the steady-state modulation signals in the d-q reference frame and, if I_1 denote the steady state d-axis current, using (6.12) and (6.36) an expression for $\bar{I_{dc}}$ can be derived as,

$$\bar{I_{dc}} = \frac{3(V_1 + \omega_1 L I_1)}{2K_m V_{dc}} \bar{I_p} + \frac{3}{2}(-H_i(s - j2\pi f_1) + jK_d)\bar{I_p} I_1 \tag{6.37}$$

Neglecting the three-phase inverter PLL dynamics, from (6.13) and (6.37) an expression for Y_{dp} can be derived as,

$$Y_{dp} = \frac{-3}{2K_m V_{dc}} \cdot \frac{(LCs^2 + RCs + 1 - K_{pwm} V_{dc} K_f)(V_1 + [-H_i(s - j2\pi f_1) + jK_d] I_1 V_{dc} K_m - j\omega_1 L I_1)}{(Ls + R) + V_{dc}[-H_i(s - j2\pi f_1) + jK_d]} \tag{6.38}$$

Assuming a negative sequence voltage perturbation that is injected from the ac side of the inverter, adhering to the same procedure, an expression for the Y_{dn} can be derived as given in (6.39).

$$Y_{dn} = \frac{-3}{2K_m V_{dc}} \cdot \frac{(LCs^2 + RCs + 1 - K_{pwm} V_{dc} K_f)(V_1 - [-H_i(s - j2\pi f_1) + jK_d] I_1 V_{dc} K_m + j\omega_1 L I_1)}{(Ls + R) + V_{dc}[H_i(s - j2\pi f_1) + jK_d]} \tag{6.39}$$

To determine the other unknown parameters of Y_{dd}, Y_{pd} and Y_{nd} in the impedance matrix given in (6.31), a small signal perturbation of $\bar{V_{dc}}$ can be added to the dc bus voltage V_{dc}. Therefore, with a dc voltage perturbation, from (6.33), (6.40) can be derived:

$$(Ls+R)\bar{i_{abc}} = K_m(V_{dc}\bar{m_{abc}} + \bar{V_{dc}}m_{abc}) \tag{6.40}$$

Therefore, from (6.12) and (6.40), expressions for Y_{pd} and Y_{nd} can be derived as given in (6.41) and (6.42) respectively.

$$Y_{pd} = \frac{(V_1 + j\omega_1 LI_1)}{2V_{dc}[Ls+R+H_i(s-j\omega)K_mV_{dc} - jK_dK_mV_{dc}]} \tag{6.41}$$

Adhering to the same procedure, an expression for Y_{nd} can be derived as shown in (6.42).

$$Y_{nd} = \frac{(V_1 - j\omega_1 LI_1)}{2V_{dc}[LS+R+H_i(s+j\omega)K_mV_{dc} + jK_dK_mV_{dc}]} \tag{6.42}$$

From (6.13), (6.38) and (6.41), an expression for Y_{dd} can be derived as given in (6.43).

$$Y_{dd} = \frac{3}{2K_mV_{dc}^2}\frac{(V_1 + \omega_1 LI_1 + K_mV_{dc}[-H_i(s-j\omega)+jK_d]I_1)(V_1 + j\omega_1 LI_1)}{Ls+R+H_i(s-j\omega)K_mV_{dc} - jK_dK_mV_{dc}} \tag{6.43}$$

6.3.1 Determination of the Inverter Output Impedance Considering the Inverter dc Link Dynamics

In the determination of the positive and negative sequence ac impedances at the inverter output, two aspects need to be followed which are given below:

- When establishing the sequence impedance of the inverter, the coupling between the negative and positive sequence ac currents was neglected to reduce the complexity of the equations.
- The $\bar{V_{dc}}$ and $\bar{I_{dc}}$ terms are eliminated using the dc network impedance Z_{dc}

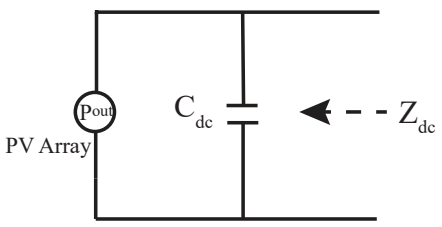

Figure 6.9: Simplified dc network of the inverter

The dc network of the considered three-phase inverter model consists of the PV array, dc-dc boost converter and the MPPT controller. However, to simplify the study, an approximate expression for the inverter dc network impedance is derived using the power output of the PV array (P_{out}) as shown in (6.44):

$$Z_{dc}(s) \approx \left(\frac{P_{out}}{V_{dc}^2} + sC_{dc} \right)^{-1} \tag{6.44}$$

Hence, expressions for the positive and negative sequence ac side impedances can be derived using (6.31) - (6.43) and (6.44) as shown in (6.45) and (6.46).

$$Z_p(s) = \frac{Y_{dp}(s-j\omega_1)Y_{pd}(s-j\omega_1) - Y_{pp}(s-j\omega_1)Y_{dd}(s-j\omega_1) - Z_{dc}(s-j\omega_1)^{-1}Y_{pp}(s-j\omega_1)}{Z_{dc}(s-j\omega_1)^{-1} + Y_{dd}(s-j\omega_1)} \tag{6.45}$$

$$Z_n(s) = \frac{Y_{dn}(s+j\omega_1)Y_{nd}(s+j\omega_1) - Y_{pp}(s+j\omega_1)Y_{dd}(s+j\omega_1) - Z_{dc}(s+j\omega_1)^{-1}Y_{nn}(s+j\omega_1)}{Z_{dc}(s+j\omega_1)^{-1} + Y_{dd}(s+j\omega_1)} \tag{6.46}$$

6.3.2 Results and Discussion

The key parameters of the ac network of the considered three-phase inverter system are the same as the three-phase inverter controlled in the d-q reference frame in Section 6.2. The parameters are given in Table 6.1. The dc link capacitor (C_{dc}) is 4000 μF. The inverter output impedances were determined for the most significant harmonic orders of 5^{th}, 7^{th}, 11^{th} and 13^{th} harmonic orders using the equations derived in ((6.45) and (6.46)) and compared with the results with the sequence impedances determined using the EMT simulations and the results are given in Table 6.2.

Table 6.2: Inverter output impedance

Harmonic order	Impedance from the EMT simulation model (Ω)	Impedance from the mathematical expressions (Ω)
5	$0.014 \angle 30.26^\circ$	$0.065 \angle 64.56^\circ$
7	$0.030 \angle 23.19^\circ$	$0.061 \angle 57.16^\circ$
11	$0.047 \angle 76.55^\circ$	$0.015 \angle 67.76^\circ$
13	$0.027 \angle 85.76^\circ$	$0.013 \angle 71.59^\circ$

As it can be seen from the results given in Table 6.2, the inverter output impedances de-

termined using EMT simulations compared with those obtained using mathematical formulations for the positive and negative sequence inverter output impedances show some discrepancies. Although the magnitudes derived using both methods seem to have the same order, the magnitudes are seen to be significantly different. There can be quite a few reasons for these discrepancies and a few of the major reasons are listed below:

- Omission of PLL dynamics caused by the perturbation injection, when determining the inverter output impedances in positive and negative sequences.
- Omission of the grid voltage feed forward of the inverter current controller to simplify the equations when deriving the admittance matrix components except for the Y_{pp} and Y_{nn}.
- Omission of the dc-dc boost converter dynamics and the effect of the MPPT controller when determining the dc side impedance of the inverter.

6.4 Chapter Summary

Inverter manufacturers provide the worst-case inverter Thevenin/Norton model parameters alongside the inverters to use in pre-compliance harmonic studies. The exact method used by the inverter manufacturers to determine these parameters is unknown as it is an intellectual property of the inverter manufacturer. However, it is clear that the inverter manufacturers use site measurements and calculations based approaches to determine the inverter harmonic model parameters.

The output impedance of an inverter depends on the controllers used in the inverter, PLL dynamics, the low-pass filter used, inverter modulation techniques and many other inverter internal parameters. Hence, in this chapter considering a few different inverter configurations, mathematical formulations were carried out for the inverter output impedance in the frequency domain. If the inverter output impedance and one set of inverter output current and voltage combination are known, then the Norton source current for the corresponding harmonic order can be easily determined. Firstly, mathematical expressions for the inverter output impedance were derived considering two, three-phase inverter configurations, which are controlled in α-β and d-q reference frames. The two configurations have different control strategies and different inverter parameters; however, both were assumed to have a constant dc link voltage. The inverter output impedances for the most significant harmonic orders were determined employing the mathematical formulations and were noted to be approximately equal to those determined employing EMT simulations.

The mathematical expressions for the inverter output impedance were derived considering a three-phase inverter model, in which the dc link is not constant. In this exercise,

the sequence impedances determined employing the derived mathematical expressions were seen to have some discrepancies compared with those determined using EMT simulations. The accuracy of the derived mathematical expressions determined in this chapter can be further improved by considering the PLL dynamics, the effect of the grid voltage feed forward, the active/reactive power and/or the dc link voltage controller dynamics, by adding the effects of the voltage/current filters if there are any, and by adding the inverter/grid transformer dynamics etc. However, by doing so, the complexity of the mathematical expressions of the inverter output impedance will increase, which can be identified as a disadvantage in using mathematical based methods to determine the inverter output impedances.

Chapter 7

Preliminary Studies on Cross Harmonic Generation by Grid Connected Inverters

7.1 Introduction

With regard to the use of Thevenin/Norton models of inverters in harmonic compliance studies, it is common to consider the pre-existing background harmonics of the same order as those produced by the inverters themselves in determining the resultant harmonic voltage levels at the PCC thus applying superposition, often employing summation laws. In practice, there is the possibility that a background harmonic voltage of given order (or a voltage with a certain frequency) can lead to the inverter injecting a harmonic current of a distinctly different order or orders in addition to that of the background harmonic. This phenomenon, which is commonly known as cross harmonic generation [81]–[84], cannot be ignored with regard to grid connected inverters.

Taking a simplistic view on cross harmonic generation, considering an inverter that injects a positive sequence harmonic current with a frequency f_p to the grid, when injected with a harmonic voltage of the same frequency from the grid side will lead to currents at frequencies f_p and $f_p - 2f_1$ where f_1 is the fundamental frequency of the system. Similarly, with a negative sequence harmonic with a frequency f_n, the resulting harmonic currents at the PCC will have frequencies f_n and $f_n + 2f_1$. The frequency components at $f_p - 2f_1$ and $f_n + 2f_1$ will be identified as principal cross modulation components as the process of cross modulation can lead to other frequency components which may not be dominant.

Depending on the phase angles of the background harmonic voltages, the level of influence can be to strengthen or weaken the pre-existing levels of harmonic currents at frequencies f_p or f_n. Thevenin/Norton models so far used to examine the behaviour

at a single harmonic order obviously are simply unsuitable if there is significant cross harmonic generation. For example, in the case of the 7^{th} harmonic, which is a positive sequence harmonic, the generation of the 5^{th} harmonic as a result of cross harmonic phenomena can be significantly different from what is predicted using the 5^{th} harmonic Thevenin/Norton model equivalent so far used noting that such low order harmonics are of high significance with regard to large scale inverters. Same argument applies to 5^{th} harmonic, which is a negative sequence harmonic that leads to 7^{th} harmonic.

Following are the key reasons have been identified as the causes of cross harmonic generation by grid connected inverters [85]:

- Asymmetrical d-q axis current control
- Dc link voltage controller that affects d axis current controlling only
- PLL that regulates the q axis voltage component to generate the angle response. This also leads to asymmetric control in three phase inverters.

Noting the complexity of the whole cross harmonic generation process associated with inverters, the primary aim of this chapter is to carry out a limited number of studies considering only the first level of cross harmonic generation assuming only the background harmonic voltages and the principal components of the cross harmonic frequencies. Further, only a single background harmonic voltage is considered at a time. The work presented is essentially EMT simulation based as the development of a theoretical framework on the whole cross harmonic generation process was considered to be outside the scope of the thesis.

7.2 Examination of Cross Harmonic Generation by Grid Connected Inverters

The cross harmonic generation phenomenon of three-phase grid-connected inverters was examined using the three-phase grid-connected inverter EMT model developed in Chapter 4, neglecting the cable network. Commonly known to exist 5^{th}, 7^{th}, 11^{th} and 13^{th} harmonic voltages were considered on the grid side with only one harmonic at a time and with their application, the resultant harmonic spectrum of the grid current was observed for each case. The harmonic voltage magnitude injected from the grid side for the harmonic orders considered was 0.354 kV (line-to-neutral RMS, which is 0.46% of 132 kV) with 0° phase angle.

Figure 7.1 shows the harmonic spectrum of the output current as a percentage of the rated current when the three-phase grid connected inverter operates at the rated power level with no background voltage harmonics present in the grid.

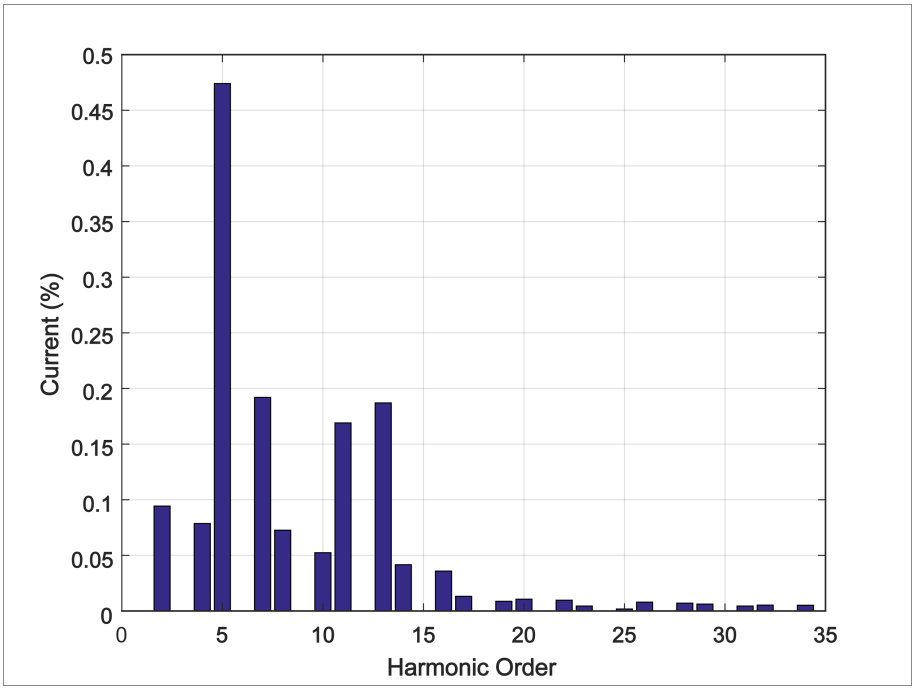

Figure 7.1: Current harmonics at the PCC at the inverter rated power

Figure 7.2 shows the percentage change in the current harmonics at the PCC from 2nd harmonic to 19th harmonic when the grid fundamental voltage is individually superimposed with 5th, 7th, 11th and 13th harmonics.

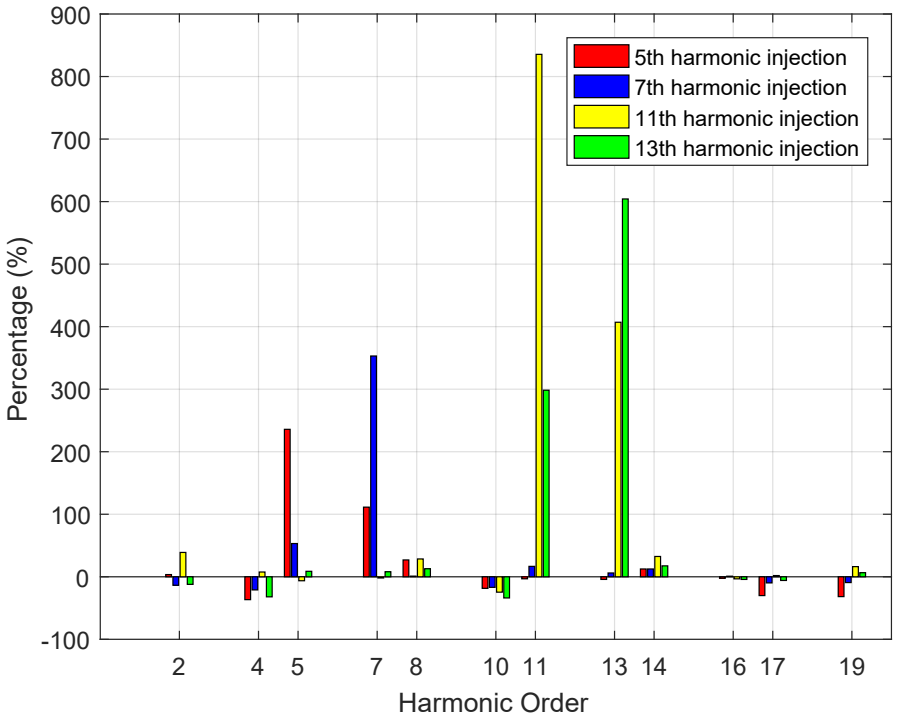

Figure 7.2: Percentage change in harmonic currents at the PCC

From Figure 7.2, it is evident that when 5th harmonic voltage is injected from the grid

side, both 5^{th} and 7^{th} harmonic currents at the PCC show a significant increase, but not at the other harmonic orders. A significant change in the 5^{th} and 7^{th} harmonic currents at the PCC can also be observed when the fundamental grid voltage is superimposed with the 7^{th} harmonic voltage. This trend is evident with the 11^{th} and 13^{th} harmonic orders as well, thus illustrating the phenomena of cross harmonic modulation.

7.3 Variation of the Harmonic Currents at the PCC With the Magnitude of the Harmonic Voltage on the Grid

Although the cross harmonic generation phenomenon is well-known, the nature of variation of generated cross harmonic current magnitudes with different grid harmonic levels has not been investigated to-date, which is the focus of this section. For each considered harmonic order, the injected harmonic voltage magnitude on the grid was varied from 0.354 kV (0.46%) to 1.414 kV (1.86%), and the magnitudes of harmonic current at the same frequency as the injected voltage and the corresponding dominant cross harmonic frequency were observed. The results obtained are illustrated in Figure 7.3.

From Figure 7.3, in general, it is evident that as the injected harmonic voltage increases, both the harmonic current at the injected frequency and the harmonic current at cross harmonic frequency (principal component) increase in proportion to the injected harmonic voltage. Further, corresponding to each injected frequency, the magnitudes of the two harmonic current components are comparable, suggesting that the cross harmonic current cannot be ignored. It is to be noted, as observed in Figure 7.2, the injected harmonic voltage has the most influence on the current at the same harmonic order and the current at the cross harmonic frequency (principal component) and not on the currents at other harmonic orders, which is an important observation.

7.3.1 Variation of the Harmonic Currents at the PCC With the Magnitude and Phase Angle Variation of the 5^{th} Harmonic Voltage Applied on the Grid

The magnitude of the harmonic currents (both at the perturbation frequency and the principal cross harmonic frequency) determined at the PCC can vary depending on the applied harmonic voltage magnitude and as well as the phase angle on the grid. Hence, the variation of the harmonic currents at the PCC was determined for harmonic voltage perturbations applied at the 5^{th} harmonic order for different harmonic voltage magnitudes varied from 0.354 kV (0.46%) to 1.414 kV (1.86%) and for each magnitude, for 60°, 120°, 180°, 240° and 300° phase angles. The results are shown in Figure 7.4.

From the results, it is evident that for all the considered phase angles, the harmonic cur-

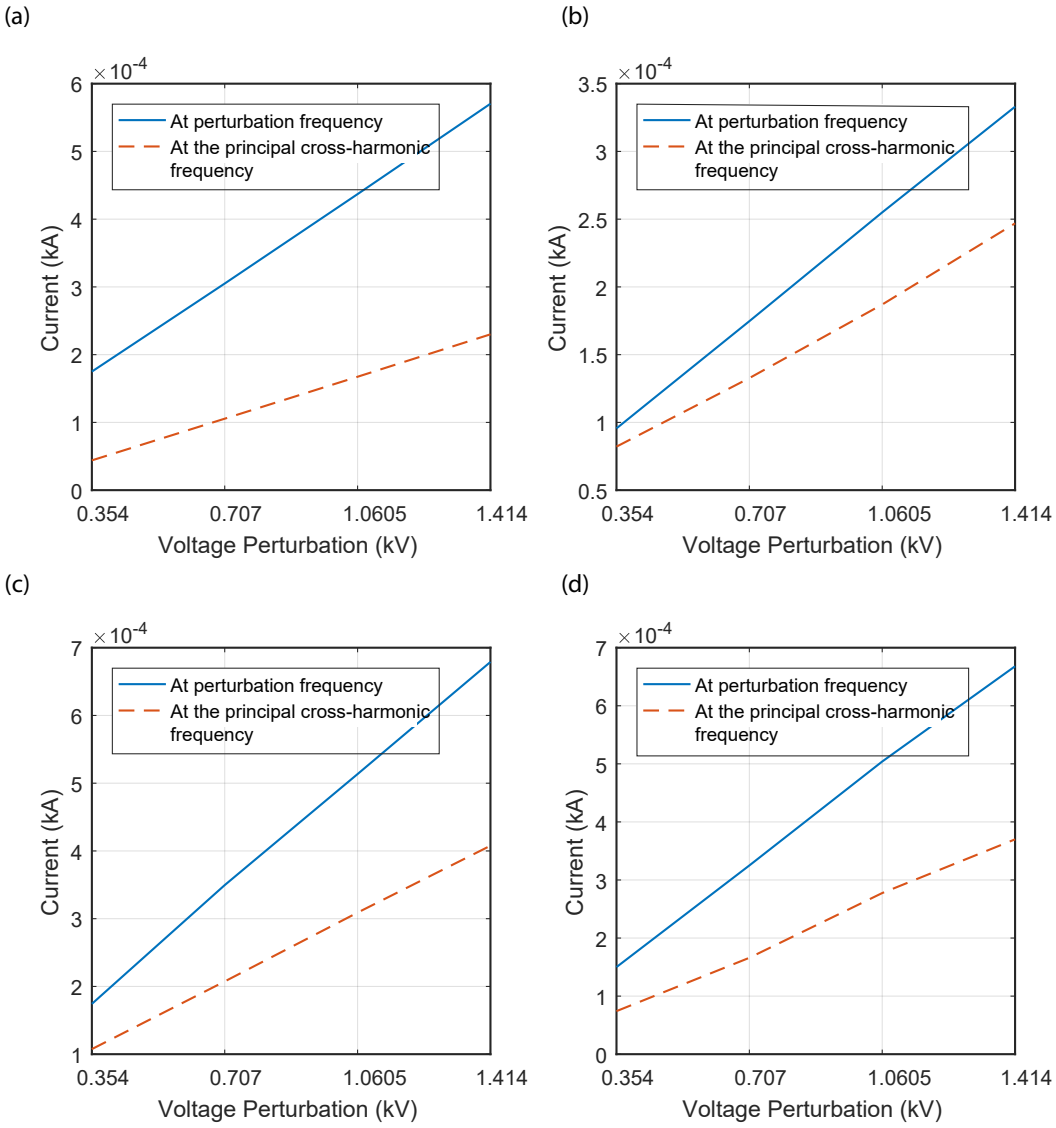

Figure 7.3: Variation of the harmonic currents with the injected harmonic voltage on the grid for (a) 5^{th} (b) 7^{th} (c) 11^{th} and (d) 13^{th} harmonic orders

rents determined at PCC at the perturbation frequency and the principal cross harmonic frequency show linear variation with the applied harmonic voltage perturbation magnitudes. Furthermore, from Figure 7.4 it is apparent that the magnitudes of the current harmonic components determined at PCC at the perturbation frequency and the principal cross harmonic frequency vary depending on the phase angle of the applied harmonic voltage at the grid.

Figure 7.5 shows the percentage change in the current harmonics at the PCC for 5^{th} harmonic and 7^{th} harmonic orders when the grid fundamental voltage is individually superimposed with 5^{th} harmonic voltage with 0.354 kV magnitude and 0°, 60°, 120°, 180° 240° and 300° phase angles.

From Figure 7.5 it is evident that even though the magnitudes of the currents at 5^{th} har-

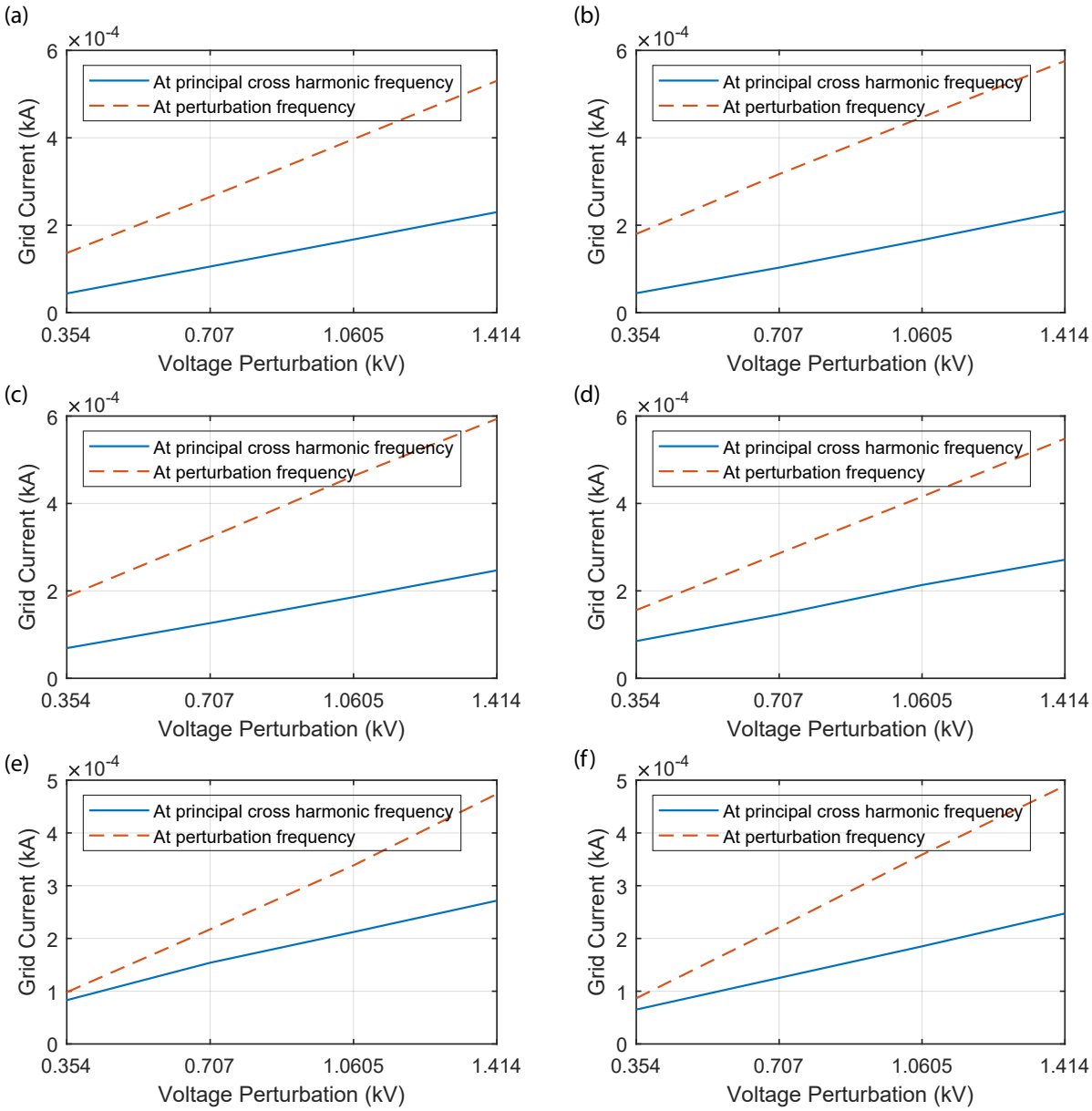

Figure 7.4: Variation of the harmonic currents with the injected harmonic voltage magnitude and phase angle on the grid for (a) 0° (b) 60° (c) 120° (d) 180° (e) 240° and (f) 300° phase angles for the 5th harmonic order

monic and 7th harmonic orders at the PCC have some fluctuations due to the phase angle variation of the applied harmonic voltage, the observed harmonic current magnitudes at the PCC always greater than the corresponding harmonic currents at the PCC when the grid is not superimposed with harmonic voltages.

The cross harmonic current generation depending on the applied harmonic voltage magnitude and phase angle was only observed and analysed for the 5th harmonic voltage application only for a few randomly selected phase angles, as the EMT simulations take extensive time to complete the simulations.

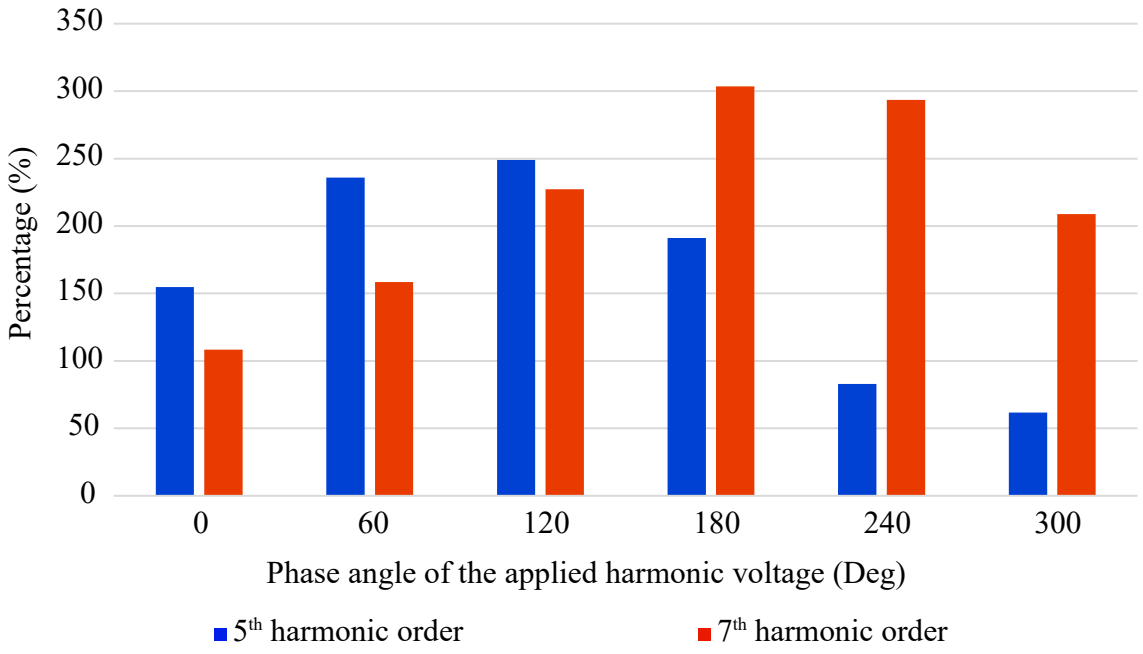

Figure 7.5: Percentage change in harmonic currents at the PCC when 5th harmonic voltage applied at the grid with 0.354 kV magnitude and different phase angles

7.4 Modified Inverter Harmonic Model Incorporating Cross Harmonic Generation

The most commonly used method of theoretical determination of Thevenin/Norton harmonic model parameters of inverters is the harmonic injection or harmonic perturbation method as elaborated in Chapter 5, where such models do not have the capability to predict harmonic currents injected at the cross harmonic frequencies. As the cross-harmonic current magnitudes may not be negligible, it is proposed that two Norton models be adopted, one at the perturbation injected frequency and the other at the principal cross-harmonic frequency, considering the worst-case emission levels.

With the positive sequence perturbation applied from the grid side, the grid-connected Norton models at the perturbation frequency and the principal cross harmonic frequency can be shown in Figure 7.6 where $V_p(s)$ is the positive sequence harmonic perturbation voltage present in the grid. $Y_g(s)$ and $Y_g(s-2j\omega_1)$ represent the grid impedance at the positive sequence and the corresponding mirror harmonic frequencies. $Y_p(s)$ and $Y_n(s)$ are the positive and negative sequence inverter output impedances, and $i_p(s)$ and $i_p(s-j2\omega_1)$ are the Norton model source currents at the perturbation frequency and the cross harmonic frequency respectively. The same concept can be applied where a negative sequence harmonic voltage perturbation is present in the grid.

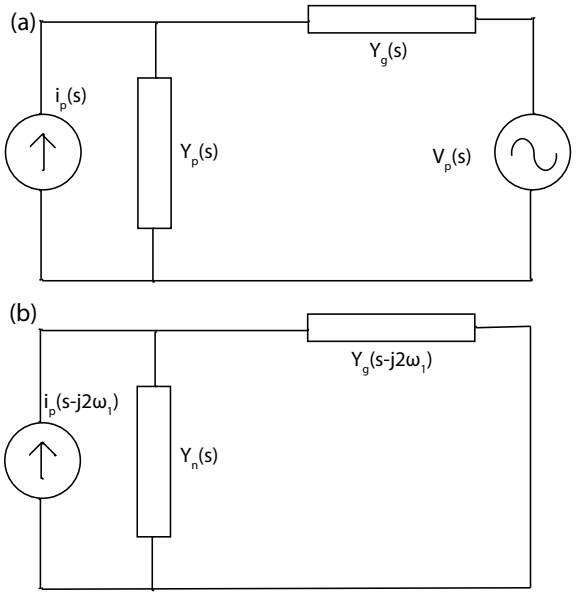

Figure 7.6: Norton models of inverter in the presence of a positive sequence harmonic voltage in the grid (a) at injected positive sequence frequency and (b) at the principal cross harmonic frequency

7.4.1 Norton Model Parameter Determination at the Cross Harmonic Frequency

It was shown in Chapter 5 that the Norton model source current and the Norton admittance at the perturbation frequency can be determined using (5.4) where it was observed that both the Norton/Thevenin admittance/impedance and source current/voltage are nearly constant and independent of the harmonic perturbation voltage magnitude at the perturbation injection frequency. Hence it can be concluded that the grid injected harmonic current at the perturbation frequencies will exhibit an increasing trend due to the applied harmonic voltage perturbation magnitudes, as seen in Figure 7.3 in the worst case, when the applied perturbations are in 0° phase angle.

Since the inverter output impedance for each harmonic order depends mainly on inverter internal parameters such as low-pass filter parameters, modulation technique used and the dc link voltage (refer Section 6.4), the inverter output impedance was assumed to be constant for each harmonic order when determining the Norton/Thevenin model parameters at the cross harmonic frequency.

As shown in Figure 7.7, when a positive sequence voltage perturbation is applied from the grid side, a current at the cross harmonic frequency can be observed at the inverter terminals ($i_{inv}(s-j2\omega_1)$) and as a result of that current, a voltage at the same frequency is generated at the inverter terminals ($v_{inv}(s-j2\omega_1)$). Since the inverter output impedance at the cross harmonic frequency is already known ($Y_n(s)$), if the voltage and current at the cross-harmonic frequency at the inverter terminals are known, the Norton source current at the cross-harmonic frequency ($i_p(s-j2\omega_1)$) can be determined using (7.1).

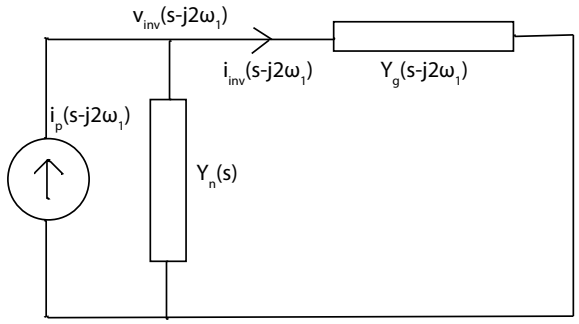

Figure 7.7: Norton model of an inverter in the presence of a positive sequence harmonic voltage in the grid at the principal cross harmonic frequency

$$i_p(s-j2\omega_1) = Y_n(s)v_{inv}(s-j2\omega_1) + i_{inv}(s-j2\omega_1) \tag{7.1}$$

At cross harmonic frequencies, an important observation made through EMT simulation studies was that when the applied voltage perturbation magnitude varies, the Norton/Thevenin source current/voltage also varies. For instance, the inverter cross harmonic Thevenin model parameters are calculated by applying 7^{th} harmonic voltage perturbation levels of 0.141 kV and 0.007 kV (RMS), the calculated 5^{th} harmonic (which is the cross harmonic order) Thevenin model parameters are as follows.

- with 0.141kV: Thevenin impedance = $0.014 \angle 30.27^\circ\ \Omega$, Thevenin voltage = $2.383 \times 10^{-6} \angle 103.78^\circ$ kV
- with 0.007kV: Thevenin impedance = $0.014 \angle 30.27^\circ\ \Omega$, Thevenin voltage = $1.266 \times 10^{-6} \angle 75.42^\circ$ kV

From the above data, it can be observed that, with an increasing harmonic injected voltage magnitude, the grid injected cross harmonic current also increases as a result of its link to the injected harmonic voltage, as seen from Figure 7.3. Therefore, the harmonic Norton model source current at the cross harmonic frequency can be considered to be dependent on the applied perturbation voltage. This, in fact, is a drawback of the proposed harmonic model as the Norton source current at the cross harmonic frequency is based on the applied perturbation voltage. However, knowing the linearly increasing behaviour of the cross harmonic current, the corresponding Norton source current can be predicted for a given background harmonic voltage level.

The derived Norton model parameters for the 5^{th}, 7^{th}, 11^{th} and 13^{th} harmonic orders are shown in Table 7.1 for an injected harmonic voltage magnitude of 0.354 kV.

Table 7.1: Harmonic Norton model parameters

Harmonic order of the applied voltage	Norton model parameters at the applied harmonic voltage		Norton model parameters at the principal cross harmonic frequency	
	Admittance (S)	Source Current (kA)	Admittance (S)	Source Current (kA)
5	62.2-j36.3	$0.031\angle$-110.2°	30.2-j12.9	$0.020\angle$-17.1°
7	30.2-j12.9	$9.625 \times 10^{-3}\angle$108.7°	62.2-j36.3	$0.048\angle$-63.9°
11	4.9+j20.6	$2.552 \times 10^{-3}\angle$-51.8°	2.7+j36.8	$0.013\angle$-71.2°
13	2.7+j36.8	$2.502 \times 10^{-3}\angle$-10.9°	4.9+j20.6	$0.007\angle$ -58.9°

7.5 Cross Harmonic Generation in a Multiple Inverter Environment

In this section, the variation of the grid currents at cross harmonic frequencies is investigated in the presence of a total of four parallel grid-connected inverters (neglecting the cable network) employing both EMT models and the developed Norton models. Although this case does not represent a realistic solar farm environment as the cable network was not considered for the simulation studies, some key understandings of cross harmonic generation can still be developed through the work presented. In this study, 5^{th}, 7^{th}, 11^{th} and 13^{th} harmonic voltages were injected from the grid side. For the convenience of analysis of the cross harmonic currents injected to the grid by the inverters, only one harmonic was injected at a time having a magnitude of 0.354 kV at 0° phase angle. The grid harmonic currents at the voltage harmonic injection frequency and the corresponding cross harmonic frequency current magnitudes observed using both the EMT and Norton models are illustrated by Figure 7.8, as the number of inverters is increased from 1 to 4.

From Figure 7.8, it is evident that the injected harmonic grid currents measured at the harmonic injection frequencies and at the corresponding cross-harmonic frequencies increase almost linearly for the considered harmonic orders with the number of inverters. Furthermore, it can be concluded that the derived inverter Norton models are capable of closely predicting the grid harmonic currents for all the considered cases. From these test results, it can be concluded that inverters can be represented with two Norton models for each harmonic order in the presence of a single voltage harmonics present in the grid.

It is to be noted that in an actual solar farm environment, there is a cable network. While it is the practice to use derived Norton models associated with the inverters that are independent of the associated external impedances at a particular grid injected frequency, the cross harmonic Norton model independently derived requires attention with regard to its source current as it is dependent on the external injected harmonic voltage. In such situations, the source current needs adjustment iteratively.

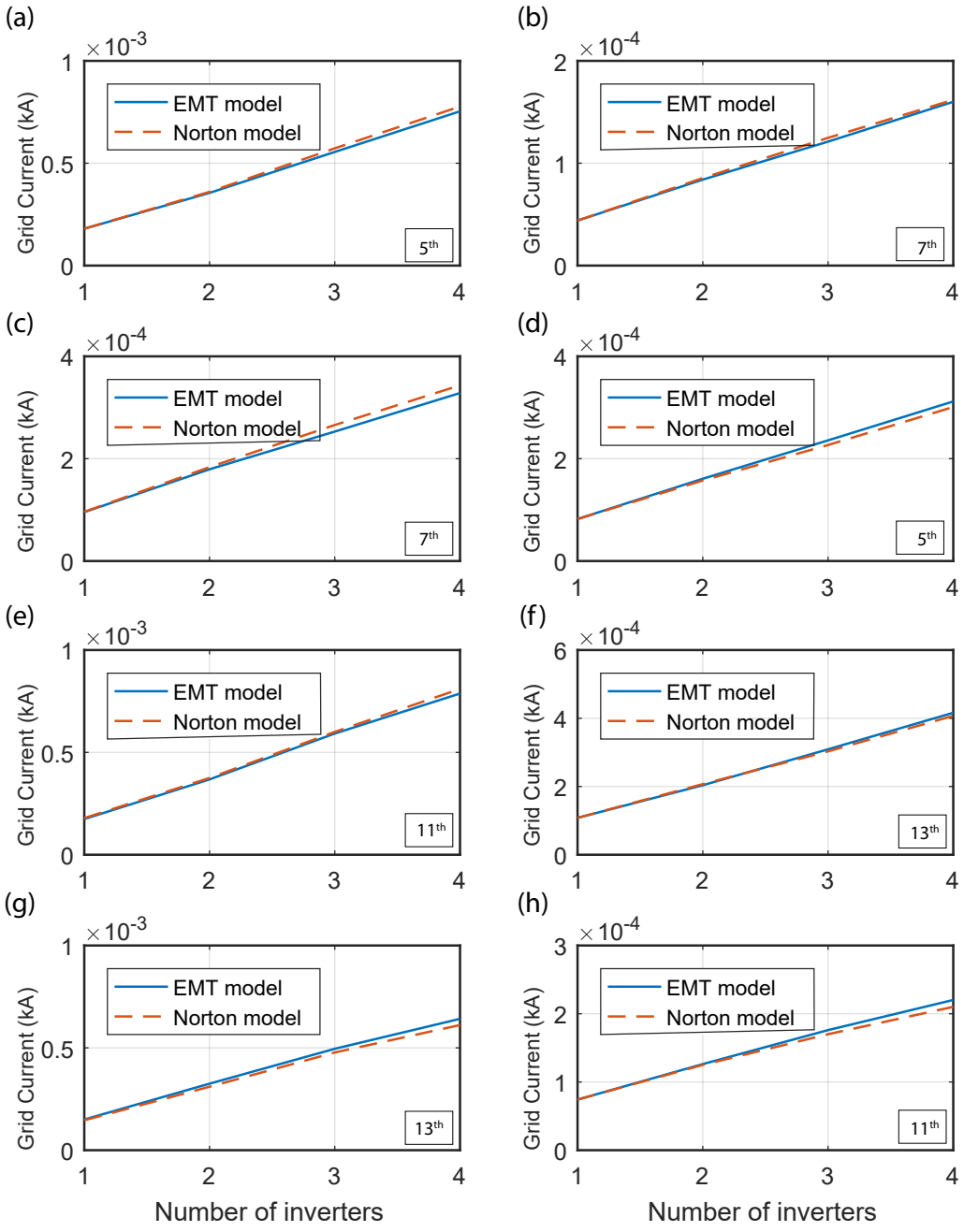

Figure 7.8: Grid injected harmonic currents, Case 1: Injected harmonic - 5th harmonic order; (a) at 5th harmonic and (b) at 7th harmonic, Case 2: Injected harmonic - 7th harmonic order, (c) at 7th harmonic and (d) at 5th harmonic, Case 3: Injected harmonic - 11th harmonic order, (e) at 11th harmonic and (f) at 13th harmonic, Case 4: Injected harmonic - 13th harmonic order, (g) at 13th harmonic and (h) at 11th harmonic

The cross harmonic generation phenomenon becomes increasingly complex when there are multiple voltage harmonics present at the grid, which in fact, is well known. For instance, with both 5th and 7th harmonic order voltages present in the grid, harmonic currents at both 5th and 7th harmonic orders will exhibit a change. The resulting cross harmonic current induced at 7th harmonic order may contribute to a change in the voltage harmonic at 7th harmonic order. Both the original applied grid harmonic voltage and

the new cross harmonic voltage at 7^{th} harmonic order will contribute to change the cross harmonic current generation at 5^{th} harmonic order, which will eventually affect the 5^{th} harmonic grid voltage.

7.6 Chapter Summary

Cross harmonic generation is a known phenomenon which may arise with grid-connected inverters, especially when the grid is polluted with pre-existing harmonic voltages. Although this phenomenon is often neglected, the case studies given in this chapter show that the generated cross harmonic currents can have substantial magnitudes, which cannot be ignored in harmonic studies. The nature of cross harmonic generation under variable grid voltage harmonic magnitude levels and phase angles was also investigated in this chapter. It was observed from the case studies that the cross harmonic current magnitudes increase linearly for the considered harmonic orders with the injected voltage perturbation magnitude.

The parameters of the Norton/Thevenin models commonly used in harmonic studies developed using the well-known perturbation injection method fail to represent the harmonic currents generated at the cross harmonic frequencies. Noting that cross-harmonic current magnitudes may not be negligible, the development of two Norton models was proposed to represent inverter harmonic behaviour, one at the perturbation injected frequency and the other at the cross harmonic frequency. However, the Norton source currents at the cross harmonic frequencies depend on the voltage perturbation injection magnitude and this was identified as a limitation of the proposed inverter harmonic model. This limitation can be overcome by taking a pragmatic view assuming the worst-case scenario, in which the background harmonic voltages in the grid are at the network planning levels and hence no adjustments may be required.

Chapter 8

Conclusions and Recommendations for Future Work

8.1 Conclusions

In harmonic compliance studies associated with renewable energy sources integrated to electricity grids employing power electronic converters, it is the common practice to use Norton/Thevenin models that are usually provided by the vendors of such converter systems. In this regard, the focus of this thesis was the large scale inverters in solar farms where the suitability of such models was examined as there is no concrete evidence to the effect that such models represent the true harmonic behaviour in actual environments. This is mainly because of the fact that the vendor provided models are developed in isolation with no reference to where the inverters will be ultimately connected and often they are worst case harmonic models. One method of examining their suitability is to compare the outcomes from such models with those obtained using EMT models that are able to represent a whole range of internal and external variables of inverters. The main objective of this thesis was the examination of this suitability and to investigate possible improvements that can be applied with regard to suitable models.

Although inverter EMT models are generally available from their vendors, the crucial control system and other important parameters, including the details and the depth of modelling that can influence the harmonic behaviour are contained within black-boxes that are not publicly available. Therefore, carrying out objective sensitivity studies associated with the harmonic behaviours of inverters is prohibitive. As it was mandatory to develop a thorough understanding of the inverter operation to study their harmonic behaviour, a large-scale inverter EMT model was initially developed, followed by the development of a solar farm model with realistic parameters employing PSCAD^{TM}.

With a view to compare the outcomes derived employing EMT models with corresponding Norton/Thevenin models, one of the major requirements of the work undertaken

was the development of such frequency domain models. It is understood that inverter vendors employ hybrid approaches in developing worst case harmonic models where simulations, calculations and or experimental procedures are used. However, details of such work are not publicly available. In this regard, this thesis utilised the harmonic injection approach to develop Norton/Thevenin models of the developed EMT models.

A sensitivity study was carried out to examine how the Norton/Thevenin models perform in comparison to inverter EMT models under different inverter internal and external conditions. From this study, it was concluded that for most of the inverter internal and external conditions, when the number of inverters in the solar farm increases, the inverter Norton/Thevenin harmonic models cannot accurately replicate the true harmonic behaviour as predicted by the EMT models. Furthermore, interactions were noted to occur between the Thevenin model impedance and the impedance of the rest of the network, exhibiting resonances which do not actually exist as demonstrated by the inverter EMT models, thus hinting possible inaccuracies that can arise in harmonic compliance studies which employ frequency domain Norton/Thevenin models.

With EMT models, it was also noted that the harmonic currents generated by inverters in a solar farm vary specially with different grid conditions. This also clearly shows that an inverter cannot be accurately modelled using a fixed Norton/Thevenin model.

The applicability of the arithmetic summation and the general summation laws in establishing the aggregated harmonic current at the PCC was also investigated in this thesis, where it was noted that the arithmetic summation can be used reasonably confidently.

Mathematical expressions for frequency domain harmonic model parameters were also derived in this thesis. This was done using three inverter models, in which two inverter models were characterised by constant dc link voltage, whereas the third model covered the complete dc system of the inverter. The mathematically derived inverter harmonic model parameters exhibited quite good agreement with the determined inverter Norton/Thevenin model parameters of the cases with constant dc link voltage. By using this approach applied in the determination of harmonic model parameters, a thorough understanding of the association between the inverter control system and inverter parameters with the inverter Norton/Thevenin model parameters can be achieved. Furthermore, to determine the harmonic model parameters using the proposed mathematical-based method, the approach requires only one set of inverter terminal voltage and current measurements at the required harmonic order, which makes the application of the methodology quite convenient.

Norton/Thevenin models of inverters being single harmonic frequency models, are naturally unable to demonstrate the cross harmonic generation phenomena demonstrated by their EMT models in the presence of background harmonic voltages in the connected grid. Therefore, a preliminary study was undertaken to determine the behaviour associated with cross harmonics generated by inverters. From this study, it was noted that the

cross harmonics generated by the inverters cannot be neglected, noting their magnitudes. Furthermore, the magnitudes of the cross harmonics generated by inverters linearly increase with the applied grid voltage harmonic magnitude, an observation which may not be general, but nonetheless was considered as a crucial observation that is relevant to the development of suitable models to characterise cross harmonic generation. In this thesis, a novel inverter harmonic model which consists of two Norton models was proposed to represent the harmonics generated by the inverters, such that one Norton model represents the harmonic behaviour of the inverter at the background harmonic frequency (the injected frequency) and the other Norton model represents the cross harmonics injected by the inverter. However, the drawback of this composite model is that the Norton source current at the cross harmonic frequency varies depending on the applied grid voltage magnitude. This can be mitigated to some extent as it is already known from the studies that the generated cross harmonic magnitude varies with the applied grid voltage magnitude linearly. Therefore, worst-case cross harmonic Norton model parameters can be derived by assuming the grid voltage harmonic magnitude to be equal to the corresponding planning level.

From the studies presented in this thesis, it can be concluded that the currently used (Norton/Thevenin models) may not be suitable for replicating the true harmonic behaviour of the inverters on many occasions, especially in solar farm environments, where a large number of inverters are connected together with a cable network, and also under different inverter internal and external conditions.

8.2 Recommendations for Future Work

In this thesis, the determined frequency domain harmonic model parameters of inverters were used to investigate the suitability of using Norton/Thevenin models. Assuming the availability of EMT models that are declared to be suitable for harmonic studies and the corresponding Norton/Thevenin models, a side-by-side comparison should be carried out to examine the level of agreement between the two approaches. Further, the vendor-provided EMT models should be used in developing the corresponding Norton/Thevenin models using the harmonic injection method so that they can be compared with the vendor-provided Norton/Thevenin models. A range of studies should be undertaken to investigate the influence of different operating conditions on the behaviour of these models and compare the results with the results obtained using EMT models.

Using the outcomes presented in this thesis, it was concluded that when the inverters operate at the rated power level, the aggregated harmonic current of a solar farm at the PCC can be determined by applying arithmetic summation, given that all inverters within a solar farm are identical. This study should be extended so that the validity of the arithmetic summation and the general summation laws can be investigated under different

inverter internal conditions and grid conditions.

The mathematical expressions derived for inverter harmonic model parameters for three-phase inverters with pure dc link voltage, controlled in α-β and d-q reference frames, are suitable for replacing the traditional software-based methods for determining the Norton/Thevenin model parameters. However, with the entire dc system that comprises the PV array, dc-dc boost converter and the MPPT controller, derivation of the mathematical expressions for the inverter output impedance becomes quite complex. The work presented in this thesis shows that this challenge has been achieved to some extent. However, the mathematical formulations presented in this thesis can be further improved by considering the dynamics of the PV array, the boost converter, the MPPT controller, the dc link voltage controller and the reactive power controller as well.

The cross harmonic currents generated by the inverters were noted to be substantial in their magnitudes in the preliminary study undertaken. The studies presented and the outcomes are limited in depth as only a single voltage harmonic was considered to be present in the grid with 0° phase angle. These studies need to be extended such that the grid consists of multiple voltage harmonics with different phase angles to investigate the range of variations of the various cross harmonics with a view to improve the proposed models or to develop new models.

One of the major obstacles faced in many of the studies undertaken in this thesis is the extensive time taken to complete EMT simulations employing quite small numerical time steps, although the inverter switching frequency was set at 3 kHz. The issue of simulation time becomes more problematic in solar farm environments with multiple inverters. For this reason, it is unlikely that EMT simulations will be used in harmonic studies, especially in relation to large solar farms, which may consist of much more inverters than what was considered in this thesis. Hence, it is recommended that suitable hybrid approaches are developed which are suitable for such studies with a view to achieve more realistic and accurate outcomes.

While theoretical modelling and simulation-based approaches are considered to form the backbone of harmonic studies, it is vital that such outcomes are validated using appropriate experimental and field validation. The absence of such validation was prohibitive with regard to the studies undertaken, considering the absence of true-to-life data from actual operating inverters, although actual internal and external network data could be procured. This aspect is prudent in future work undertaken in the area of high fidelity model development associated with solar farms.

Bibliography

[1] A. Yazdani and R. Iravani, *Voltage-sourced converters in power systems: modeling, control, and applications*. John Wiley & Sons, 2010.

[2] N. Mohan, T. M. Undeland, and W. P. Robbins, *Power electronics: converters, applications, and design*. John wiley & sons, 2003.

[3] B. K. Bose, *Power electronics and motor drives: advances and trends*. Academic press, 2020.

[4] S. H. Kim, *Electric motor control: DC, AC, and BLDC motors*. Elsevier, 2017.

[5] K. V. Kumar, P. A. Michael, J. P. John, and S. S. Kumar, "Simulation and comparison of spwm and svpwm control for three phase inverter," *ARPN journal of engineering and applied sciences*, vol. 5, no. 7, pp. 61–74, 2010.

[6] J. S. Kim and S. K. Sul, "A novel voltage modulation technique of the space vector pwm," *Chongi Hakhoe Nonmunchi (Transactions of the Korean Institute of Electrical Engineers)*, vol. 44, 1995.

[7] Y. Wu, C. Leong, and R. McMahon, "A study of inverter loss reduction using discontinuous pulse width modulation techniques," 2006.

[8] T. D. Nguyen, J. Hobraiche, N. Patin, G. Friedrich, and J.-P. Vilain, "A direct digital technique implementation of general discontinuous pulse width modulation strategy," *IEEE Transactions on Industrial Electronics*, vol. 58, no. 9, pp. 4445–4454, 2010.

[9] K. Zhou, Z. Qiu, N. R. Watson, and Y. Liu, "Mechanism and elimination of harmonic current injection from single-phase grid-connected pwm converters," *IET Power Electronics*, vol. 6, no. 1, pp. 88–95, 2013.

[10] Y. Yang, K. Zhou, and F. Blaabjerg, "Current harmonics from single-phase grid-connected inverters—examination and suppression," *IEEE Journal of Emerging and Selected Topics in Power Electronics*, vol. 4, no. 1, pp. 221–233, 2015.

[11] Y. Yang, K. Zhou, H. Wang, and F. Blaabjerg, "Harmonics mitigation of dead time effects in pwm converters using a repetitive controller," *2015 IEEE Applied Power Electronics Conference and Exposition (APEC)*, pp. 1479–1486, 2015.

[12] S.-H. Hwang and J.-M. Kim, "Dead time compensation method for voltage-fed pwm inverter," *IEEE Transactions on energy conversion*, vol. 25, no. 1, pp. 1–10, 2009.

[13] J.-W. Choi and S.-K. Sul, "Inverter output voltage synthesis using novel dead time compensation," *IEEE transactions on Power Electronics*, vol. 11, no. 2, pp. 221–227, 1996.

[14] J. Arrillaga, B. C. Smith, N. R. Watson, and A. R. Wood, *Power system harmonic analysis*. John Wiley & Sons, 1997.

[15] D. B. Rathnayake, S. M. H. K. Samarasinghe, C. I. Medagedara, and S. G. Abeyratne, "An enhanced pulse-based dead-time compensation technique for pwm-vsi drives," *2014 9th International Conference on Industrial and Information Systems (ICIIS)*, pp. 1–5, 2014.

[16] J. A. Houldsworth and D. A. Grant, "The use of harmonic distortion to increase the output voltage of a three-phase pwm inverter," *IEEE Transactions on Industry Applications*, vol. IA-20, no. 5, pp. 1224–1228, 1984.

[17] L. Chaturvedi, D. Yadav, and G. Pancholi, "Comparison of spwm, thipwm and pdpwm technique based voltage source inverters for application in renewable energy," *Journal of Green Engineering*, vol. 7, no. 1, pp. 83–98, 2017.

[18] J. Jose, G. Goyal, and M. Aware, "Improved inverter utilisation using third harmonic injection," *2010 Joint International Conference on Power Electronics, Drives and Energy Systems and 2010 Power India*, pp. 1–6, 2010.

[19] A. Bosman, J. Cobben, J. Myrzik, and W. Kling, "Harmonic modelling of solar inverters and their interaction with the distribution grid," *Proceedings of the 41st International Universities Power Engineering Conference*, vol. 3, pp. 991–995, 2006.

[20] A. E. Fitzgerald, C. Kingsley, S. D. Umans, and B. James, *Electric machinery*. McGRAW-hill New York, 2003, vol. 5.

[21] I. Daut, S. Hasan, and S. Taib, "Magnetizing current, harmonic content and power factor as the indicators of transformer core saturation," *Journal of Clean Energy Technologies*, vol. 1, no. 4, pp. 304–307, 2013.

[22] S. N. Vukosavic, *Grid-side converters control and design*. Springer, 2018.

[23] N. Pjevalica, N. Petrovic, V. Pjevalica, and N. Teslic, "Experimental detection of transformer excitation asymmetry through the analysis of the magnetizing current harmonic content," *Elektronika ir Elektrotechnika*, vol. 22, no. 2, pp. 43–48, 2016.

[24] "Ieee standard for interconnection and interoperability of distributed energy resources with associated electric power systems interfaces," *IEEE Std 1547-2018 (Revision of IEEE Std 1547-2003)*, pp. 1–138, 2018.

[25] IEC, "Iec 61727: Photovoltaic (pv) systems - characteristics of the utility interface," 2004.

[26] IEC, "Tr 61000-3-6 electromagnetic compatibility (emc) - part 3-6: Limits - assessment of emission limits for the connection of distorting installations to mv, hv and ehv power systems," 2008.

[27] M. Jansen, "Harmonic compliance assessment and mitigation design in renewable energy networks," *CIGRE Australia CIDER 17 event*, 2017.

[28] AEMC, *National Electricity Rules*. Version 180, 2022.

[29] J. Arrillaga and N. R. Watson, *Power system harmonics*. John Wiley & Sons, 2004.

[30] A. Abdalrahman, A. Zekry, and A. Alshazly, "Simulation and implementation of grid-connected inverters," *International Journal of Computer Applications*, vol. 60, no. 4, 2012.

[31] S. Rogalla, F. Ackermann, N. Bihler, H. Moghadam, and O. Stalter, "Source-driven and resonance-driven harmonic interaction between pv inverters and the grid," *2016 IEEE 43rd Photovoltaic Specialists Conference (PVSC)*, pp. 1399–1404, 2016.

[32] E. C. Aprilia, V. Ćuk, J. Cobben, P. F. Ribeiro, and W. L. Kling, "Modeling the frequency response of photovoltaic inverters," *2012 3rd IEEE PES Innovative Smart Grid Technologies Europe (ISGT Europe)*, pp. 1–5, 2012.

[33] J. Leung, D. Chong, and T. George, "Solar power plant harmonic emission-design and commissioning case study," *DIgSILENT Pacific Melbourne*, 2017.

[34] A. Timbus, M. Liserre, R. Teodorescu, P. Rodriguez, and F. Blaabjerg, "Evaluation of current controllers for distributed power generation systems," *IEEE Transactions on power electronics*, vol. 24, no. 3, pp. 654–664, 2009.

[35] S. M. Cherati, N. A. Azli, S. M. Ayob, and A. Mortezaei, "Design of a current mode pi controller for a single-phase pwm inverter," *2011 IEEE Applied Power Electronics Colloquium (IAPEC)*, pp. 180–184, 2011.

[36] S. Golestan, M. Monfared, J. M. Guerrero, and M. Joorabian, "A d-q synchronous frame controller for single-phase inverters," *2011 2nd Power Electronics, Drive Systems and Technologies Conference*, pp. 317–323, 2011.

[37] R. Teodorescu, F. Blaabjerg, M. Liserre, and P. C. Loh, "Proportional-resonant controllers and filters for grid-connected voltage-source converters," *IEE Proceedings-Electric Power Applications*, vol. 153, no. 5, pp. 750–762, 2006.

[38] L. F. A. Pereira, J. V. Flores, G. Bonan, D. F. Coutinho, and J. M. G. da Silva, "Multiple resonant controllers for uninterruptible power supplies—a systematic robust control design approach," *IEEE Transactions on Industrial Electronics*, vol. 61, no. 3, pp. 1528–1538, 2014.

[39] C. Rech, H. Pinheiro, H. Grundling, H. Hey, and J. Pinheiro, "Analysis and design of a repetitive predictive-pid controller for pwm inverters," *2001 IEEE 32nd Annual Power Electronics Specialists Conference (IEEE Cat. No.01CH37230)*, vol. 2, 986–991 vol.2, 2001.

[40] H. Häberlin, *Photovoltaics: system design and practice*. John Wiley & Sons, 2012.

[41] G. M. Masters, *Renewable and efficient electric power systems*. John Wiley & Sons, 2013.

[42] B. K. Perera, S. R. Pulikanti, P. Ciufo, and S. Perera, "Simulation model of a grid-connected single-phase photovoltaic system in pscad/emtdc," *2012 IEEE International Conference on Power System Technology (POWERCON)*, pp. 1–6, 2012.

[43] B. Hasaneen and A. A. E. Mohammed, "Design and simulation of dc/dc boost converter," *2008 12th International Middle-East Power System Conference*, pp. 335–340, 2008.

[44] A. Reznik, M. G. Simões, A. Al-Durra, and S. M. Muyeen, "Lcl filter design and performance analysis for small wind turbine systems," *2012 IEEE Power Electronics and Machines in Wind Applications*, pp. 1–7, 2012.

[45] J. Xu, S. Xie, and J. Kan, "Lcl-filter design for grid-connected inverter to suppress grid-induced low-order current harmonics," *2015 IEEE Energy Conversion Congress and Exposition (ECCE)*, pp. 1178–1183, 2015.

[46] R. Teodorescu, F. Blaabjerg, U. Borup, and M. Liserre, "A new control structure for grid-connected lcl pv inverters with zero steady-state error and selective harmonic compensation," *Nineteenth Annual IEEE Applied Power Electronics Conference and Exposition, 2004. APEC '04.*, vol. 1, 580–586 Vol.1, 2004.

[47] R. Teodorescu, F. Blaabjerg, and M. Liserre, "Proportional-resonant controllers. a new breed of controllers suitable for grid-connected voltage-source converters," *Journal of Electrical Engineering*, vol. 6, no. 2, pp. 6–6, 2006.

[48] R. Teodorescu, F. Blaabjerg, and M. Liserre, "Proportional-resonant controllers. a new breed of controllers suitable for grid-connected voltage-source converters," *Journal of Electrical Engineering*, vol. 6, no. 2, pp. 6–6, 2006.

[49] R. Teodorescu, F. Blaabjerg, M. Liserre, and P. C. Loh, "Proportional-resonant controllers and filters for grid-connected voltage-source converters," *IEE Proceedings-Electric Power Applications*, vol. 153, no. 5, pp. 750–762, 2006.

[50] C. Picardi, D. Sgro, and G. Gioffre, "A simple and low-cost pll structure for single-phase grid-connected inverters," *Power Electronics Electrical Drives Automation and Motion (SPEEDAM), 2010 International Symposium on*, pp. 358–362, 2010.

[51] M. Ciobotaru, R. Teodorescu, and F. Blaabjerg, "A new single-phase pll structure based on second order generalized integrator," *Power Electronics Specialists Conference, 2006. PESC'06. 37th IEEE*, pp. 1–6, 2006.

[52] H. S. Kim and S. K. Sul, "A novel filter design for output lc filters of pwm inverters," *Journal of Power Electronics*, vol. 11, no. 1, pp. 74–81, 2011.

[53] Y. W. Li, "Control and resonance damping of voltage-source and current-source converters with *lc* filters," *IEEE Transactions on Industrial Electronics*, vol. 56, no. 5, pp. 1511–1521, 2008.

[54] H. Kim and S. K. Sul, "Analysis on output lc filters for pwm inverters," *2009 IEEE 6th International Power Electronics and Motion Control Conference*, pp. 384–389, 2009.

[55] K. H. Ahmed, S. J. Finney, and B. W. Williams, "Passive filter design for three-phase inverter interfacing in distributed generation," *2007 Compatibility in Power Electronics*, pp. 1–9, 2007.

[56] R. Teodorescu, M. Liserre, and P. Rodriguez, *Grid converters for photovoltaic and wind power systems*. John Wiley & Sons, 2011, vol. 29.

[57] R. Kadri, J. P. Gaubert, and G. Champenois, "An improved maximum power point tracking for photovoltaic grid-connected inverter based on voltage-oriented control," *IEEE transactions on industrial electronics*, vol. 58, no. 1, pp. 66–75, 2010.

[58] S. Pillai and S. Thale, "Design and implementation of a three phase inverter for renewable energy source with unified control strategy," *Energy Procedia*, vol. 90, pp. 673–680, 2016.

[59] K. Zhou and D. Wang, "Relationship between space-vector modulation and three-phase carrier-based pwm: A comprehensive analysis [three-phase inverters]," *IEEE transactions on industrial electronics*, vol. 49, no. 1, pp. 186–196, 2002.

[60] Z. B. Ibrahim, M. L. Hossain, I. B. Bugis, N. M. N. Mahadi, and A. S. A. Hasim, "Simulation investigation of spwm, thipwm and svpwm techniques for three phase voltage source inverter," *International Journal of Power Electronics and Drive Systems*, vol. 4, no. 2, p. 223, 2014.

[61] A. M. Vural, "Pscad modeling of a two-level space vector pulse width modulation algorithm for power electronics education," *Journal of Electrical Systems and Information Technology*, vol. 3, no. 2, pp. 333–347, 2016.

[62] M. Gaballah, M. El-Bardini, S. Sharaf, and M. Mabrouk, "Implementation of space vector-pwm for driving two level voltage source inverters," *Journal of Engineering Sciences*, vol. 39, no. 4, pp. 871–884, 2011.

[63] Z. Zhang, M. Zhou, M. Xiang, and Y. Liu, "Pscad/emtdc based svpwm inverter simulation," *IET Journals*, 2012.

[64] A. Robert, T. Deflandre, E. Gunther, R. Bergeron, A. Emanuel, A. Ferrante, G. Finlay, R. Gretsch, A. Guarini, J. G. Iglesias, *et al.*, "Guide for assessing the network harmonic impedance," *14th International Conference and Exhibition on Electricity Distribution. Part 1. Contributions (IEE Conf. Publ. No. 438)*, vol. 2, pp. 3–1, 1997.

[65] T. J. Browne, "Harmonic management in transmission networks," 2008.

[66] C. working group B1.30, "Cable systems electrical characteristics," 2013.

[67] L. Hong, W. Shu, J. Wang, and R. Mian, "Harmonic resonance investigation of a multi-inverter grid-connected system using resonance modal analysis," *IEEE Transactions on Power Delivery*, vol. 34, no. 1, pp. 63–72, 2018.

[68] M. Bollen, S. Mousavi-Gargari, and S. Bahramirad, "Harmonic resonances due to transmission-system cables," no. 12, 2014.

[69] Olex, "Naxans olex high voltage cable catalogue," 2009.

[70] J. Sun, "Ac power electronic systems: Stability and power quality," *2008 11th Workshop on Control and Modeling for Power Electronics*, pp. 1–10, 2008.

[71] J. Sun, "Small-signal methods for ac distributed power systems–a review," *IEEE Transactions on Power Electronics*, vol. 24, no. 11, pp. 2545–2554, 2009.

[72] Y. Du, D. Lu, G. James, and D. J. Cornforth, "Modeling and analysis of current harmonic distortion from grid connected pv inverters under different operating conditions," *Solar Energy*, vol. 94, pp. 182–194, 2013.

[73] S. Rogalla, F. Ackermann, N. Bihler, H. Moghadam, and O. Stalter, "Source-driven and resonance-driven harmonic interaction between pv inverters and the grid," *2016 IEEE 43rd Photovoltaic Specialists Conference (PVSC)*, pp. 1399–1404, 2016.

[74] V. J. Gosbell, D. Robinson, S. Perera, and A. Baitch, "The application of iec 61000-3-6 to mv systems in australia," *Quality and Security of Electrical Supply Conference Proceedings*, pp. 7.1–7.1.10, 2001.

[75] J. Leung, D. Chong, and T. George, "Solar power plant harmonic emission-design and commissioning case study," *DIgSILENT Pacific Melbourne*, 2017.

[76] M. Cespedes and J. Sun, "Impedance modeling and analysis of grid-connected voltage-source converters," *IEEE Transactions on Power Electronics*, vol. 29, no. 3, pp. 1254–1261, 2013.

[77] M. Céspedes and J. Sun, "Modeling and mitigation of harmonic resonance between wind turbines and the grid," *2011 IEEE Energy Conversion Congress and Exposition*, pp. 2109–2116, 2011.

[78] M. Cespedes and J. Sun, "Impedance shaping of three-phase grid-parallel voltage-source converters," *2012 Twenty-Seventh Annual IEEE Applied Power Electronics Conference and Exposition (APEC)*, pp. 754–760, 2012.

[79] L. Hong, W. Shu, J. Wang, and R. Mian, "Harmonic resonance investigation of a multi-inverter grid-connected system using resonance modal analysis," *IEEE Transactions on Power Delivery*, vol. 34, no. 1, pp. 63–72, 2018.

[80] S. Shah and L. Parsa, "Impedance modeling of three-phase voltage source converters in dq, sequence, and phasor domains," *IEEE Transactions on Energy Conversion*, vol. 32, no. 3, pp. 1139–1150, 2017.

[81] M. Kazem Bakhshizadeh, X. Wang, F. Blaabjerg, J. Hjerrild, Ł. Kocewiak, C. L. Bak, and B. Hesselbæk, "Couplings in phase domain impedance modeling of grid-connected converters," *IEEE Transactions on Power Electronics*, vol. 31, no. 10, pp. 6792–6796, 2016.

[82] T. Reinikka, T. Roinila, and J. Sun, "Measurement device for inverter output impedance considering the coupling over frequency," *2020 IEEE 21st Workshop on Control and Modeling for Power Electronics (COMPEL)*, pp. 1–7, 2020.

[83] S. Song, Z. Wei, Y. Lin, B. Liu, and H. Liu, "Impedance modeling and stability analysis of pv grid-connected inverter systems considering frequency coupling," *CSEE Journal of Power and Energy Systems*, vol. 6, no. 2, pp. 279–290, 2020.

[84] A. Wood, D. Hume, and J. Arrillaga, "Cross-modulation of harmonics in hvdc schemes," *CIGRE, Paris, France, Working Group*, vol. 14,

[85] S. Song, Z. Wei, Y. Lin, B. Liu, and H. Liu, "Impedance modeling and stability analysis of pv grid-connected inverter systems considering frequency coupling," *CSEE Journal of Power and Energy Systems*, vol. 6, no. 2, pp. 279–290, 2020.

[86] A. M. Vural, "Pscad modeling of a two-level space vector pulse width modulation algorithm for power electronics education," *Journal of Electrical Systems and Information Technology*, vol. 3, no. 2, pp. 333–347, 2016.

Appendix A

Development of Space Vector Pulse Width Modulation User Defined Model

A.1 Space Vector Pulse Width Modulation

The theory behind the SVPWM method is well-documented. The most commonly used three phase inverter configurations used to-date in solar energy generation systems comprise of six IGBT switches and six anti-parallel diodes. Since two switches are turned on simultaneously each time, the inverter has altogether eight switching states comprised of six active vectors (100, 110, 010, 011, 001 and 101) and two zero vectors (000 and 111). These eight switching states are shown in Figure A.1.

The switching vectors facilitate continuous current at the inverter output without allowing the dc link to short circuit. The vectors can be represented graphically in the α - β plane and the active vectors divide the plane into six sectors which are apart from each other by 60° and the zero vectors are located at the origin of the plane. The reference vector can be located anywhere on the α - β plane and it can be approximated by switching its two adjacent active vectors and both zero vectors. This can be shown in Figure A.2. In this figure, V_0, V_1, V_2, V_3, V_4, V_5, V_6 and V_7 represent the switching vectors and the V_{ref} denotes the reference signal.

This appendix describes two methods of generating the switching pulses of the six inverter switches using the SVPWM method. In method 1, a user-defined SVPWM block is used to generate three phase duty cycle waveforms and the corresponding IGBT switching pulses can be generated externally by comparing the duty cycle waveforms with a carrier waveform. In method 2, a user defined component is used to produce the switching pulses directly without using any carrier waveform external to the user defined component.

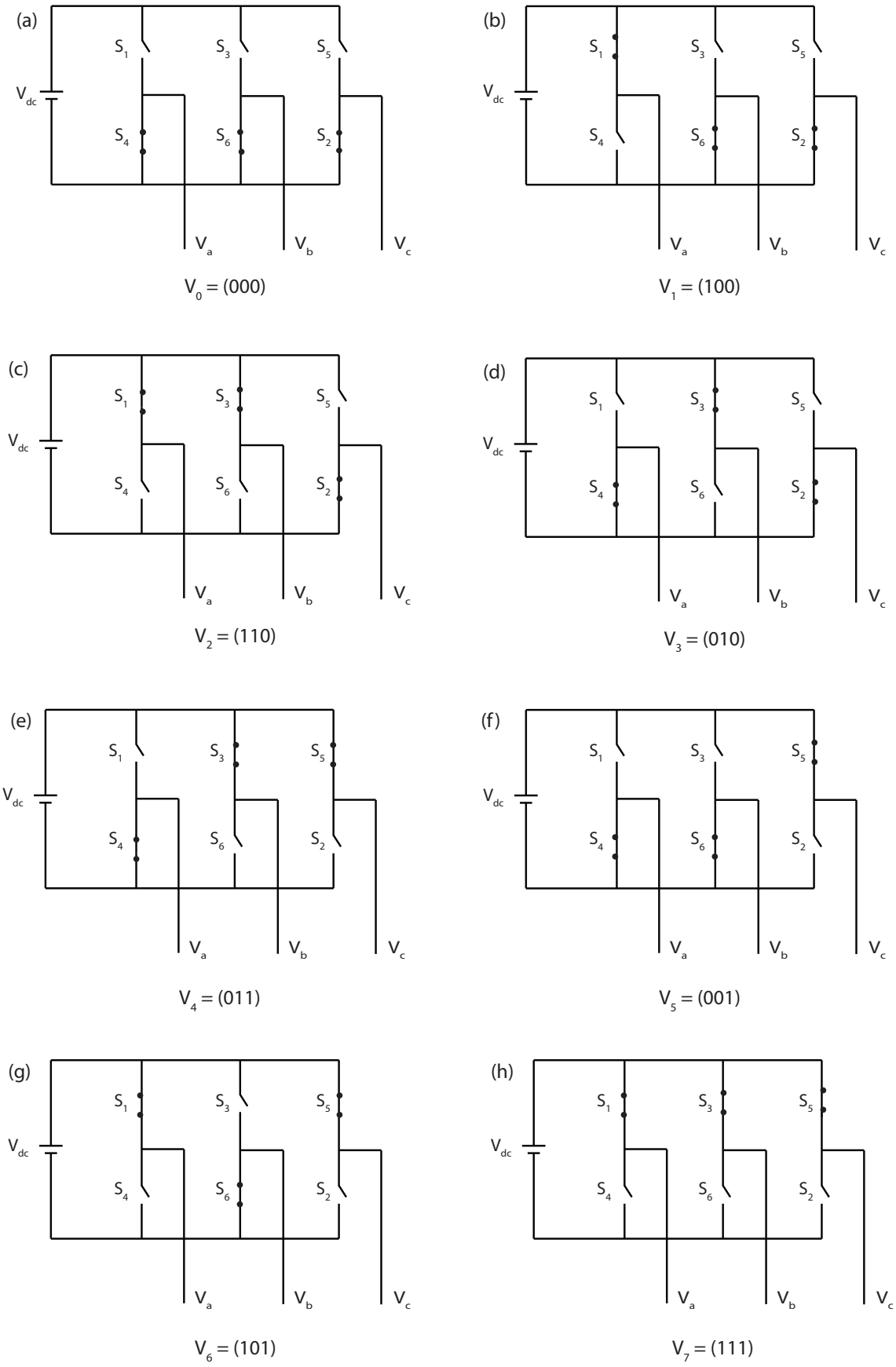

Figure A.1: Inverter switching states

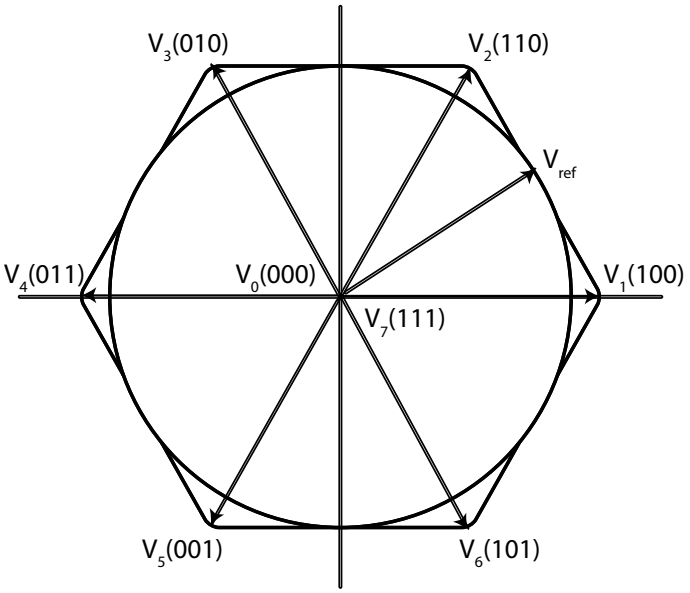

Figure A.2: Voltage source inverter output vectors in α-β plane

Method 1

The three phase reference waveforms generated by the current controller were converted into α-β reference frame using Clark transformation, such that the magnitude and the phase angle of the reference vector can be calculated. The corresponding part of the FORTRAN script is given below.

```
P=3.141592654
q=1.047197551
SQRT3=1.732050808


$mag=SQRT($Alpha**2+$Beta**2)


IF  (($Alpha>0).AND.($Beta>=0)) THEN
$angle=ATAN($Beta/$Alpha)
ELSEIF  (($Alpha>0).AND.($Beta<0)) THEN
$angle=ATAN($Beta/$Alpha)+(2*p)
ELSEIF  (($Alpha==0).AND.($Beta>0)) THEN
$angle=P/2
ELSEIF  (($Alpha==0).AND.($Beta<0)) THEN
$angle=(3*P/2)
ELSEIF  ($Alpha<0) THEN
$angle=ATAN($Beta/$Alpha)+P
ENDIF
```

Using the determined phase angle of the reference vector, the exact sector where the reference signal is located was determined. The reference vector lies in any sector can

be replicated using the adjacent two active vectors and one zero vector. Following the identification of the corresponding active and zero vectors, the turning on time for each vector was estimated [62].

```
1  IF  (($angle>=0).AND.($angle<=P/3)) THEN
2  $sector=1
3  ELSEIF  (($angle>P/3).AND.($angle<=2*P/3)) THEN
4  $sector=2
5  ELSEIF  (($angle>2*P/3).AND.($angle<=P)) THEN
6  $sector=3
7  ELSEIF  (($angle>P).AND.($angle<=4*P/3)) THEN
8  $sector=4
9  ELSEIF  (($angle>4*P/3).AND.($angle<=5*P/3)) THEN
10 $sector=5
11 ELSEIF  (($angle>5*P/3).AND.($angle<=2*P)) THEN
12 $sector=6
13 ENDIF
```

For instance, if the reference signal is located in sector 1 as shown in Figure A.3, it can be represented with the two active vectors of V_1, V_2 and the zero vector V_0. If the activation times of these vectors are T_1, T_2 and T_0 respectively, the duration of the reference vector can be calculated with (A.1).

$$V_{ref}T_s = V_1T_1 + V_2T_2 + V_0T_0 \tag{A.1}$$

where, T_s=1/switching frequency (f_s).

Since the position of all the vectors can be described with their corresponding magnitude and angle, (A.1) can be modifies as the equation given in (A.2).

$$\begin{aligned} T_s|V_{ref}|\cos(\alpha) &= \frac{2}{3}T_1V_{dc} + \frac{2}{3}T_2V_{dc}\cos\left(\frac{\pi}{3}\right) \\ T_s|V_{ref}|\sin(\alpha) &= \frac{2}{3}T_2V_{dc}\sin\left(\frac{\pi}{3}\right) \end{aligned} \tag{A.2}$$

where, $|V_{ref}|$ is the magnitude of the reference signal, V_{dc} is the inverter dc link voltage and α is the phase angle of the reference signal.

Hence, the switching times for each vector can be determined using (A.3).

$$\begin{aligned} T_1 &= \frac{\sqrt{3}.T_s.|V_{ref}|}{V_{dc}}\,(sin\,(\pi/3-\alpha)) \\ T_2 &= \frac{\sqrt{3}.T_s.|V_{ref}|}{V_{dc}}\,(sin\,(\alpha)) \\ T_0 &= T_s-(T_1+T_2) \end{aligned} \tag{A.3}$$

This can be expanded such that the time durations for the active and zero vectors are calculated for any location of the reference vector. If the reference vector is located at sec-

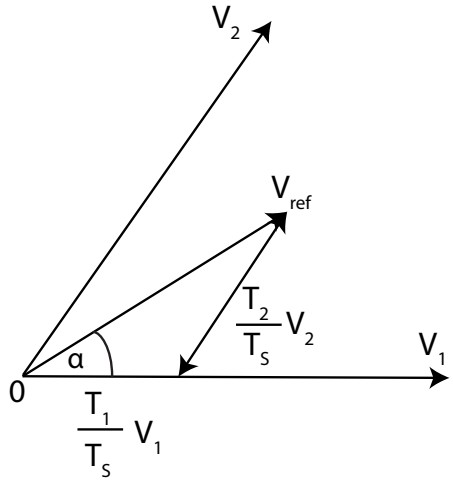

Figure A.3: Reference vector located in sector 1

tor n, the activation times for the corresponding active and zero vectors can be calculated using (A.4).

$$\begin{aligned} T_1 &= \frac{\sqrt{3}.T_s.|V_{ref}|}{V_{dc}} \left(sin\left(\frac{n\pi}{3} - \alpha\right)\right) \\ T_2 &= \frac{\sqrt{3}.T_s.|V_{ref}|}{V_{dc}} \left(sin\left(\alpha - \frac{n-1}{3}\pi\right)\right) \\ T_0 &= T_s - (T_1 + T_2) \end{aligned} \tag{A.4}$$

Table A.1: Sequence of the vectors with respect to time

sector	$T_0/2$	T_1	T_2	T_0	T_1	T_2	$T_0/2$
1	V_0	V_1	V_2	V_7	V_2	V_1	V_0
2	V_0	V_3	V_2	V_7	V_2	V_3	V_0
3	V_0	V_3	V_4	V_7	V_4	V_3	V_0
4	V_0	V_5	V_4	V_7	V_4	V_5	V_0
5	V_0	V_5	V_6	V_7	V_6	V_5	V_0
6	V_0	V_1	V_6	V_7	V_6	V_1	V_0

Table A.1 shows the vectors activated at each time based on the sector where the reference vector is located. Hence, depending on the reference vector location, the activation times of the corresponding vectors can be calculated using the FORTRAN script below:

```
1 IF (sector==1) THEN
2 Ta=(SQRT3*mag*Ts*SIN(q-angle))/Vdc
3 Tb=(SQRT3*mag*Ts*SIN(angle))/Vdc
4 T0=Ts-Ta-Tb
5 ELSEIF (sector==2) THEN
6 Ta=(SQRT3*mag*Ts*SIN(2*q-angle))/Vdc
7 Tb=(SQRT3*mag*Ts*SIN(angle-q))/Vdc
```

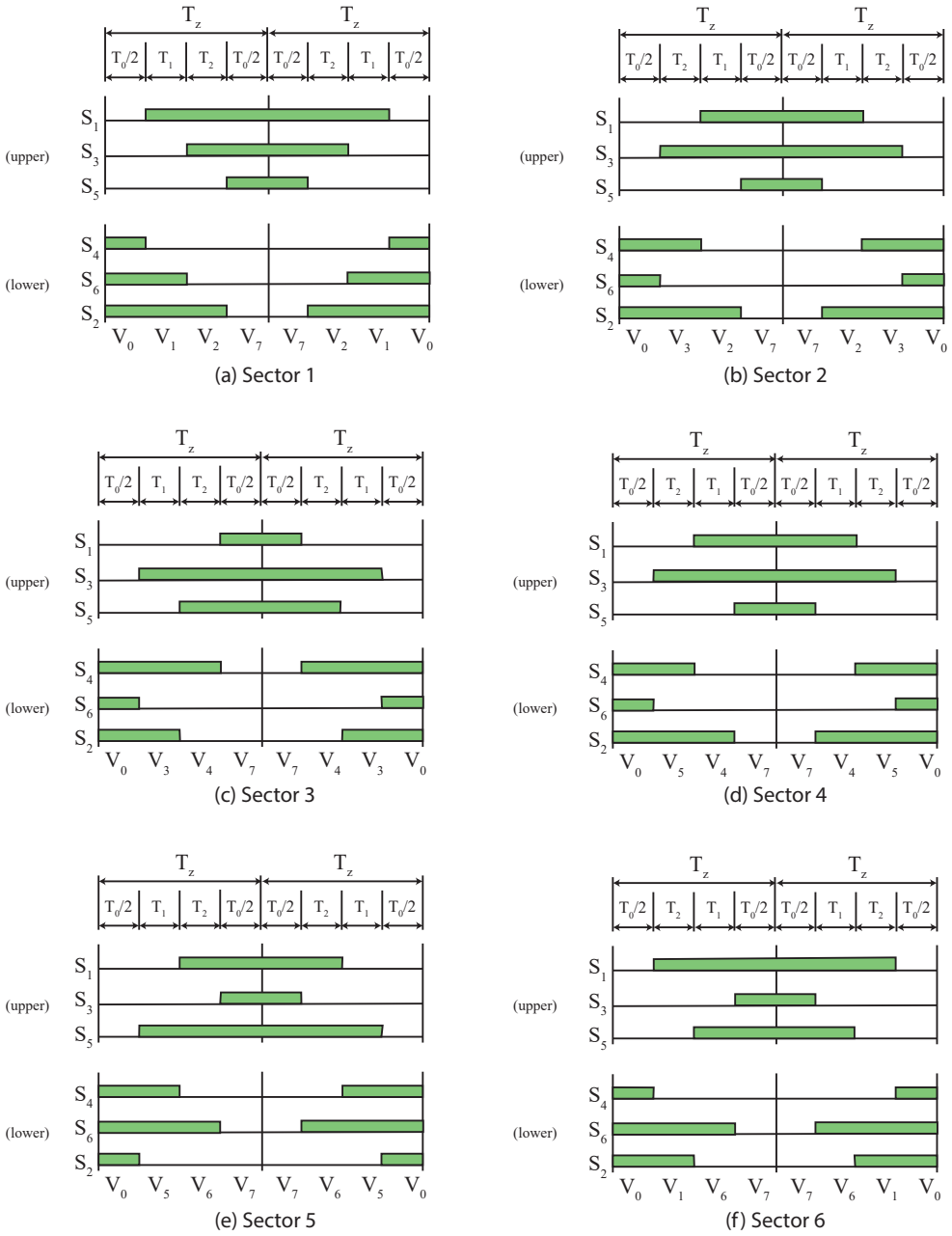

Figure A.4: SVPWM switching patterns at each sector

```
 8 T0=Ts-Ta-Tb
 9 ELSEIF (sector==3) THEN
10 Ta=(SQRT3*mag*Ts)/Vdc*SIN(P-angle)
11 Tb=(SQRT3*mag*Ts)/Vdc*SIN(angle-2*q)
12 T0=Ts-Ta-Tb
13 ELSEIF (sector==4) THEN
14 Ta=(SQRT3*mag*Ts)/Vdc*SIN(4*q-angle)
15 Tb=(SQRT3*mag*Ts)/Vdc*SIN(angle-P)
16 T0=Ts-Ta-Tb
17 ELSEIF (sector==5) THEN
18 Ta=(SQRT3*mag*Ts)/Vdc*SIN(5*q-angle)
19 Tb=(SQRT3*mag*Ts)/Vdc*SIN(angle-4*q)
```

```
T0=Ts-Ta-Tb
ELSEIF (sector==6) THEN
Ta=(SQRT3*mag*Ts)/Vdc*SIN(2*p-angle)
Tb=(SQRT3*mag*Ts)/Vdc*SIN(angle-5*q)
T0=Ts-Ta-Tb
ENDIF
```

Figure A.4 provides the visual illustration of the inverter switching patterns for each sector, from which it is evident that there are seven switching states (intervals) for each cycle, which always starts and ends with a zero vector. The switching times for each IGBT switch corresponding to each sector are shown in Table A.2. From the data given in Table A.2, the modulation waveforms were generated and then they were compared with a triangular carrier waveform externally from the user-defined model to generate the switching pulses for the inverter switches. The corresponding part of the FORTRAN script is given below.

```

IF (sector==1) THEN
D1=Ta+Tb+T0/2
D2=Tb+T0/2
D3=T0/2
ELSEIF (sector==2) THEN
D1=Ta+T0/2
D2=Ta+Tb+T0/2
D3=T0/2
ELSEIF (sector==3) THEN
D1=T0/2
D2=Ta+Tb+T0/2
D3=Tb+T0/2
ELSEIF (sector==4) THEN
D1=T0/2
D2=Ta+T0/2
D3=Ta+Tb+T0/2
ELSEIF (sector==5) THEN
D1=Tb+T0/2
D2=T0/2
D3=Ta+Tb+T0/2
ELSEIF (sector==6) THEN
D1=Ta+Tb+T0/2
D2=T0/2
D3=Ta+T0/2
ENDIF
```

Table A.2: Switching times of each inverter switch at each sector

sector	Upper switches (S_1, S_3, S_5)	Lower switches (S_4, S_6, S_2)
1	$S_1 = T_1 + T_2 + T_0/2$ $S_3 = T_2 + T_0/2$ $S_5 = T_0/2$	$S_4 = T_0/2$ $S_6 = T_1 + T_0/2$ $S_2 = T_1 + T_2 + T_0/2$
2	$S_1 = T_1 + T_0/2$ $S_3 = T_1 + T_2 + T_0/2$ $S_5 = T_0/2$	$S_4 = T_2 + T_0/2$ $S_6 = T_0/2$ $S_2 = T_1 + T_2 + T_0/2$
3	$S_1 = T_0/2$ $S_3 = T_1 + T_2 + T_0/2$ $S_5 = T_2 + T_0/2$	$S_4 = T_1 + T_2 + T_0/2$ $S_6 = T_0/2$ $S_2 = T_1 + T_0/2$
4	$S_1 = T_0/2$ $S_3 = T_1 + T_0/2$ $S_5 = T_1 + T_2 + T_0/2$	$S_4 = T_1 + T_2 + T_0/2$ $S_6 = T_2 + T_0/2$ $S_2 = T_0/2$
5	$S_1 = T_2 + T_0/2$ $S_3 = T_0/2$ $S_5 = T_1 + T_2 + T_0/2$	$S_4 = T_1 + T_0/2$ $S_6 = T_1 + T_2 + T_0/2$ $S_2 = T_0/2$
6	$S_1 = T_1 + T_2 + T_0/2$ $S_3 = T_0/2$ $S_5 = T_1 + T_0/2$	$S_4 = T_0/2$ $S_6 = T_1 + T_2 + T_0/2$ $S_2 = T_2 + T_0/2$

Method 2

The steps of method 2 are the same as in method 1, up to the activation time calculation for corresponding active and zero vectors depending on the sector location of the reference vector. If the sector where the reference signal is located and the activation times for each active and zero vectors are known for each instance, the inverter switching status could be easily determined by comparing the actual time with the activated times of each vector. However, after each cycle, the time needs to be reset as the reference vector should move from sector 1 to sector 6 and back to sector 1. Hence, a sawtooth waveform was generated as the timer, which is very much identical to the PLL output. The vector transition times (intervals) can be calculated using Figure A.4, similar to method 1 and then for each interval, the inverter switching status was determined [86].

The main difference between method 1 and method 2 is the output signals of the developed SVPWM user-defined components. In method 1, three-phase modulation signals are generated as the component output, so that they can be compared with a carrier waveform to generate the switching signals of the inverter switches external to the user-defined component. Whereas in method 2, the user-defined component generates switching signals which can be directly applied to the inverter switches.

A.2 The Complete FORTRAN Codes for SVPWM Method

A.2.1 Method 1

Initializing the parameters used
P=3.141592654
q=1.047197551
SQRT3=1.732050808

Calculating the magnitude of the reference vector
mag=SQRT(Alpha**2+Beta**2)

Determining the angle of the reference vector
IF ((Alpha>0).AND.(Beta≥0)) THEN
angle=ATAN(Beta/Alpha)
ELSEIF ((Alpha>0).AND.(Beta<0)) THEN
angle=ATAN(Beta/Alpha)+(2*p)
ELSEIF ((Alpha==0).AND.(Beta>0)) THEN
angle=P/2
ELSEIF ((Alpha==0).AND.(Beta<0)) THEN
angle=(3*P/2)
ELSEIF (Alpha<0) THEN
angle=ATAN(Beta/Alpha)+P
ENDIF

Determining the sector of the reference signal
IF ((angle≥0).AND.(angle≤P/3)) THEN
sector=1
ELSEIF ((angle>P/3).AND.(angle≤2*P/3)) THEN
sector=2
ELSEIF ((angle>2*P/3).AND.(angle≤P)) THEN
sector=3
ELSEIF ((angle>P).AND.(angle≤4*P/3)) THEN
sector=4
ELSEIF ((angle>4*P/3).AND.(angle≤5*P/3)) THEN
sector=5
ELSEIF ((angle>5*P/3).AND.(angle≤2*P)) THEN
sector=6
ENDIF

Calculating activation times of active and zero vectors

```
IF (sector==1) THEN
Ta=(SQRT3*mag*Ts*SIN(q-angle))/V
Tb=(SQRT3*mag*Ts*SIN(angle))/V
T0=Ts-Ta-Tb
ELSEIF (sector==2) THEN
Ta=(SQRT3*mag*Ts*SIN(2*q-angle))/V
Tb=(SQRT3*mag*Ts*SIN(angle-q))/V
T0=Ts-Ta-Tb
ELSEIF (sector==3) THEN
Ta=(SQRT3*mag*Ts)/V*SIN(P-angle)
Tb=(SQRT3*mag*Ts)/V*SIN(angle-2*q)
T0=Ts-Ta-Tb
ELSEIF (sector==4) THEN Ta=(SQRT3*mag*Ts)/V*SIN(4*q-angle)
Tb=(SQRT3*mag*Ts)/V*SIN(angle-P)
T0=Ts-Ta-Tb
ELSEIF (sector==5) THEN
Ta=(SQRT3*mag*Ts)/V*SIN(5*q-angle)
Tb=(SQRT3*mag*Ts)/V*SIN(angle-4*q)
T0=Ts-Ta-Tb
ELSEIF (sector==6) THEN
Ta=(SQRT3*mag*Ts)/V*SIN(2*p-angle)
Tb=(SQRT3*mag*Ts)/V*SIN(angle-5*q)
T0=Ts-Ta-Tb
ENDIF
```

switching sequence and duty cycle calculation

```
IF (sector==1) THEN
D1=Ta+Tb+T0/2
D2=Tb+T0/2
D3=T0/2
ELSEIF (sector==2) THEN
D1=Ta+T0/2
D2=Ta+Tb+T0/2
D3=T0/2
ELSEIF (sector==3) THEN
D1=T0/2
D2=Ta+Tb+T0/2
D3=Tb+T0/2
```

ELSEIF (sector==4) THEN
D1=T0/2
D2=Ta+T0/2
D3=Ta+Tb+T0/2
ELSEIF (sector==5) THEN
D1=Tb+T0/2
D2=T0/2
D3=Ta+Tb+T0/2
ELSEIF (sector==6) THEN
D1=Ta+Tb+T0/2
D2=T0/2
D3=Ta+T0/2
ENDIF

A.2.2 Method 2

Initializing the parameters used
P=3.141592654
q=1.047197551
SQRT3=1.732050808

Calculating the magnitude of the reference vector
mag=SQRT(Alpha**2+Beta**2)

Determining the angle of the reference vector
IF ((Alpha >0).AND.(Beta≥0)) THEN
angle=ATAN(Beta/Alpha)
ELSEIF ((Alpha>0).AND.(Beta<0)) THEN
angle=ATAN(Beta/Alpha)+(2*p)
ELSEIF ((Alpha==0).AND.(Beta>0)) THEN
angle=P/2
ELSEIF ((Alpha==0).AND.(Beta<0)) THEN
angle=(3*P/2)
ELSEIF (Alpha<0) THEN
angle=ATAN(Beta/Alpha)+P
ENDIF

Determining the sector of the reference signal

```
IF ((angle ≥ 0).AND.(angle ≤ P/3)) THEN
sector=1
ELSEIF ((angle >P/3).AND.(angle ≤ 2*P/3)) THEN
sector=2
ELSEIF ((angle >2*P/3).AND.(angle ≤ P)) THEN
sector=3
ELSEIF ((angle >P).AND.(angle ≤ 4*P/3)) THEN
sector=4
ELSEIF ((angle >4*P/3).AND.(angle ≤ 5*P/3)) THEN
sector=5
ELSEIF ((angle >5*P/3).AND.(angle ≤ 2*P)) THEN
sector=6
ENDIF
```

Calculating activation times of active and zero vectors

```
IF (sector==1) THEN
Ta=(SQRT3*mag*Ts*SIN(q-angle))/V
Tb=(SQRT3*mag*Ts*SIN(angle))/V
T0=Ts-Ta-Tb
ELSEIF (sector==2) THEN
Ta=(SQRT3*mag*Ts*SIN(2*q-angle))/V
Tb=(SQRT3*mag*Ts*SIN(angle-q))/V
T0=Ts-Ta-Tb
ELSEIF (sector==3) THEN
Ta=(SQRT3*mag*Ts)/V*SIN(P-angle)
Tb=(SQRT3*mag*Ts)/V*SIN(angle-2*q)
T0=Ts-Ta-Tb
ELSEIF (sector==4) THEN
Ta=(SQRT3*mag*Ts)/V*SIN(4*q-angle)
Tb=(SQRT3*mag*Ts)/V*SIN(angle-P)
T0=Ts-Ta-Tb
ELSEIF (sector==5) THEN
Ta=(SQRT3*mag*Ts)/V*SIN(5*q-angle)
Tb=(SQRT3*mag*Ts)/V*SIN(angle-4*q)
T0=Ts-Ta-Tb
ELSEIF (sector==6) THEN
Ta=(SQRT3*mag*Ts)/V*SIN(2*p-angle)
Tb=(SQRT3*mag*Ts)/V*SIN(angle-5*q)
T0=Ts-Ta-Tb
```

ENDIF

Timer generation (sawtooth waveform which can determine the interval)
Comp_time=TIME-(INT(TIME/Ts)*Ts)

Vector transition time calculation
t1=T0/4
t2=t1+(T1/2)
t3=t2+(T2/2)
t4=t3+(T0/2)
t5=t4+(T2/2)
t6=t5+(T1/2)
t7=t6+(T0/4)

Determination of switching status for each switch
IF ((Comp_time <t1).AND.((t6 ≤ Comp_time).OR.(Comp_time <t7))) THEN
interval=1
ELSEIF (((t1 ≤ Comp_time).AND.(Comp_time <t2)).OR.((t5 ≤ Comp_time).AND.(Comp_time <t6))) THEN
interval=2
ELSEIF (((t2 ≤ Comp_time).AND.(Comp_time <t3)).OR.((t4 ≤ Comp_time).AND.(Comp_time <t5))) THEN
interval=3
ELSEIF ((t3 ≤ Comp_time).AND.(Comp_time <t4)) THEN
interval=4
ENDIF

Pulse generation
IF (interval==1) THEN
out1=0
out2=0
out3=0
out4=1
out5=1
out6=1
ELSEIF (((interval==2).AND.(sector==1)).OR.((interval==2).AND.(sector==6))) THEN
out1=1
out2=0
out3=0

```
out4=0
out5=1
out6=1
ELSEIF (((interval==2).AND.(sector==2)).OR.((interval==2).AND.(sector==3))) THEN
out1=0
out2=1
out3=0
out4=1
out5=0
out6=1
ELSEIF (((interval==2).AND.(sector==4)).OR.((interval==2).AND.(sector==5))) THEN
out1=0
out2=0
out3=1
out4=1
out5=1
out6=0
ELSEIF (((interval==3).AND.(sector==1)).OR.((interval==2).AND.(sector==2))) THEN
out1=1
out2=1
out3=0
out4=0
out5=0
out6=1
ELSEIF (((interval==3).AND.(sector==3)).OR.((interval==2).AND.(sector==4))) THEN
out1=0
out2=1
out3=1
out4=1
out5=0
out6=0
ELSEIF (((interval==3).AND.(sector==5)).OR.((interval==2).AND.(sector==6))) THEN
out1=1
out2=0
out3=1
out4=0
out5=1
out6=0
ELSEIF (interval==4) THEN
```

```
out1=1
out2=1
out3=1
out4=0
out5=0
out6=0
ENDIF
```

Appendix B

Numerical Calculations

B.1 Analysis of the Results with Numerical Calculations

Based on Figure 5.6 (a), it can be determined that the impedances at the inverter output can be represented by the inductances of 9.47×10^{-6} H and 1.025×10^{-5} H for inverter 1 and inverter 5 respectively. For 5^{th} and 7^{th} harmonics, the Thevenin equivalent impedances are inductive (4.456×10^{-6} H and 5.457×10^{-6} H respectively), and as the rest of the system is also displaying an inductive behaviour, a series resonance should not be present in the impedance scan analysis results conducted with the Thevenin impedances of 5^{th} and 7^{th} harmonic orders. For instance, Figure 5.6 (b) shows that the impedances almost linearly change with the frequency in relation to both Inverter 1 and Inverter 5, replicating inductive impedances of 1.393×10^{-5} H and 1.492×10^{-5} H for those cases. These values are almost identical to the addition of the Thevenin equivalent impedance inductances and the system impedance inductances determined at the inverter output for each harmonic order. The details are summarised in Table B.1.

Table B.1: Summary of the details for the 5^{th} harmonic order

Case	Inductance of the Thevenin impedance (H)	System inductance determined at the inverter terminal (H)	Addition of the Thevenin inductance and system inductance (H)	Determined inductance from Figure 5.6 (b) (H)
Inverter 1	4.456×10^{-6}	9.470×10^{-6}	1.393×10^{-5}	1.393×10^{-5}
Inverter 5	4.456×10^{-6}	1.025×10^{-5}	1.570×10^{-5}	1.492×10^{-5}

The Thevenin equivalent impedance of the 11^{th} harmonic is $(0.0114 - 0.0459\text{i})\,\Omega$, which corresponds to a 0.0114 Ω resistor and a 6304.4 μF capacitor connected in series. The capacitive nature of the Thevenin equivalent impedance and the inductive behaviour of the external network may cause series resonance. From the determined inductive and capacitive component parameters, the resonance frequencies can be calculated as 651.4 Hz and 626.1 Hz associated with inverter 1 and inverter 5 respectively (Figure 5.6), which shows that the series resonance frequency moves towards the 11^{th} harmonic with increas-

ing cable length associated with a reduction in impedance thus supporting the increase in the 11^{th} harmonic current as the cable length increases. The details are summarised in Table B.2.

Table B.2: Summary of the details for the 11^{th} harmonic order

Case	Capacitance of the Thevenin impedance (μF)	System inductance determined at the inverter terminal (H)	Calculated resonance frequency (Hz)
Inverter 1	6304.4	9.470×10^{-6}	651.4
Inverter 5	6304.4	1.025×10^{-5}	626.1

The above method can be extended considering the Thevenin equivalent impedance (0.002-j0.027) Ω of the 13^{th} harmonic. The numerical calculations show that the resonance frequencies for inverter 1 and inverter 5 connected to the grid are 543.1 Hz and 522.0 Hz respectively, which shows that the series resonance frequency decreases and moves away from the 13^{th} harmonic when increasing the cable length. The details are summarised in Table B.3.

Table B.3: Summary of the details for the 13^{th} harmonic order

Case	Capacitance of the Thevenin impedance (μF)	System impedance determined at the inverter terminal (H)	Determined resonance frequency (Hz)
Inverter 1	9068.6	9.470×10^{-6}	543.1
Inverter 5	9068.6	1.025×10^{-5}	522.0